QUANTIFYING THE EFFECT OF ENVIRONMENTS ON CROP EMERGENCE, DEVELOPMENT AND YIELD USING SENSING AND DEEP LEARNING TECHNIQUES

A Dissertation

presented to

the Faculty of the Graduate School

at the University of Missouri-Columbia

In Partial Fulfillment

of the Requirements for the Degree

Doctor of Philosophy

---

by AIJING FENG

Dr. Jianfeng Zhou, Dissertation Supervisor

MAY 2021

The undersigned, appointed by the dean of the Graduate School, have examined the dissertation entitled

QUANTIFYING THE EFFECT OF ENVIRONMENTS ON CROP EMERGENCE, DEVELOPMENT AND YIELD USING SENSING AND DEEP LEARNING TECHNIQUES

presented by Aijing Feng,

a candidate for the degree of doctor of philosophy,

and hereby certify that, in their opinion, it is worthy of acceptance.

_____

Dr. Jianfeng Zhou

_____

Dr. Gang Yao

_____

Dr. Kenneth A. Sudduth

_____

Dr. Toni Kazic

_____

Dr. Earl D. Vories

ACKNOWLEDGEMENTS

I would like to express my sincere appreciation to my advisor and committee chair Dr. Jianfeng Zhou. Dr. Zhou constantly offers me great support and excellent suggestions during the period of my Ph.D. study. Without his mentoring, I could not have completed this dissertation. I not only regard him as my academic advisor but also as a respected elder. He taught me how to think critically, how to do things meticulously, and how to deal with the trivial things in life wisely.

I would like to thank my committee members Dr. Kenneth A. Sudduth and Dr. Earl D. Vories for the help with my experiments as well as all the wonderful suggestions and the review of my publications. They help me improve my writing skills a lot and I learn how to think deeper on a research topic. I would also like to thank my committee members Dr. Gang Yao and Dr. Toni Kazic for all their guidance and suggestions through this long-term process.

I appreciate the great support from my colleagues Jing Zhou and Chin Nee Vong from the Precision and Automated Agriculture Lab at the University of Missouri. They created an excellent environment for research in our lab. I enjoy working with them. They always try their best to help me with the data collection and gave me useful suggestions in my research. We are best friends in life and no matter in life or study, they have helped me a lot.

In the end, I would like to thank the China Scholarships Council fellowship support.

TABLE OF CONTENTS

LIST OF FIGURES

LIST OF TABLES

LIST OF ABBREVIATIONS

AGL	Above Ground Level
ANOVA	Analysis of Variance
API	Application Programming Interface
CDT	Central Daylight Time
CNN	Convolutional Neural Network
CWSI	Crop Water Stress Index
DAP	Day After Planting
DL	Deep Learning
DSM	Digital Surface Model
ET	Evapotranspiration
ExG	Excess Green Index
GDD	Growing Degree Days
GNDVI	Green NDVI
GNSS	Global Navigation Satellite System
GRP	Ground Reference Point
GRU	Gated Recurrent Units
GSD	Ground Sampling Distance
KNN	K-Nearest Neighbors
LSTM	Long Short-Term Memory network
MAE	Mean Absolute Error
MAPE	Mean Absolute Percentage Error

NDVI	Normalized Difference Vegetation Index
NIR	Near-Infrared
PVC	Polyvinyl Chloride
R^2	Correlation of Determination
ReLU	Rectified Linear Unit
RGB	Red-Green-Blue
RNN	Recurrent Neural Network
ROI	Region of Interest
RTK	Real Time Kinematics
SfM	Structure from Motion
SHT	Standard Hough transform
SSD	Solid-State Drive
SURF	Speeded-Up Robust Features
UAV	Unmanned Aerial Vehicle
VI	Vegetation Index
VRI	Variable Rate Irrigation
WAAS	Wide Area Augmentation System

QUANTIFYING THE EFFECT OF ENVIRONMENTS ON CROP EMERGENCE, DEVELOPMENT AND YIELD USING SENSING AND DEEP LEARNING TECHNIQUES

Aijing Feng

Dr. Jianfeng Zhou, Dissertation Supervisor

ABSTRACT

The world population is estimated to increase by 2 billion in the next 30 years, and global crop production needs to double by 2050 to meet the projected demands from rising population, diet shifts, and increasing biofuels consumption. Improving the production of the major crops has become an increasing concern for the global research community. However, crop development and yield are complex and determined by many factors, such as crop genotypes (varieties), growing environments (e.g., weather, soil, microclimate and location), and agronomic management strategies (e.g., seed treatment and placement, planting, fertilizer and pest management). To develop next-generation and high-efficiency agriculture production systems, we will have to solve the complex equation consisting of the interactions of genotype, environment and management (G×E×M) using emerging technologies. Precision agriculture is a promising agriculture practice to increase profitability and reduce environmental impact using site-specific and accurate measurement of crop, soil and environment. The success of precision agriculture technology heavily relies on access to accurate and high-resolution spatiotemporal data and reliable prediction models of crop development and yield.

Soil texture and weather conditions are important factors related to crop growth and yield. The percentages of sand, clay and silt in the soil affect the movement of air and water, as well as the water holding capacity. Weather conditions, including temperature,

wind, humidity and solar irradiance, are determining factors for crop evapotranspiration and water requirements. Compared to crop yield, which is easy to measure and quantify, crop development effects due to the soil texture and weather conditions within a season can be challenging to measure and quantify. Evaluation of crop development by visual observation at field scale is time-consuming and subjective. In recent years, sensor-based methods have provided a promising way to measure and quantify crop development. Unmanned aerial vehicles (UAVs) equipped with visual sensors, multispectral sensors and/or hyperspectral sensors have been used as a high-throughput data collection tool by many researchers to monitor crop development efficiently at the desired time and at field-scale.

In this study, UAV-based remote sensing technologies combining with soil texture and weather conditions were used to study the crop emergence, crop development and yield under the effects of varying soil texture and weather conditions in a cotton research field. Soil texture, i.e., sand and clay content, calculated using apparent soil electrical conductivity (EC_a) based on a model from a previous study, was used to estimate soil characteristics, including field capacity, wilting point and total available water. Weather data were obtained from a weather station 400 m from the field. UAV imagery data were collected using a high-resolution RGB camera, a multispectral camera and a thermal camera from the crop emergence to before harvesting on a monthly basis. An automatic method to count emerged crop seedlings based on image technologies and a deep learning model was developed for near real-time cotton emergence evaluation. The soil and elevation effects on the stand count and seedling size were explored. The effects of soil texture and weather conditions on cotton growth variation were examined using

multispectral images and thermal images during the crop development growth stages. The cotton yield variations due to soil texture and weather conditions were estimated using multiple-year UAV imagery data, soil texture, weather conditions and deep learning techniques.

The results showed that field elevation had a high impact on cotton emergence (stand count and seedling size) and clay content had a negative impact on cotton emergence in this study. Monthly growth variations of cotton under different soil textures during crop development growth stages were significant in both 2018 and 2019. Soil clay content in shallow layers (0-40 cm) affected crop development in early growth stages (June and July) while clay content in deep layers (40-70 cm) affected the mid-season growth stages (August and September). Thermal images were more efficient in identifying regions of water stress compared to the water stress coefficient K_s calculated using data of soil texture and weather conditions. Results showed that cotton yield for each one of the three years (2017-2019) could be predicted using the model trained with data of the other two years with prediction errors of MAE = 247 (8.9%) to 384 kg ha^{-1} (13.7%), which showed that quantifying yield variability for a future year based on soil texture, weather conditions and UAV imagery was feasible. Results from this research indicated that the integration of soil and weather information and UAV-based image data is a promising way to understand the effects of soil and weather on crop emergence, crop development and yield.

Chapter 1. INTRODUCTION

1.1 Problem Statement

Crop production is the function of genotype, environment and management (Hatfield and Walthall, 2015). With the development of urbanization, the available cultivated land is reducing in recent decades. Moreover, long-term cultivation leads to a decline in soil quality (e.g. soil erosion, salinization, nutrient reduction), which affects future cultivation (Pennock et al., 2015). Because of the worsening environmental problems, freshwater resources are becoming more and more precious. Faced with the rapid growth of population, increasing crop yield using less freshwater resources, less input under the current situation of soil resources and cultivated land is an important topic.

Timely monitoring of crop development and accurate estimation of yield are important to help improving field management and crop production. The information obtained from different crop growth stages can be used to explore environmental impacts and nutrient deficiencies. For example, Holman et al. (2016) monitored the wheat plant height in five days and found out that the growth rates range from -13 mm /day to 17 mm /day subject to four different nitrogen fertilizer treatments. Farmers could understand the growth status of crops and make management adjustments through monitoring crop growth in critical multi-temporal growth stages.

Weather, soil texture and irrigation treatment affect crop development and yield. Soil texture type is an important soil property related to crop growth (Scherer et al., 2017). The size of solid particles can be used to classify soil texture as clay (less than 0.002 mm), silt (from 0.002 mm to 0.05 mm) and sand (from 0.05 mm to 2 mm). The percentage of

sand, clay and silt content in the soil would affect the movement of air and water, as well as the water holding capacity.

Compared to the crop yield, which is easy to measure and quantify, crop development effects due to the soil texture and weather conditions within a growing season could be challenging to measure and quantify. Evaluation of crop development by visual observation in field-scale is time-consuming and subjective. In recent years, sensor-based methods have provided a promising way to measure and quantify crop development (Bendig et al., 2015; Hunt et al., 2013). Vegetation indices (VIs) such as normalized difference vegetation index (NDVI), chlorophyll vegetation index, triangular greenness index, and green red vegetation index can be used to quantify the crop growth status objectively. In remote sensing applications, VIs have been widely used for qualitative and quantitative evaluation of vegetation cover and its growth. In the visible range of light (spectral), the reflectance of green light (as shown in Figure 1.1) of plants is higher than that of blue and red (R). Red-edge and near-infrared (NIR) were 2 kinds of invisible light (as shown in Figure 1.1), which are in 700-800nm and 800-1000nm. Plants have higher reflectance near the infrared, which is obviously different from the reflection of soil (similar reflectance from 400 nm to 1000 nm). Moreover, different plants or those in different growth conditions reflect different values at red-edge. The slope of the reflection curve of crops in the red-edge range can reflect the growth states of crops. Thus, the red-edge and near-infrared spectral region are of critical importance to describe crop traits comparing to visual wavelengths. The difference between NIR and R reflection of healthy green vegetation is relatively large because R is strongly absorbed by green plants, while NIR is the high reflection and high transmittance, which means that the healthier plants

have larger NDVI values (the equation is listed in Table 5.3). NIR and R of rock or bare soil are close to each other, so their NDVI was close to 0. Negative NDVI values indicated the effects of light and clouds. As for GNDVI (the equation is listed in Table 5.3), the green channel is more linked to the chlorophyll and nitrogen content of plants, so it can use to estimate vegetation biomass and leaf area index (Hunt et al., 2011). A study found that both NDVI and GNDVI were reliable predictors for forage biomass, forage N uptake, grain yield, grain N uptake in winter wheat (Moges et al., 2005). As for NDRE (the equation is listed in Table 5.3), a study used it as a Canopy Chlorophyll Content Index (CCCI) to estimate water and nitrogen stress (Barnes et al., 2000). Unmanned aerial vehicles (UAVs) equipped with visual sensors, multispectral sensors and/or hyperspectral sensors have been used as a high-throughput data collection tool by many researchers to monitor crop development at the desired time efficiently at field-scale (Turner, Lucieer, Malenovský, King, & Robinson, 2014).

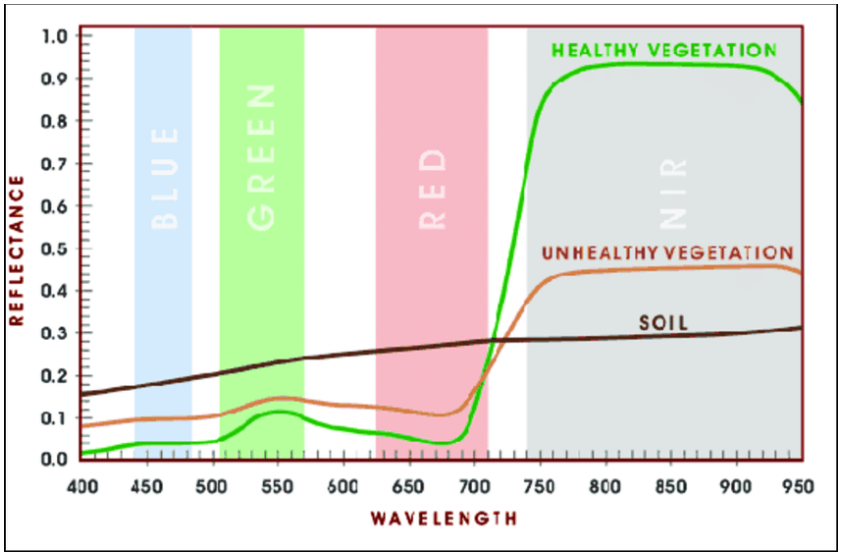

Figure 1.1: Spectral reflection of healthy plants, unhealthy plants and soil (Chang et al., 2013)

1.2 Literature review

Soil and weather affect crop emergence, development and yield

Since soil texture affects soil water holding capacity, it is one of the more important factors that affecting crop development and yield. Forcella et al. (2000) reported that soil texture and soil water content affected seedling emergence date and emergence rate. Soil texture and soil water content also affected root development (Oosterhuis, 1990). Allen et al. (1998) pointed out that during the growing season, weather conditions (i.e. daily temperature, wind speed, relative humidity and solar irradiance) at different crop growth stages affected the crop evapotranspiration (ET) and water requirements. Models calculating the ET (FAO-56) provided in Allen et al. (1998) based on the soil, weather and crop growth are widely used for irrigation design and schedule, which calculate from ET_o, crop coefficient K_c and water stress coefficient K_s. Once the water content in the soil cannot satisfy the crop water requirements, crop development would be influenced and those influences would eventually be reflected in yield. Many studies found that soil texture (or soil EC_a) was related to the yield of cotton (Vories et al., 2020), corn (Kitchen et al., 2003; Kitchen et al., 2005) and soybean (Jiang and Thelen, 2004; Kitchen et al., 2005).

Daily weather data determine the water loss due to soil evaporation (E) and crop transportation (T) (Allen et al., 1998). Weather parameters of radiation and air temperature provide energy for ET, air humidity affects the water stored capability in the air, and wind speed that affects the capability of water removal (Allen et al., 1998). Models such as Penman-Monteith (PM) model, Hargreaves–Samani (HS) model and Priestly–Taylor (PT)

model were widely used for calculating ET based on daily weather parameters (Chia et al., 2020). Weather conditions of temperature, precipitation and solar radiation had been shown to be important effects for yield variability of maize and winter wheat between years (Ceglar et al., 2016). Addy et al. (2020) showed that the functional response of crop yield to nitrogen application rate varied under different weather conditions between years. Addy et al. (2020) showed that the cereal grain yield had different responses to nitrogen application under various weather conditions during 1968-2016. Tremblay et al. (2012) showed that weather conditions could influence the corn response to nitrogen. Battisti et al. (2018) showed that weather condition was an important component for soybean yield estimation. Van Bussel et al. (2016) used weather data for long-term (30 years) wheat yield estimation.

Sensor networks for crop monitoring

To explore the soil and weather effects on crop development and yield, data related to soil texture, weather and crop development states are required. Sensor-based in-field measurement networks were used for data collection and analysis for crop development monitoring due to different environmental conditions.

Soil texture usually is determined by laboratory analysis, which analyzes the sand, clay and silt content. Sensor-based in-field measurements to determine the soil texture have been used by some researchers. For example, Sudduth et al. (2005), Stępień et al. (2015) and James et al. (2003) reported that the apparent electrical conductivity (EC_a) measured by mobile sensors was related to clay, sand and silt content. Compared to the traditional laboratory methods, sensor-based methods had the advantage of providing dense datasets at a lower cost and high efficiency (Sudduth et al., 2005).

Crop growth can be monitored with remotely sensed data acquired at various platforms (Cheng et al., 2016). Some researchers monitored crop in a large-scale area through vegetation indices of satellite images (e.g. NDVI, GNDVI) using vegetation indices (Fermont and Benson, 2011). Satellite images are limited by low resolution, the influence of the cloud, and predetermined data collection times. The resolution of satellite images is generally not high enough for accurate yield estimation. For example, the resolution of free or affordable multispectral satellite images such as Sentinel-2 is around 10 m (Liu, Wang, Skidmore, & Liu, 2018; Singhal, Bansod, Mathew, & Taneja, 2018). Commercial sources such as WorldView-3 provide panchromatic imagery with a 0.31 m resolution and multispectral imagery with a 1.24 m resolution (Rahman, Robson, & Bristow, 2018). However, it is a challenge to acquire images at the desired time of day, such as noon when plants may show more symptoms of stresses. For thermal images, the resolution is about 60 m -100 m from Landsat (Amazirh et al., 2018) and ASTER (Zhang et al., 2017) which is not sufficient for precision decision making in sub-field management zones. Meanwhile, atmospheric factors, such as clouds and humidity, make it challenging to utilize satellite images for the collection of dynamic and high-resolution crop information for field management.

Ground-based platforms were also used to monitor crop growth by some studies. For example, Ni et al. (2018) used a handhold system equipped with a multispectral sensor to monitor wheat canopy spectral reflectance. The advantage of the extremely high resolution of the ground-based platforms makes them good tools to assess crop emergence. For example, Jin et al. (2017) and Liu et al. (2017) used ground vehicle-based imaging systems to assess wheat stand count in field conditions. However, ground vehicle-based

systems have many limitations when they are used in full-scale crop production, such as being slow and affected by ground conditions (e.g., wet soil or narrow-row cropping systems).

Field monitoring with UAV integrated with remote sensors are increasingly used in agriculture recently due to the ultra-high spatial frequencies and efficiency of the UAV sensing systems (Yang et al., 2017). Some examples include the assessment of wheat density (Jin et al., 2017; Sankaran et al., 2015a), cotton uniformity (Feng et al., 2020), and stand count in cotton (Chen et al., 2018; Feng et al., 2020), corn (Varela et al., 2018), potato (Sankaran et al., 2017) and rapeseed (Zhao et al., 2018). Equipped with proper sensors, UAV-based remote sensing systems are able to provide low-cost and high-resolution digital surface models (DSMs) and orthomosaic images for researchers and farmers in a timely manner (Yang et al., 2017). Du and Noguchi (2017) used a UAV equipped with an RGB camera to monitor wheat growth status and estimate yield. UAV can also be used to monitor e.g. canopy cover (Chu et al., 2016), crop height (Chang et al., 2017), germination rate (Chen et al., 2015). Studies have also used UAV-based remote sensing technologies to estimate crop evaporation (Hoffmann et al., 2016b) and crop water status (Romero et al., 2018) and have quantified water stress (Gago et al., 2017; Hoffmann et al., 2016a; Zhang et al., 2019). These studies explored the relationships between VIs and evapotranspiration (latent heat flux) calculated by energy balance models, water status measured by pressure bomb, ground measured stomatal conductance and sap flow under different irrigation treatments.

Crop monitoring using multi-temporal UAV-based image data attracted a lot of attention recently. Multi-temporal image data were mainly used to monitor the growth

changes between different growth stages. The growth changes would be different based on the different treatment of the crops. For example, different nitrogen fertilizer treatments (Yue et al., 2018), different varieties (Pádua et al., 2018), different irrigation treatment (Dayananda et al., 2019), conventional tillage and no-tillage system (Ashapure et al., 2019), different field elevation and different planting date (Yang et al., 2019). By comparing the growth changes, the effect of those different treatments could be explored. The built multi-temporal model could also use to estimate yield (Yang et al., 2019), biomass (Dayananda et al., 2019) and chlorophyll content (Aasen and Bolten, 2018).

1.3 Problems not been solved

The need for rapid and accurate emergence assessment in early stage

Many UAV image studies used similar approaches to process UAV imagery data, i.e., using commercial UAV image processing software, such as Agisoft PhotoScan (Agisoft LLC, St. Petersburg, Russia) and Pix4D (Pix4D S.A., Lausanne, Switzerland), to generate orthomosaic images before further processing. The procedure of generating orthomosaic images includes image feature detection, matching, alignment and blending based on mosaic blending models as described by Brown and Lowe (2003), which may take a very long time (days or weeks) and require extensive computational resources. For example, it took more than two weeks to develop an orthomosaic image using 2000 images of 4864 × 3648 pixels using Agisoft in one of our projects. The software was running in a workstation desktop computer (Model Dell Precision Tower 5810, Dell, Round Rock, TX, USA) configured with an Intel Xeon E5 (1630 v3) 3.70 GHz central processing unit (CPU), 32GB random-access memory (RAM) and an NVIDIA Quadro K1200 4GB graphics processing unit (GPU). Crop seedlings are usually small and require high-resolution

images to capture sufficient information, which results in a large number of images for mosaic processing and makes it challenging to make timely decisions. The challenge in the timely processing of imagery data becomes one of the most critical barriers for adopting UAV imagery in applications of crop emergence assessment (Forcella et al., 2000; Supak, 1990). Although leveraging high-performance computing or cloud computing resources may provide an alternative solution, it requires expensive and complicated infrastructure that may not be feasibly or economically accessible by most users. Therefore, there is a pressing need to develop a cost-effective solution for timely image processing and real-time decision making.

Current studies related to crop emergence using UAV imagery focus on stand count and uniformity (Feng et al., 2020). Crop seedlings were usually segmented by their morphological features from the images to estimate the number of seedlings in a certain row length or area. The image features include canopy area (total number of green pixels) (Gnädinger and Schmidhalter, 2017), leaf polygons (Chen et al., 2018), and major axis length (Jin et al., 2017; Zhao et al., 2018). Developing seedling templates based on the statistical analysis of seedling geometric shape that is then matched with every single plant in images is another way to count seedlings (Koh et al., 2019). However, the shape, size and overlap of individual seedlings may vary in a large range (Zhao et al., 2018) due to the variation in soil conditions (moisture, temperature, nutrients), cropping system, planting depth and seed quality (Egli and Rucker, 2012; Feng et al., 2020). Simple image features or their combinations are not sufficient to identify seedlings accurately, which will result in large errors in the evaluation of stand count. In addition, most of the published studies used seedling clusters (overlapped seedlings) as regions of interest (RoIs) and then

developed classification models to estimate the number of seedlings in each RoI. However, Feng et al. (2020) found that the number of plants in each RoI was unbalanced and most of the RoIs contained one or two seedlings with only a few RoIs containing three or four seedlings. Unbalanced data sets could affect the estimation accuracy (Chawla, 2009); however, this effect can be potentially reduced by using regression models (Ribera et al., 2017).

The need of quantifying the effects of soil, water and weather on plant growth and yield

Even though studies had shown that soil and weather affect crop development and yield, the combined effects of soil and weather on crops are complicated. Crops showed a different level of weather-sensitive in different regions (Mathieu and Aires, 2018) and different growth stages (Addy et al., 2020; Ceglar et al., 2016). Crop development and yield also showed different dependence on soil under different years' weather conditions (Feng et al., 2021). Studies had developed many crop models from regions to the global to quantify crop development and yield based on weather and soil (Van Bussel et al., 2016). The development of those models required more than 10 years of data and generally needed a recalibration when used in other regions (Ceglar et al., 2016). Khaki et al. (2020) and Khaki and Wang (2019) developed yield prediction models based on weather and soil that can work for different states of the USA but needed data of 35 years and 9 years respectively.

Evaluation of high-resolution spatiotemporal crop, soil and weather

Most of the available literature focusing on a single sensor (RGB or multispectral cameras). Some researchers have noticed the prospect of multi-sensors for precision

agriculture. Busemeyer et al. (2013) mentioned that a single sensor showed constraints in the determination accuracy of more complex traits like biomass yield. No thermal multi-temporal images or multi-sensors were used in the above literature. The effect of soil texture and weather on crop development from emergence to harvest has not been sufficiently investigated.

Integration of emerging data analysis techniques: machine learning and deep learning

Advanced data processing technology, deep learning (DL), has been increasingly used to process imagery data collected in agricultural applications this decade (Kamilaris and Prenafeta-Boldú, 2018). Deep learning models have been used to extract hidden information from imagery data collected by satellites, UAVs and ground robotic systems to monitor crop development and predict yield (Humphrey et al., 2012; Nanni et al., 2017). In addition, the multilayer structure of DL models works well for complex nonlinear problems (Nielsen, 2015). However, high accuracy prediction and explainable models are still not exploring enough under various agriculture application (Adão et al., 2017; Kamilaris and Prenafeta-Boldú, 2018).

1.4 Goals of the study

The goal of this study is to quantify the effects of soil and weather conditions on crop emergence, crop development and yield using sensing and data analytic technologies. This study tried to focus on the technologies and methods for extracting features of the crop, soil and weather from different sensing systems and tried to use the integrated data of soil, weather and images to understand the soil and weather effects on crop emergence, crop development and yield.

The specific objectives included:

1) Methods to characterize crop development and yield using UAV-based remote sensing and deep learning technologies;
2) Fusion of different spatiotemporal resolution soil, weather and images data;
3) Quantification of soil and weather effects on crop development and yield.

The study would organize the above contents as four majority Chapters: emergence evaluation study as described in Chapter 3, soil and elevation effects on crop emergence as described in Chapter 4, crop development monitoring study as described in Chapter 5, and yield estimation study as described in Chapter 6.

1.5 Literature cited

Aasen, H., Bolten, A., 2018. Multi-temporal high-resolution imaging spectroscopy with hyperspectral 2D imagers–From theory to application. Remote sensing of environment 205, 374-389.

Adão, T., Hruška, J., Pádua, L., Bessa, J., Peres, E., Morais, R., Sousa, J., 2017. Hyperspectral imaging: a review on Uav-based sensors, data processing and applications for agriculture and forestry. Remote Sensing 9, 1110.

Addy, J.W., Ellis, R.H., Macdonald, A.J., Semenov, M.A., Mead, A., 2020. Investigating the effects of inter-annual weather variation (1968–2016) on the functional response of cereal grain yield to applied nitrogen, using data from the Rothamsted Long-Term Experiments. Agricultural and Forest Meteorology 284, 107898.

Allen, R., Pereira, L., Raes, D., Smith, M., 1998. Crop evapotranspiration-Guidelines for computing crop water requirements-FAO Irrigation and drainage paper 56. Fao, Rome 300, D05109.

Ashapure, A., Jung, J., Yeom, J., Chang, A., Maeda, M., Maeda, A., Landivar, J., 2019. A novel framework to detect conventional tillage and no-tillage cropping system effect on cotton growth and development using multi-temporal UAS data. ISPRS Journal of Photogrammetry and Remote Sensing 152, 49-64.

Barnes, E., Clarke, T., Richards, S., Colaizzi, P., Haberland, J., Kostrzewski, M., Waller, P., Choi, C., Riley, E., Thompson, T., 2000. Coincident detection of crop water stress, nitrogen status and canopy density using ground based multispectral data, Proceedings of the Fifth International Conference on Precision Agriculture, Bloomington, MN, USA.

Battisti, R., Bender, F.D., Sentelhas, P.C., 2018. Assessment of different gridded weather data for soybean yield simulations in Brazil. Theoretical and Applied Climatology.

Bendig, J., Yu, K., Aasen, H., Bolten, A., Bennertz, S., Broscheit, J., Gnyp, M.L., Bareth, G., 2015. Combining UAV-based plant height from crop surface models, visible, and near infrared vegetation indices for biomass monitoring in barley. International Journal of Applied Earth Observation and Geoinformation 39, 79-87.

Busemeyer, L., Mentrup, D., Möller, K., Wunder, E., Alheit, K., Hahn, V., Maurer, H.P., Reif, J.C., Würschum, T., Müller, J., 2013. BreedVision—A multi-sensor platform for non-destructive field-based phenotyping in plant breeding. Sensors 13, 2830-2847.

Ceglar, A., Toreti, A., Lecerf, R., Van der Velde, M., Dentener, F., 2016. Impact of meteorological drivers on regional inter-annual crop yield variability in France. Agricultural and forest meteorology 216, 58-67.

Chang, A., Jung, J., Maeda, M.M., Landivar, J., 2017. Crop height monitoring with digital imagery from Unmanned Aerial System (UAS). Computers and Electronics in Agriculture 141, 232-237.

Chang, J., Clay, D.E., Clay, S.A., Reese, C.L., 2013. Using Field Scouting or Remote Sensing Technique to Assess Soybean Yield Limiting Factors.

Chen, Y., Mei, X., Liu, J., 2015. Cotton growth monitoring and yield estimation based on assimilation of remote sensing data and crop growth model, Geoinformatics, 2015 23rd International Conference on. IEEE, pp. 1-4.

Cheng, T., Yang, Z., Inoue, Y., Zhu, Y., Cao, W., 2016. Preface: Recent advances in remote sensing for crop growth monitoring. Multidisciplinary Digital Publishing Institute.

Chia, M.Y., Huang, Y.F., Koo, C.H., Fung, K.F., 2020. Recent Advances in Evapotranspiration Estimation Using Artificial Intelligence Approaches with a Focus on Hybridization Techniques—A Review. Agronomy 10, 101.

Chu, T., Chen, R., Landivar, J.A., Maeda, M.M., Yang, C., Starek, M.J., 2016. Cotton growth modeling and assessment using unmanned aircraft system visual-band imagery. Journal of Applied Remote Sensing 10, 036018.

Dayananda, S., Astor, T., Wijesingha, J., Chickadibburahalli Thimappa, S., Dimba Chowdappa, H., Nidamanuri, R.R., Nautiyal, S., Wachendorf, M., 2019. Multi-

Temporal Monsoon Crop Biomass Estimation Using Hyperspectral Imaging. Remote Sensing 11, 1771.

Du, M., Noguchi, N., 2017. Monitoring of wheat growth status and mapping of wheat yield's within-field spatial variations using color images acquired from UAV-camera system. Remote Sensing 9, 289.

Fermont, A., Benson, T., 2011. Estimating yield of food crops grown by smallholder farmers. International Food Policy Research Institute, Washington DC, 1-68.

Forcella, F., Arnold, R.L.B., Sanchez, R., Ghersa, C.M., 2000. Modeling seedling emergence. Field Crops Research 67, 123-139.

Gago, J., Fernie, A.R., Nikoloski, Z., Tohge, T., Martorell, S., Escalona, J.M., Ribas-Carbó, M., Flexas, J., Medrano, H., 2017. Integrative field scale phenotyping for investigating metabolic components of water stress within a vineyard. Plant Methods 13, 90.

Hatfield, J.L., Walthall, C.L., 2015. Meeting global food needs: realizing the potential via genetics× environment× management interactions. Agronomy Journal 107, 1215-1226.

Hoffmann, H., Jensen, R., Thomsen, A., Nieto, H., Rasmussen, J., Friborg, T., 2016a. Crop water stress maps for an entire growing season from visible and thermal UAV imagery. Biogeosciences 13, 6545.

Hoffmann, H., Nieto, H., Jensen, R., Guzinski, R., Zarco-Tejada, P., Friborg, T., 2016b. Estimating evaporation with thermal UAV data and two-source energy balance models. Hydrology and Earth System Sciences 20, 697-713.

Holman, F.H., Riche, A.B., Michalski, A., Castle, M., Wooster, M.J., Hawkesford, M.J., 2016. High throughput field phenotyping of wheat plant height and growth rate in field plot trials using UAV based remote sensing. Remote Sensing 8, 1031.

Hunt, E.R., Doraiswamy, P.C., McMurtrey, J.E., Daughtry, C.S.T., Perry, E.M., Akhmedov, B., 2013. A visible band index for remote sensing leaf chlorophyll content at the canopy scale. International Journal of Applied Earth Observation and Geoinformation 21, 103-112.

Hunt, E.R., Hively, W.D., McCarty, G.W., Daughtry, C.S.T., Forrestal, P.J., Kratochvil, R.J., Carr, J.L., Allen, N.F., Fox-Rabinovitz, J.R., Miller, C.D., 2011. NIR-green-blue high-resolution digital images for assessment of winter cover crop biomass. GIScience & Remote Sensing 48, 86-98.

James, I., Waine, T., Bradley, R., Taylor, J., Godwin, R., 2003. Determination of soil type boundaries using electromagnetic induction scanning techniques. Biosystems Engineering 86, 421-430.

Jiang, P., Thelen, K., 2004. Effect of soil and topographic properties on crop yield in a north-central corn–soybean cropping system. Agronomy Journal 96, 252-258.

Kamilaris, A., Prenafeta-Boldú, F.X., 2018. Deep learning in agriculture: A survey. Computers and electronics in agriculture 147, 70-90.

Khaki, S., Wang, L., 2019. Crop Yield Prediction Using Deep Neural Networks. Frontiers in Plant Science 10.

Khaki, S., Wang, L., Archontoulis, S.V., 2020. A cnn-rnn framework for crop yield prediction. Frontiers in Plant Science 10, 1750.

Kitchen, N., Drummond, S., Lund, E., Sudduth, K., Buchleiter, G., 2003. Soil electrical conductivity and topography related to yield for three contrasting soil–crop systems. Agronomy Journal 95, 483-495.

Kitchen, N., Sudduth, K., Myers, D., Drummond, S., Hong, S., 2005. Delineating productivity zones on claypan soil fields using apparent soil electrical conductivity. Computers and Electronics in Agriculture 46, 285-308.

Mathieu, J.A., Aires, F., 2018. Assessment of the agro-climatic indices to improve crop yield forecasting. Agricultural And Forest Meteorology 253, 15-30.

Moges, S., Raun, W., Mullen, R., Freeman, K., Johnson, G., Solie, J., 2005. Evaluation of green, red, and near infrared bands for predicting winter wheat biomass, nitrogen uptake, and final grain yield. Journal of Plant Nutrition 27, 1431-1441.

Ni, J., Zhang, J., Wu, R., Pang, F., Zhu, Y., 2018. Development of an Apparatus for Crop-Growth Monitoring and Diagnosis. Sensors 18, 3129.

Oosterhuis, D.M., 1990. Growth and development of a cotton plant. Nitrogen Nutrition of Cotton: Practical Issues, 1-24.

Pádua, L., Marques, P., Hruška, J., Adão, T., Peres, E., Morais, R., Sousa, J., 2018. Multi-Temporal Vineyard Monitoring through UAV-Based RGB Imagery. Remote Sensing 10, 1907.

Pennock, D., McKenzie, N., Montanarella, L., 2015. Status of the World's Soil Resources. Technical Summary FAO, Rome, Italy.

Romero, M., Luo, Y., Su, B., Fuentes, S., 2018. Vineyard water status estimation using multispectral imagery from an UAV platform and machine learning algorithms

for irrigation scheduling management. Computers and Electronics in Agriculture 147, 109-117.

Scherer, T.F., Franzen, D., Cihacek, L., 2017. Soil, water and plant characteristics important to irrigation. North Dakota State University, Fargo, North Dakota.

Stępień, M., Samborski, S., Gozdowski, D., Dobers, E.S., Chormański, J., Szatyłowicz, J., 2015. Assessment of soil texture class on agricultural fields using ECa, Amber NDVI, and topographic properties. Journal of Plant Nutrition and Soil Science 178, 523-536.

Sudduth, K.A., Kitchen, N.R., Wiebold, W., Batchelor, W., Bollero, G., Bullock, D., Clay, D., Palm, H., Pierce, F., Schuler, R., 2005. Relating apparent electrical conductivity to soil properties across the north-central USA. Computers and Electronics in Agriculture 46, 263-283.

Tremblay, N., Bouroubi, Y.M., Bélec, C., Mullen, R.W., Kitchen, N.R., Thomason, W.E., Ebelhar, S., Mengel, D.B., Raun, W.R., Francis, D.D., 2012. Corn response to nitrogen is influenced by soil texture and weather. Agronomy Journal 104, 1658-1671.

Van Bussel, L.G., Ewert, F., Zhao, G., Hoffmann, H., Enders, A., Wallach, D., Asseng, S., Baigorria, G.A., Basso, B., Biernath, C., 2016. Spatial sampling of weather data for regional crop yield simulations. Agricultural and Forest Meteorology 220, 101-115.

Vories, E., O'Shaughnessy, S., Sudduth, K.A., Evett, S., Andrade, M., Drummond, S., 2020. Comparison of precision and conventional irrigation management of cotton and impact of soil texture. Precision Agriculture, 1-18.

Yang, G., Liu, J., Zhao, C., Li, Z., Huang, Y., Yu, H., Xu, B., Yang, X., Zhu, D., Zhang, X., 2017. Unmanned aerial vehicle remote sensing for field-based crop phenotyping: current status and perspectives. Frontiers in Plant Science 8, 1111.

Yang, Q., Shi, L., Han, J., Zha, Y., Zhu, P., 2019. Deep convolutional neural networks for rice grain yield estimation at the ripening stage using UAV-based remotely sensed images. Field Crops Research 235, 142-153.

Yue, J., Feng, H., Jin, X., Yuan, H., Li, Z., Zhou, C., Yang, G., Tian, Q., 2018. A comparison of crop parameters estimation using images from UAV-mounted snapshot hyperspectral sensor and high-definition digital camera. Remote Sensing 10, 1138.

Zhang, L., Zhang, H., Niu, Y., Han, W., 2019. Mapping maize water stress based on UAV multispectral remote sensing. Remote Sensing 11, 605.

Chapter 2. GROUND DATA COLLECTION AND EXPERIMENT DESIGN

2.1 Experimental field

This study was conducted in a cotton research field at the Fisher Delta Research Center of the University of Missouri, located in the upper portion of the Mississippi River Delta region near Portageville, MO, USA as shown in Figure 2.1. The experimental site includes two sub-fields, i.e., west side and east side (East and West field hereafter). The two fields have similar dimensions of approx. 320 m × 160 m with the long dimension in the south-north direction.

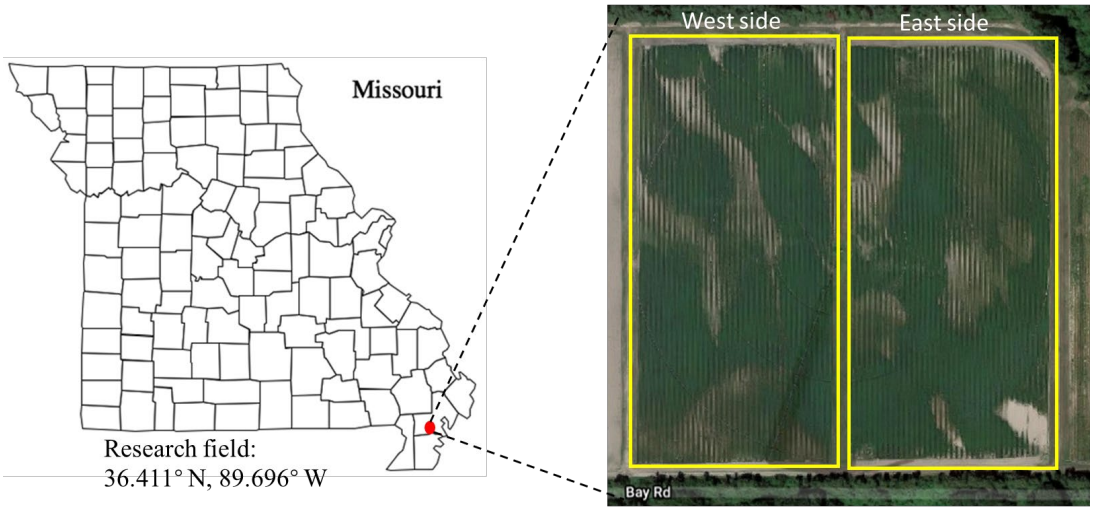

Figure 2.1: The research site includes two experimental fields (west and east) of similar sizes, shown in a Google Earth satellite image captured on Aug. 14, 2019. Higher sand content soil regions (i.e. brighter soil color) and variations in crop growth (i.e., degree of canopy closure) can be seen.

2.2 Soil, field elevation and weather data

The spatial variability of soil texture in the field is quite large due to both alluvial and seismic activities. As soil texture is strongly correlated to EC_a (Sudduth et al. 2003), soil EC_a data were collected on May 9, 2016 using a Veris 3100 instrument (Veris Technologies, Salina, KS) following procedures described by Sudduth et al. (2003). The elevation variation of the field was measured using a Global Navigation Satellite System (GNSS) receiver (Geo 7X, Trimble Navigation Ltd., Westminster, Colorado, USA) and a network-based GNSS correction service that provided 10 cm or better accuracy in 2018. The field elevation increases from 86.85 m on the north side to 88.37 m above mean sea level on the south side, as shown in Figure 2.2.

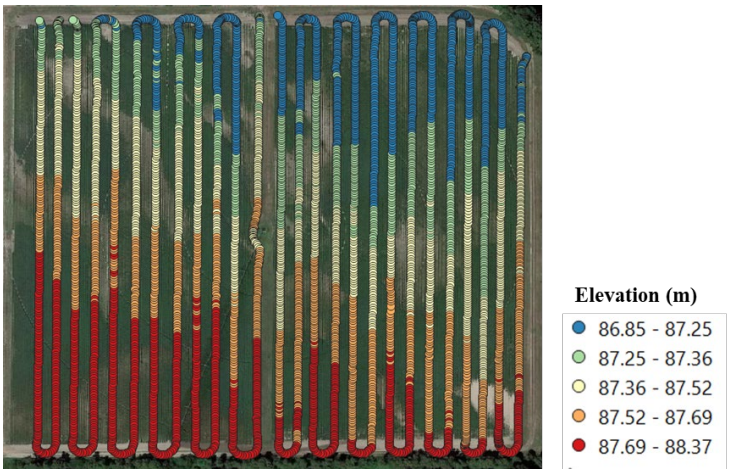

Figure 2.2: Field elevation.

Figure 2.3 shows the cumulative precipitation and daily average temperature from May 1 to October 31 from 2017 to 2019, retrieved from an approximately 400 m nearby weather station (http://agebb. missouri.edu/weather/).

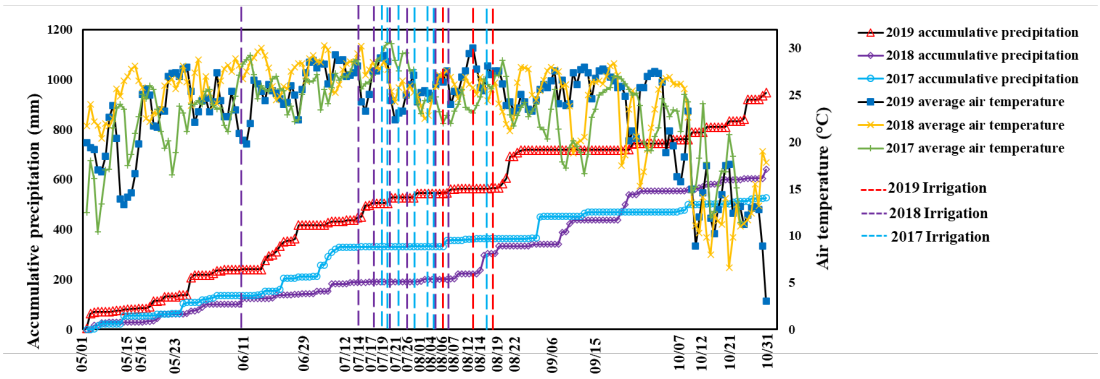

Figure 2.3: Cumulative precipitation and the daily average temperature of the experimental field from May 1 to October 31 in 2017, 2018 and 2019. The data were obtained from a 400 m nearby weather station. The red and purple dashed lines show the irrigation dates. Irrigations were on parts of the field as described in Vories et al. (2020)

The accumulated growing degree days (GDD) were calculated by Eq. 2.1 (Main, 2012; Thompson et al., 2019):

$$GDD = \frac{T_{max} - T_{min}}{2} - 15.6 \qquad (2.1)$$

where T_{max} and T_{min} are the highest and lowest temperature (ºC) of each day. The accumulated GDD and the accumulated precipitation in each month from May to October are shown in Figure 2.4a-b. The accumulated GDD during 2017 to 2019 were similar to the 10-year (2009-2019) average accumulated GDD with the exceptions of being slightly lower in Aug. in 2017, higher in May and June 2018 and September 2019 (Figure 2.4a). However, the accumulated precipitation in each month from 2017 to 2019 was quite variable and different from the 10-year average accumulated precipitation. In the early part of the season, precipitation was lower than average in September in 2017 and from May to July in 2018, but higher from May to July in 2019 (Figure 2.4b). The highest monthly precipitation was in August 2017, September in 2018 but May in 2019.

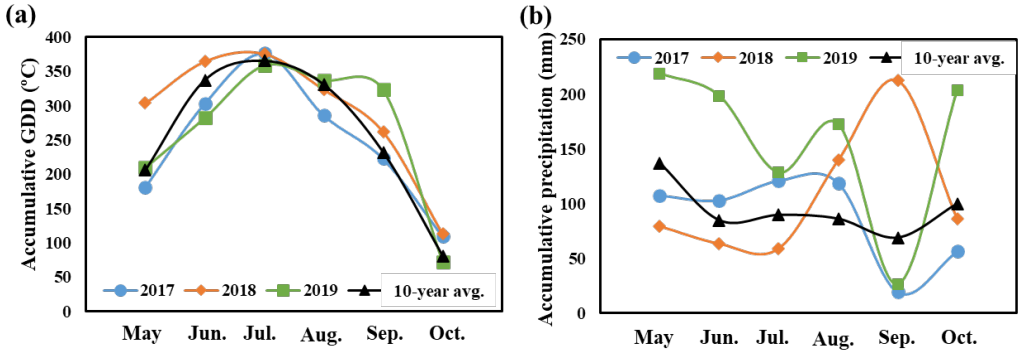

Figure 2.4: Monthly accumulative GDD (a) and monthly accumulative precipitation (b) in 2017-2019 with the 10-year (2009-2019) averages

2.3 Crop management and cotton yield data

Cotton cultivar PHY 333WRF for 2017E (the east field), PHY 375 WRF for 2018W (the west field), PHY 320 WRF for 2019E and PHY 390 WRF (Dow Agrosciences, Indianapolis, IN, USA) for 2019W were planted on bedded soil using a commercial planter (John Deere 1700, Moline, IL, USA) with a GPS system. The planting dates were May 15, 2017, May 16, 2018 and May 15, 2019. There were 152 cotton rows on the east side and 148 cotton rows on the west side with a row spacing of 0.97 m.

A Valley 6000 center pivot irrigation system with zone control variable rate irrigation (VRI; Valley Irrigation, Valley, NE, USA) was used to conduct site-specific irrigation based on the needs of crops and different treatments, including no irrigation, that was described in Vories et al. (2020). The amount of irrigation water applied to different areas of the fields was recorded. As the fields were part of an irrigation study, all treatments other than irrigation (e.g., fertility, pest management) were applied uniformly to the entire field.

Cotton was harvested using a four-row cotton spindle picker (Case IH 2155, Racine, WI, USA) on October 6 & 7, 2017, October 12, 2018 and October 10, 2019. An Ag Leader Insight yield monitor system (Ag Leader Technology, Ames, IA, USA) recorded geo-referenced yield data separately for each row on a 1-s interval at approximately 6.5 km h^{-1}, or approximately 1.8 m of row per data point. The location of each data point was determined with a GNSS receiver (GPS 1500, Ag Leader Technology, Ames, IA, USA) using wide area augmentation system (WAAS) differential correction, which is expected to provide 150–200 mm pass-to-pass accuracy (Ag Leader Technology, 2011) in 2017 and 2018. An Ag Leader GPS 7500 receiver with TerraStar-C Pro differential correction, with pass-to-pass accuracy of 30 – 60 mm (Ag Leader Technology, 2019) was used in 2019. The spatially referenced yield data were managed using Ag Leader SMS Basic version 18.50 and ArcGIS 10.4 for Desktop (Esri, Redlands, CA, USA).

2.5 Literature cited

Ag Leader Technology, 2011. GPS differential sources explained.

Ag Leader Technology, 2019. GPS 7500 and GPS 6500 correction signal comparison.

Main, C.L., 2012. W287 Cotton Growth and Development. Institute of Agriculture, The University of Tennessee.

Sudduth, K.A., Kitchen, N., Bollero, G., Bullock, D., Wiebold, W., 2003. Comparison of electromagnetic induction and direct sensing of soil electrical conductivity. Agronomy Journal 95, 472-482.

Thompson, C.N., Guo, W., Sharma, B., Ritchie, G.L., 2019. Using normalized difference red edge index to assess maturity in cotton. Crop Science 59, 2167-2177.

Vories, E., O'Shaughnessy, S., Sudduth, K.A., Evett, S., Andrade, M., Drummond, S., 2020. Comparison of precision and conventional irrigation management of cotton and impact of soil texture. Precision Agriculture, 1-18.

Chapter 3. COTTON EMERGENCE EVALUATION AND THE SOIL EFFECTS ON EMERGENCE

3.1 Abstract

Crop emergence is an important agronomic factor for making field management decisions, such as replanting, that are time-sensitive and need to be made at very early stages. Crop emergence, evaluated using plant population, stand count and uniformity, is conventionally quantified manually, not accurate, and labor and time-intensive. Unmanned aerial vehicle (UAV)-based imaging systems are able to scout crop fields rapidly. However, data processing can be too slow to make timely decision making. The goal of this study was to develop a novel image processing method for processing UAV images in nearly real-time. In this study, a UAV imaging system was used to capture RGB image frames of cotton seedlings to evaluate stand count and canopy size. Images were pre-processed to correct distortions, calculate ground sample distance and geo-reference cotton rows in the images. A pre-trained deep learning model, *resnet*18*,* was used to estimate the stand count and canopy size of cotton seedlings in each image frame. Results showed that the developed method could estimate stand count accurately with R^2 = 0.95 in the test dataset. Similar results were achieved for canopy size with an estimation accuracy of R^2 = 0.93 in the test dataset. The processing time for each image frame of 20 M pixels with each crop row geo-referenced was 2.22 s (including 1.80 s for pre-processing), which was more efficient than traditional mosaic-based image processing methods. An open-source automated image-processing framework was developed for cotton emergence evaluation and is available to the community for efficient data processing and analytics.

Keywords. Emergence evaluation; stand count; row geo-reference; real-time processing

3.2 Introduction

Crop emergence is an important agronomic factor for field management in early stages, which can be assessed using plant population, stand count, uniformity and seedling size (Sansone et al., 2002; Supak, 1990). Accurate and timely assessment of crop stand count and seedling size at the emergence stage may help farmers make important field management decisions (e.g., replanting) to reduce production loss (Goodell et al., 2015). Acquisition of high-resolution site-specific crop emergence information is the baseline for implementing precision field management. Meanwhile, accurate crop emergence information can be used to understand the impact of soil and environment on crop emergence (Forcella et al., 2000; Ghassemi-Golezani and Dalil, 2014). Conventionally, crop stand count is assessed through visual observation (manual counts) in a small number of sampling sites (Wiles and Schweizer, 1999), which is time-consuming, labor-intensive, and not suited to cover a large production field.

To improve efficiency and accuracy, advanced proximal and remote sensing technologies have been developed to assess crop emergence. For example, Jin et al. (2017) and Liu et al. (2017) used ground vehicle-based imaging systems to assess wheat stand count in field conditions. However, ground vehicle-based systems have many limitations when they are used in full-scale crop production, such as being slow and affected by ground conditions (e.g., wet soil or narrow-row cropping systems). In recent years, unmanned aerial vehicle (UAV)-based imaging technology has been tested as a high-throughput tool for crop emergence assessment in various crops as summarized by Feng et al. (2020). Some examples include the assessment of wheat density (Jin et al., 2017; Sankaran et al., 2015),

cotton uniformity (Feng et al., 2019a), and stand count in cotton (Chen et al., 2018; Feng et al., 2019a), corn (Varela et al., 2018), potato (Sankaran et al., 2017) and rapeseed (Zhao et al., 2018).

The published studies used similar approaches to process UAV imagery data, i.e., using commercial UAV image processing software, such as Agisoft PhotoScan (Agisoft LLC, St. Petersburg, Russia) and Pix4D (Pix4D S.A., Lausanne, Switzerland), to generate orthomosaic images before further processing. The procedure of generating orthomosaic images includes image feature detection, matching, alignment and blending based on mosaic blending models as described by Brown and Lowe (2003), which may take a very long time (days or weeks) and require extensive computational resources. For example, it took more than two weeks to develop an orthomosaic image using 2000 images of 4864 × 3648 pixels using Agisoft in one of our projects. The software was running in a workstation desktop computer (Model Dell Precision Tower 5810, Dell, Round Rock, TX, USA) configured with an Intel Xeon E5 (1630 v3) 3.70 GHz central processing unit (CPU), 32GB random-access memory (RAM) and an NVIDIA Quadro K1200 4GB graphics processing unit (GPU). Crop seedlings are usually small and require high-resolution images to capture sufficient information, which results in a large number of images for mosaic processing and makes it challenging to make timely decisions. The challenge in the timely processing of imagery data becomes one of the most critical barriers for adopting UAV imagery in applications of crop emergence assessment (Forcella et al., 2000; Supak, 1990). Although leveraging high-performance computing or cloud computing resources may provide an alternative solution, it requires expensive and complicated infrastructure that may not be feasibly or economically accessible by most users. Therefore, there is a pressing need to

develop a cost-effective solution for timely image processing and real-time decision making.

Current studies related to crop emergence using UAV imagery focus on stand count and uniformity (Feng et al., 2019a). Crop seedlings were usually segmented by their morphological features from the images to estimate the number of seedlings in a certain row length or area. The image features include canopy area (total number of green pixels) (Gnädinger and Schmidhalter, 2017), leaf polygons (Chen et al., 2018), and major axis length (Jin et al., 2017; Zhao et al., 2018). Template matching with a single plant was another way to count seedlings (Koh et al., 2019). However, the shape, size and overlap (Zhao et al., 2018) of individual seedlings may vary in a large range due to the variation in soil conditions (moisture, temperature, nutrients), cropping system, planting depth and seed quality (Egli and Rucker, 2012; Feng et al., 2019a). Using simple image features or their combinations may not identify seedlings accurately and result in errors in stand count. In addition, most of the published studies defined the seedling clusters (overlapped seedlings) as different regions of interest (ROI) and then used a classification model to estimate the number of seedlings in each ROI. Classification methods need to know the maximum expected plant number in each ROI (Ribera et al., 2017). Feng et al. (2019a) pointed out that there were unbalanced data sets in their study when using the classification method as most of the ROIs included one or two seedlings and only a few ROIs included three or four seedlings. Unbalanced data sets could affect the estimation accuracy (Chawla, 2009). Using regression instead of classification may help to reduce the effect of the above problems (Ribera et al., 2017).

Advanced data processing technology, deep learning (DL), has been increasingly used to process imagery data collected in agricultural applications (Kamilaris and Prenafeta-Boldú, 2018) Deep learning models have been used to extract hidden information from imagery data collected by satellites, UAVs and ground robotic systems to monitor crop development and predict yield (Humphrey et al., 2012; Nanni et al., 2017). In addition, the multilayer structure of DL models works well for complex nonlinear problems (Nielsen, 2015). There are two ways to develop a DL model: using the network architectures developed and tested by other research teams, or designing a specific network architecture (Kamilaris and Prenafeta-Boldú, 2018). Designing a specific DL network for a project requires a sufficiently large dataset for training and validating the models (Erhan et al., 2009), which is a challenge in agricultural studies. On the other hand, a number of successful and popular DL models (pre-trained DL models) have been tested and validated to have high efficiency and can be transferred to different tasks (transform learning model) (Pan and Yang, 2009). Transform learning models have been used in many studies and are potentially able to improve the efficiency and reduce the time to train the models (Ayyachamy et al., 2019; Kamilaris and Prenafeta-Boldú, 2018), including in many agricultural studies (Fu et al., 2020; Gao et al., 2020; Li et al., 2019). Various successful and popular deep learning models, such as AlexNet (Krizhevsky, 2014), VGG (Simonyan and Zisserman, 2014), GoogleNet (Szegedy et al., 2015), and ResNet (He et al., 2016), have been used to process complex data from agriculture. The applications include weed detection (Dyrmann et al., 2017; Dyrmann et al., 2016), fruit detection and counting (Bargoti and Underwood, 2017; Chen et al., 2017; Rahnemoonfar and Sheppard, 2017) and plant disease detection (Ghosal et al., 2018; Mohanty et al., 2016). In addition, transform

learning models have been used to evaluate plant stand count and showed potential for improved accuracy (Ribera et al., 2017).

This study focused on developing an efficient imagery data processing and analysis framework for timely evaluation of cotton emergence using UAV-based RGB imagery and deep learning technology. This study was different from previously published studies in the approach of directly processing individual image frames rather than developing orthomosaic images to reduce the processing time. The specific objectives included (1) developing a pre-processing pipeline to segment and geo-reference crop rows in each individual image frame; (2) implementing a deep learning model to estimate the cotton stand count and canopy size; and (3) developing a framework for automatically generating geo-referenced emergence maps in cotton.

3.3 UAV system and experimental design

To imaging the small size cotton seedlings, a high image resolution UAV system was used for the cotton emergence evaluation study. Imagery data were collected using a UAV imaging system (DJI Phantom 4 Advanced, DJI, Shenzhen, Guangdong, China). The onboard RGB camera has a focal length of 8.8 mm and the dimensions of the imaging sensor were 12.8 mm × 7.2 mm with 20M effective pixels. The spatial resolution of the images was 2.7 mm pixel^{-1} at 10 m AGL with a frame size of 3648×4864. A UAV control app (Autopilot, Hangar Technology, Austin, TX, USA) was used to plan flight paths, set waypoints, flight speed (7.5 km h^{-1}), and height (10 m above ground level, AGL) before flying. The camera collected images at a snapshot rate of 2 s per image (i.e. 0.5 frames per second), with a 60% image overlap in both sideward and forward directions. Imagery data

were collected at near solar noon (around 1 pm Central Daylight Time, CDT) 16 days after planting (DAP) on May 31, 2019. The weather conditions during imaging are shown in Table 3. 1, which indicates a mild wind speed and negligible variation in the environment (air temperature, relative humidity and solar irradiance). The onboard GPS system on the UAV continuously recorded the coordinates and altitude of the imaging system and provided geo-referencing for each image frame as part of the image metadata. Geo-referenced images were downloaded after the flight for further processing.

Table 3. 1: Weather conditions during imaging measured by the nearby weather station

Air temperature (ºC)	Relative humidity (%)	Wind speed (m s^{-1})	Solar irradiance (W m^{-2})
26.8±0.4	48.7±0.6	2±0	864±68.5

Ground truth and reference data including ground reference points (GRPs), stand count and seedling size, were collected on the day of the UAV flight. In this study, 28 GRPs (Figure 3.1) were set in the field, including 16 fence posts (~ 1.1 m in height) with white-black polytechnic boards (30 cm × 30 cm) and twelve 53 cm × 53 cm squares constructed with half-inch polyvinyl chloride (PVC) pipes. A ground stake was placed at each GRP to mark its position in a way that could be recognized during the growing season (Figure 3.1c). A real-time kinematic (RTK) survey kit (REACH RS+, Emlid Ltd., Saint Petersburg, Russia) with a ReachView app (Emlid Ltd.) was used to obtain the Global Positioning System (GPS) coordinates of the 28 GRPs. At each GRP, six flags were used to mark six 1-m intervals of crop seedlings in two cotton rows as shown in Figure 3.1a and Figure 3.1b. The number of seedlings in each 1-m interval was counted manually to serve as ground truth data for stand count estimation. Meanwhile, a tape measure with a precision

scale of 1 mm was placed along the cotton row to provide a reference to calculate ground sampling distance (GSD), which is defined as the number of pixels per meter. A digital camera on a cell phone (iPhone 6s, Apple Inc., Cupertino, CA, USA) was used to take videos of the crop rows while being held manually at a height of about 0.5 m AGL with the camera facing down. Cotton stands were counted by playing back the videos and canopy size (top view) was calculated using the GSD from the tape measure.

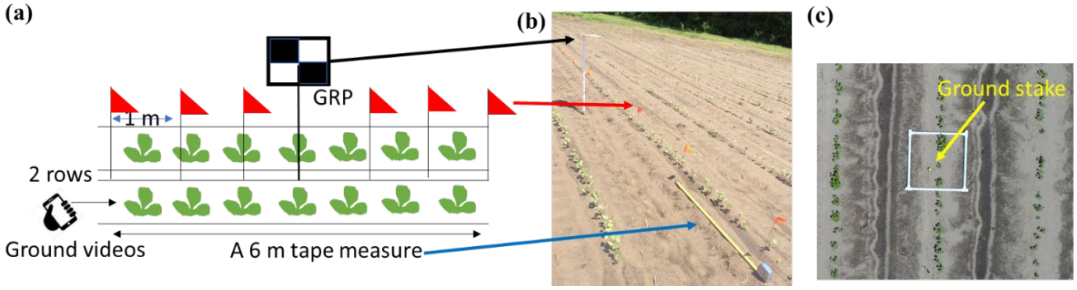

Figure 3.1: Illustration of the field experiment setup. (a) and (b) show one of the 28 ground reference points (GRPs) that include two 6-m crop rows, a fence post and red flags marking 1-m intervals. The ground videos were taken using a cell phone camera. (c) UAV image showing a PVC pipe square with one ground stake inside.

3.4 UAV image pre-processing

UAV images may have tilt/perspective angles to the ground (crop canopy) and different GSD due to variation in flight attitude and altitude of the UAV. Therefore, pre-processing is required for three main purposes: 1) image distortion correction; 2) calibration of GSD in each image; and 3) geo-referencing each crop row.

Distortion calibration

There are two types of distortions in photography, i.e. optical distortion due to the camera lens and perspective distortion due to the position of the camera relative to the

scene. Both distortions will affect the accuracy of geometric measurements using UAV photogrammetry. In this study, each image frame included about nine to fifteen cotton rows depending on the flight altitude. The GSD of cotton rows at the edge of each image is affected by both optical distortion (including radial and decentering lens distortions) and perspective distortion. The optical distortion of the onboard camera was corrected through the calibration procedure using the DJI Assistant 2 software (DJI, Shenzhen, Guangdong, China) before fights. To evaluate the calibration results of the DJI Assistant 2 software, a checkerboard with nine rows and 12 columns of squares, each 60 mm × 60 mm, was used to calculate the level of distortion following the procedure described by Zhang (2000). Images including different views (orientations) of the checkerboard were taken and then the corners of the squares in the checkerboard were identified automatically. Since the images of the checkerboard were taken outdoors, the uneven sunlight and the complex background made corner detection challenging. A more robust method for checkerboard corner detection described by Geiger et al. (2012) was used for automatic corner detection. The corners of the squares were used as features to estimate the camera intrinsic matrix and distortion parameters based on the maximum likelihood criterion. The radial distortion coefficient k1 of the lens was used to describe the level of distortion (Zhang, 2000). There is no radial distortion when $k1$=0. The images have pincushion distortion when $k1$ is positive, and barrel distortion when $k1$ is negative. Perspective distortion of each image was explained using the differences in cotton row spacing in the edge and in the middle of images and is described in the following Chapter.

Quantification of cotton row spacing

To calculate the GSD of each image, a dynamic ground reference object with a known dimension is needed. In field conditions, it is challenging to set a sufficient number of artificial objects to be captured by each frame. However, in production fields, row crops, including cotton, are planted using commercial planters with fixed row spacing, which can be used as a ground reference object for calculating the GSD of each image frame. The 12 PVC pipe squares with a side length of 0.53 m were randomly distributed in the field to provide secondary ground reference objects for validating the GSD calculated using row spacing.

To calculate row spacing in the images, the first step was to segment each row and identify their central lines. Figure 3.2 shows the procedures of crop row detection, including conducting decorrelation stretch and standard Hough transform (SHT) (Duda and Hart, 1972). Image decorrelation stretch is designed to reduce the inter-channel correlation and enhance (stretch) the color difference in a multiple-channel image for object segmentation and feature detection (Gnädinger and Schmidhalter, 2017). The decorrelation process was conducted using the decorrstretch function in Matlab (version 2018a, MathWorks, Natick, MA, USA). After decorrelation, the pixel values in the green channel of images showed a large difference between crops and soil; therefore, all pixels > 180 were considered as cotton seedlings and set as "1" in a binary image as shown in Figure 3.2b. The SHT was applied to the binary images to search long lines that were considered to be crop rows (Feng et al., 2020). The SHT process was conducted using the hough function in Matlab that returned two parameters for each detected line, i.e. the distance r from the origin coordinates of the image to the detected cotton row, and the angle θ of the detected cotton row to the vertical axis of the image. Angles within an image might be

slightly different for each row and the median θ was used for each image. The images then were rotated -θ degrees to obtain cotton rows aligned with the vertical axis of the images, as shown in Figure 3.2c. Row spacing was calculated based on the r difference between two neighboring rows, denoted by r_i. As shown in Figure 3.2d, all cotton rows in an image were split into three groups automatically based on the r values, i.e. left two rows (two smallest r), right two rows (two largest r) and middle rows. This grouping was selected to keep more than 50% of an image as the middle rows and less than 50% as the edge rows. There were at least nine crop rows in each image frame based on our statistical analysis in this study (results not shown). A t-test was conducted to test the difference in row spacing between the edge rows (left and right two rows) and middle rows, and perspective distortion was detected by a significant difference. Since the paired t-test required an equal sample size in each group, a random resampling process was conducted before the t-test. The standard deviation (δ) of row spacing across all images was used to describe the variation of the cotton row spacing. After the row spacing was measured, the GSD of the image was calculated as the ratio of the number of pixels to the true row spacing, which was 0.97 m in this case.

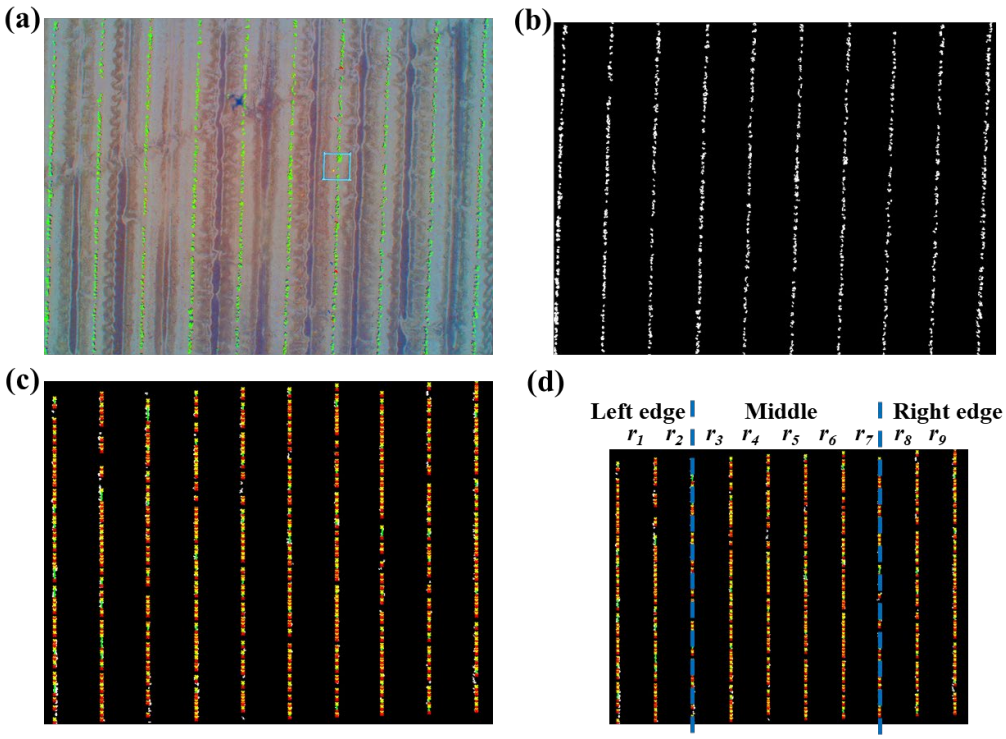

Figure 3.2: Illustration of cotton row detection. (a) Image after decorrelation stretch procedure showing the substantial difference between pixel values of crops and soil. (b) The corresponding binary image after soil removal using a threshold. (c) Cotton rows were detected using a standard Hough transform (SHT). (d) Row spacing is denoted by r_is. Cotton row spacings in an image were classified as left edges (two left row spacings, r_1 and r_2), middle (r_3-r_7), or right edges (two right row spacings, r_8 and r_9) to test perspective distortion.

Geo-referencing cotton rows

The accuracy of the UAV GPS was evaluated by comparing the horizontal coordinates of the ground stake in each GRP with those measured using the RTK receiver. As shown in Figure 3.3a, the northing and easting distances in pixels between the image geometric center and the ground stake were measured first. Then, those distances in pixels were transformed to distances in meters using the GSD calculated based on row spacing.

The GPS coordinates of the ground stake were calculated based on the above calculated distances in meters and the image GPS coordinates using Eq. 3.1 and Eq. 3.2 (Bugayevskiy and Snyder, 2013; Snyder, 1987).

$$\Delta^1_{lat} = 111132.92 - 559.82cos2\varphi + 1.175cos4\varphi - 0.0023cos6\varphi \quad (3.1)$$

$$\Delta^1_{long} = 111412.84 - 93.5cos3\varphi + 0.118cos5\varphi \quad (3.2)$$

where Δ^1_{lat} and Δ^1_{long} are the lengths in meters of a 1-degree change of latitude and longitude, and φ is the latitude in radians. The constants 111132.92 and 111412.84 represent the average estimation for Δ^1_{lat} and Δ^1_{long} based on earth's radius and ellipsoid parameters. However, the earth is an irregular ellipse and Δ^1_{lat} and Δ^1_{long} change with latitude. The other parameters are the adjustment of these changes in different latitudes. The accuracy of image GPS coordinates was calculated as the distance between the coordinates of the ground stakes measured using the two systems and was calculated using the Haversine formula as explained in Lipan and Groza (2010) and Monawar et al. (2017).

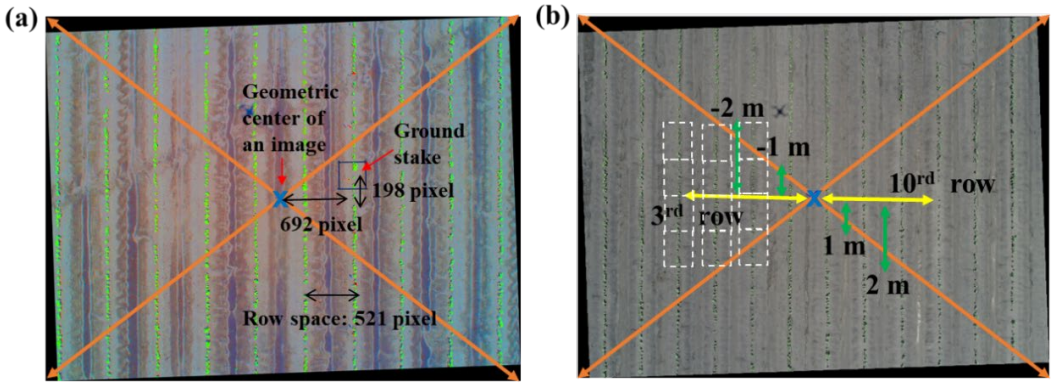

Figure 3.3: Illustration showing the location of a ground stake away from the center of an image and the location calculation for each cotton row. (a) Calculation of the ground stake coordinates from the UAV GPS system. (b) Calculation of GPS coordinates of 1-m seedling segments in each cotton row. The blue 'x' is the image geometric center.

Eq. 3.1 and Eq. 3.2 were also used to calculate the GPS coordinates of each 1-m seedling segment (white dashed boxes in Figure 3.3b) of each row in an image based on the UAV GPS system. GPS coordinates of the white boxes were assigned based on their distances from the geometric centers of the image frame. Since the images had > 60% overlap in both the sideward and the forward directions, only middle rows were used in the following processing, i.e., seedlings within 2 m from the geometric center in the north-south direction.

Evaluation of distortion correction and estimated row spacing

One hundred and six (106) images of the checkerboard were processed to validate the calibration results of optical distortion using the DJI Assistant 2 software. In this study, $k1$=0.0205 was obtained, indicating the optical distortion was small enough to be negligible. Thirty-eight images that included PVC pipes were used to evaluate the variation of the row spacing of 334 rows, resulting in a mean of 99.0 cm with a standard deviation of 3.8 cm. This result showed that the variation of row spacing was small and usage of cotton row spacing as the reference of GSD was reasonable.

The same thirty-eight images that included 334 rows were also used to test the perspective distortion of an image. Table 3.2 shows the means and standard deviations of row spacing of left, middle and right edge rows in the images (Figure 3.2). It can be seen that the mean row spacing at the middle of images was slightly larger than that of left and right edge rows. A resampling t-test with a resampling size of 1,000 showed that there was no significant difference among the three locations at a 5% significance level, which also indicated that the perspective distortion was small enough to be negligible.

Table 3.2: Mean and standard deviation of row spacing of edge and middle rows in images. The resampling t-test indicates that there was no significant difference (p-value < 0.05) in row spacing among the rows at different locations of images.

	Left two rows	Middle rows	Right two rows
Mean ± std (cm)	98.80 ± 3.64	99.28 ± 4.03	98.70 ± 3.30

3.5 Evaluation of cotton stand count and canopy size

Introduction to convolutional neural networks

The convolutional neural network (CNN) is a DL model designed in combinations of different numbers of convolution layers, pooling layers, activation layers, and full connection layers (Nielsen, 2015). Convolution layers and pooling layers include filter boxes that scan the input images using a sliding window to generate image feature maps, as shown in Figure 3.4a. A filter box is a parameter matrix. It moves from the top to the bottom and from left to right with a specific moving stride to calculate the sum of multiplication of the input image with the parameter matrix. This process can extract the input image features while keeping the spatial correlation of image features. Pooling layers extract the mean or maximum pixel values of the regions while they move. Full connection layers calculate the sum of multiplication of the input values with layer parameters, shown as Figure 3.4b. Activation layers include nonlinear functions, such as the sigmoid function, logistic activation function, or rectified linear unit (ReLU) function (Nielsen, 2015).

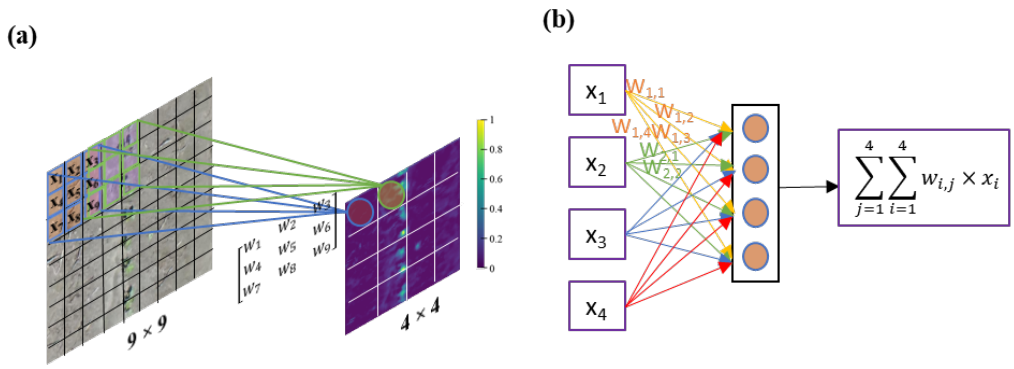

Figure 3.4: Illustration of the principle of convolution layers and full connection layers of the deep learning model. (a) Convolution layers include a 3 × 3 filter with the parameters w_i. The input image size is assumed 9 × 9 and the moving stride is 2, resulting in the output of a 4 × 4 feature map. x_i is one of the pixel values of each 3 × 3 region that is used to calculate outputs while moving. Each value in the output feature map is calculated by $\sum_{i=1}^{9} \boldsymbol{w_i} \times \boldsymbol{x_i}$. (b) In the full connection layers, $w_{i,j}$ are the parameters, and x_i are the input values. This is a four input and one output full connection layer that is calculated by the formula inside the purple box.

Deployment of transform learning model using resnet18

The CNN model used in this study was based on a widely used pre-trained CNN model *resnet* developed by (He et al., 2015). The architecture of the CNN model is shown in Figure 3.5. The *resnet* model was chosen from many popular pre-trained models (such as VGG, DenseNet and AlexNet) due to the high estimation accuracy and low computation resource requirement. The *resnet* was trained and validated using the ImageNet dataset (Russakovsky et al., 2015) with a classification capacity of 1000 classes. The *resnet* model can be optimized easily and could achieve higher accuracy with deeper layers because of the residual blocks (He et al., 2016). The *resnet* model has different versions, including 18

layers, 34 layers and 152 layers that are developed to process data of different complexity. The smallest model, *resnet18* was chosen in this study due to the relatively less complex dataset, preferred fast training speed and less computing time. The parameters trained on the ImageNet dataset were selected as the initial parameters as they had strong image feature extraction power (Pan and Yang, 2009) for low-level features (such as dots, lines, corners and textures) to avoid training models from scratch and to reduce the required time. Parameters in all layers of the model were fine-tuned using the imagery dataset from this study.

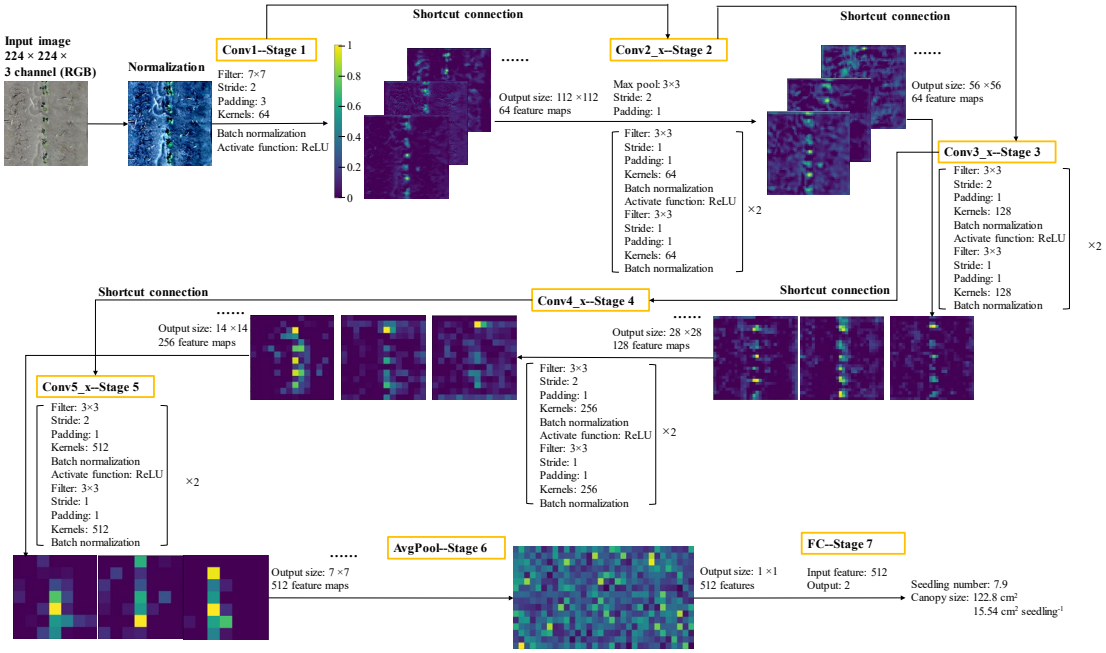

Figure 3.5: The architecture of *resnet18*, as applied to the estimation of stand count and seedling size.

The *resnet18* model requires input images of 224 × 224 pixels in three channels (red, green and blue). Therefore, images collected in this study were resized to the required dimensions. The pixel values in the three channels ([R, G, B], pixel values ranged from 0-255) of the input images were normalized to the range of [0, 1] by dividing by 255 (i.e.,

[R/255, G/255, B/255]). The pre-trained *resnet18* model requires the same normalizing procedure as the original ImageNet training set. Therefore, the imagery data were subtracted [0.485, 0.456, 0.406] and divided by [0.229, 0.224, 0.225], i.e., [(R/255-0.485)/0.229, (G/255-0.456)/0.224, (B/255-0.406)/0.225], which were the mean and standard deviation of the three channels (red, green and blue) of the ImageNet dataset (Russakovsky et al., 2015). The model used five stages of different numbers of convolution layer combinations, batch normalization layers, ReLU activation layers and max pooling layers for feature extraction (He et al., 2016). Shortcut connections were added to this network to provide the residual learning (residual blocks) (He et al., 2016). The last two stages (stages 6-7) were average pooling and full connection layers. The outputs were stand count and canopy size of each seedling based on a regression model. The L1 loss function (|f(x)-y|) was used to minimize errors and search for optimal model parameters (Goodfellow et al., 2016). The model calculated canopy size and stand count simultaneously using one loss function for the parameter optimization. However, the absolute values of canopy size (mean was about 24 cm^2 per seedling) were larger than the stand count (mean was about 12 seedlings m^{-1}), so the L1 loss was defined by Eq. 3.3 to balance the loss of canopy size and stand count. Mean absolute percentage error (MAPE) defined by Eq. 3.4 was used to evaluate the accuracy of the stand count and canopy size estimations.

$$L1\ loss = |\hat{y}_{sc} - y_{sc}| + \beta \times |\hat{y}_{cs} - y_{cs}| \qquad (3.3)$$

$$MAPE = 0.5 \times \left(\frac{|\hat{y}_{sc} - y_{sc}|}{y_{sc}} + \frac{|\hat{y}_{cs} - y_{cs}|}{y_{cs}}\right) \qquad (3.4)$$

where $\hat{y}_{sc}$ is estimated stand count, y_{sc} is the true stand count, $\hat{y}_{cs}$ is estimated canopy size and y_{cs} is true canopy size, β is the ratio of the mean of stand count to the mean of canopy size in the training set.

Deep learning models have provided promising results for agricultural applications in many current studies but with limited potential for interpretation as a "black box" system (Kamilaris and Prenafeta-Boldú, 2018). Several ways have been developed in other studies to explain the mechanisms of DL models (Ghosal et al., 2018; Mohanty et al., 2016). Those included visualization of the DL filters and feature maps, deconvolutional networks (Zeiler and Fergus, 2014), calculation of filters' receptive field (Dumoulin and Visin, 2016), or the Grad-class activation map (Grad-CAM) (Selvaraju et al., 2017). In this study, feature maps of the first two stages in the resnet18 and the Grad-regression activation map (Grad-RAM) (Wang and Yang, 2017) were used to visually interpret the results. The feature maps were the outputs of each filter in each stage of the *resnet18* model (Figure 3.5). All the feature maps outputted from stage 5 (the 512 7 X 7 features outputted from stage 5 in Figure 3.5) were elementally summed with weights that were connected between the outputs of AvgPool in stage 6 (the 512 1 X 1 outputs from stage 6 in Figure 3.5) and the FC in stage 7 (Figure 3.5) to generate the Grad-RAM. This Grad-RAM can localize the discriminative regions of seedlings in images that determined the final estimation of canopy size and stand count (Wang and Yang, 2017).

Data set preparation

A total of 155 images were selected to train and test the DL model. A GRP included two 6-m cotton rows as illustrated in Figure 3.1, resulting in 12×28=336 m of cotton rows in total. Each selected image contained all or a portion of the 6-m crop rows. All the

individual cotton seedlings and seedling clusters in the images were segmented as RoIs (small red boxes in Figure 3.6) using the method developed by (Feng et al., 2020). The number of seedlings in each RoI was counted manually by playing back the recorded videos, and each RoI was labelled using the number of seedlings in the RoI. A few RoIs only contained part of a seedling (one seedling was identified as two separate RoIs) and were labelled as 0.5. To improve the volume of the training dataset, a data augmentation method was used as illustrated in Figure 3.6. Input images were cropped in each image with a length range from 0.7 m to 1.3 m of each cotton row and including different numbers of consecutive RoIs, shown in Figure 3.6 as different colored boxes.

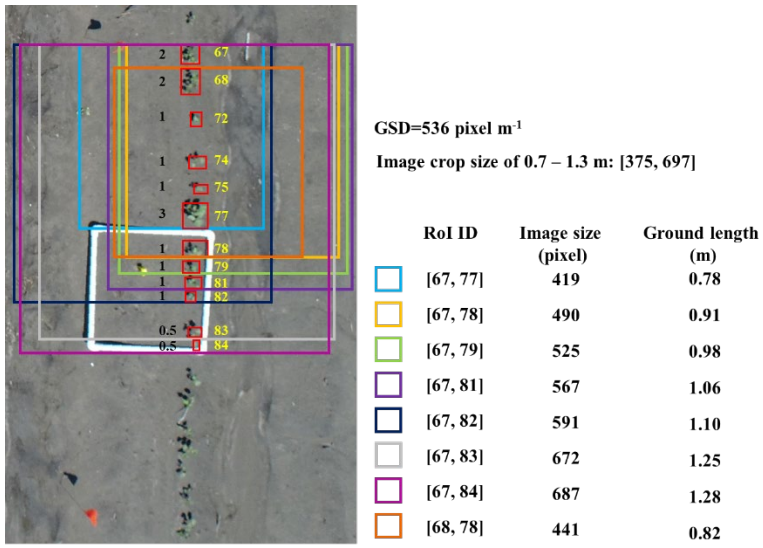

Figure 3.6: Illustration showing the approach used for the preparation of the training data and data augmentation. The red boxes mark the RoIs that contained a single cotton seedling or a cluster of several cotton seedlings. The yellow text gives the ID of each RoI and the black text gives the number of seedlings in each RoI. The different color boxes are the cropping images used as the input images of resnet18 model, where image size varied from 0.7 to 1.3 m, equaling 375 to 697 pixels.

The augmented input images were cropped as a square using the segmentation length as side length, which resulted in the dimensions of input images varying from 375×375 to 697×697 pixels with the length from 0.7 m to 1.3 m (Figure 3.6). The positions of the crop boxes from left to right in each image were random. The square images provided a constant ratio of height to width and minimized the distortion of geometric features due to resizing (to 224 × 224 pixels as required by *resnet18*). The number of seedlings in each input image was the sum of the seedlings of all RoIs. The canopy area (cm^2) of seedlings of each input image was calculated by Eq. 3.5.

$$CA = \frac{N_p \times 10000}{GSD^2} \quad (3.5)$$

where, CA is the canopy area of all seedlings from aerial images (cm^2), Np is the total number of pixels in a RoI of an input image. GSD is the ground sample distance of each input image (pixel m^{-1}). In this study, a total of about 20000 input images were generated, which were split 85% in the training set and 15% in the test set. The model was trained and evaluated using the Pytorch package (pytorch.org) (Paszke et al., 2017).

Performance of deep learning model resnet18

The seedling data set that included more than 20000 input images was used to train resnet18 with 40 epochs. An estimation error of an overall MAPE = 3.3% was obtained in training and an overall MAPE = 4.4% was obtained in testing. Figure 3.7 shows the true values and the predicted values of the test set for cotton stand count and canopy size. For stand count estimation, R^2 = 0.95 and MAPE = 4.3% were obtained, while for canopy size estimation R^2 = 0.93 and MAPE = 4.5% were obtained. These results are promising when compared to similar published studies that reported MAPE from 9.8% to 5.1% (Chen et al., 2018; Gnädinger and Schmidhalter, 2017; Jin et al., 2017; Ribera et al., 2017; Sankaran et

al., 2015; Sankaran et al., 2017; Zhao et al., 2018). Only one of those papers used a deep learning model and estimated stand count with MAPE = 6.7% (Ribera et al., 2017), a value larger than that obtained in this study.

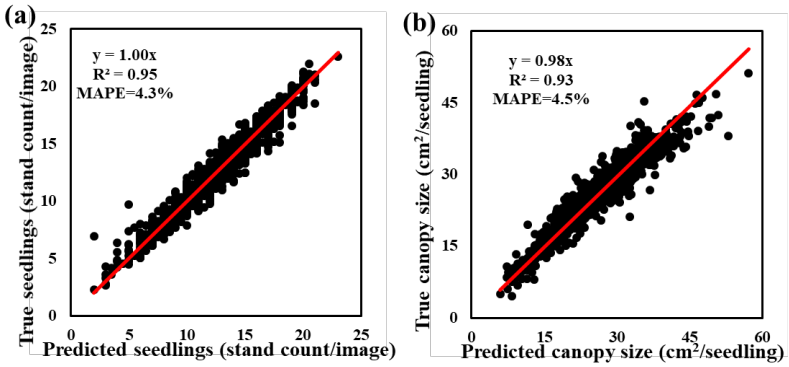

Figure 3.7: Predicted results of (a) cotton stand count and (b) canopy size in the test set

To understand the reasons for such results and potential approaches for improving the accuracy, Figure 3.8 shows the feature maps and the Grad-RAM. Figure 3.8a, e, and i show three examples of input images that had different numbers of seedlings and variations in soil color. It can be seen from Figure 3.8b, f and j that their seedlings were identified with higher values in the feature maps of stage 1. Although the difference between soil and seedlings decreased when the soil color was bright (Figure 3.8i and j), they were segmented correctly in stage 2 (Figure 3.8c, g and k), which not only highlighted the seedlings but also the color differences of the soil. Figure 3.8d, h and l show the seedlings identified in the last convolution layer (stage 5) of *resnet18*. When the number of seedlings in the clusters and the canopy size of the seedlings decreased, the values of the Grad-RAM map decreased. Based on the algorithm of the Grad-RAM calculation, it can be confirmed that the model's final estimation of stand count and canopy size was decided by the regions of seedlings rather than other regions, which was in line with our expectations of the model.

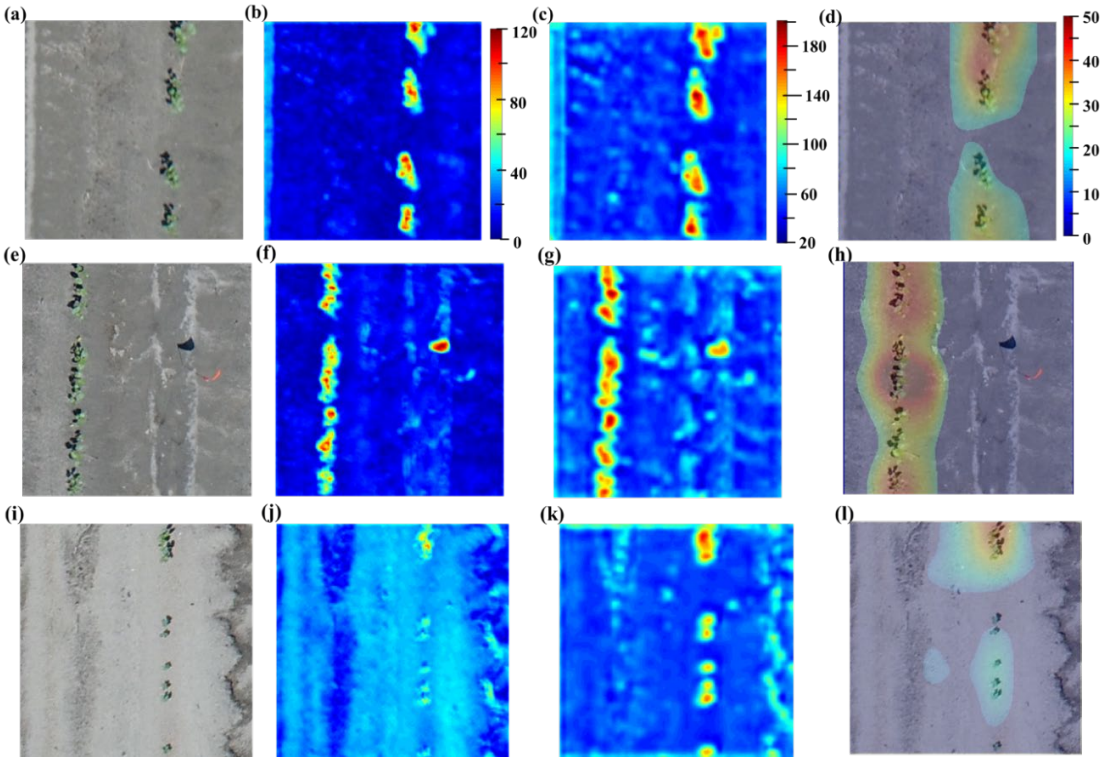

Figure 3.8: Feature maps of stages 1 and 2 of the resnet18 model and the Grad-regression activation map (Grad-RAM) of stage 5. (a), (e) and (i) are three input images; (b), (f) and (j) are the corresponding feature maps of average outputs of 64 filters in stage 1 of the resnet18 model. The higher values in the feature maps mean that these regions were highlighted by the model and that information would be passed to the next layers. The color scale legends of (f) and (j) are the same as that of (b). (c), (g) and (k) are the corresponding feature maps of average outputs of 64 filters in stage 2. The color scale legends of (g) and (k) are the same as that of (c). (d), (h) and (l) are the Grad-RAM extracted from stage 5 of *resnet18*. The color scale legend of (h) and (l) are the same as that of (d).

Vegetation indices such as excess green index (ExG) combined with a dynamic threshold method, Otsu's method, have been used to segment seedlings from the background (Varela et al., 2018; Zhao et al., 2018). Otsu's method can automatically find

an image threshold having the largest difference between two classes and the smallest difference within each class (Otsu, 1979). However, the variability in soil texture and water content may cause soil color differences, which makes it challenging to segment seedlings (Feng et al., 2020). One example of using the ExG with Otsu's method is shown in Figure 3.9a and b, from which we can see that some of the seedlings could not be identified successfully. Figure 3.9c shows an enhanced image of Figure 3.9a using a decorrelation stretch procedure with a global threshold of 180 that improves the performance of segmentation (Figure 3.9d). However, 180 was a global threshold instead of a dynamic threshold (Gnädinger and Schmidhalter, 2017), and needed to be determined by statistical analysis of the crop pixel values or by the image histograms (Feng et al., 2020) that aim to find a global threshold to largely separate the plants and soil. This global threshold is a global optimal value in the whole data set, and there may be some misidentification when using this value. Variations in soil texture and/or moisture level resulted in large differences in soil color and bright soil was detected as crop objects when a global threshold was used. When building the input image set for *resnet18*, visual counting labelled the detected objects that did not include cotton seedlings with a 0 value (that is, misidentified by the global threshold). This manually helped *resnet18* learn to correct the global threshold segmentation error to provide more accurate stand count and canopy size results than methods based only on image segmentation.

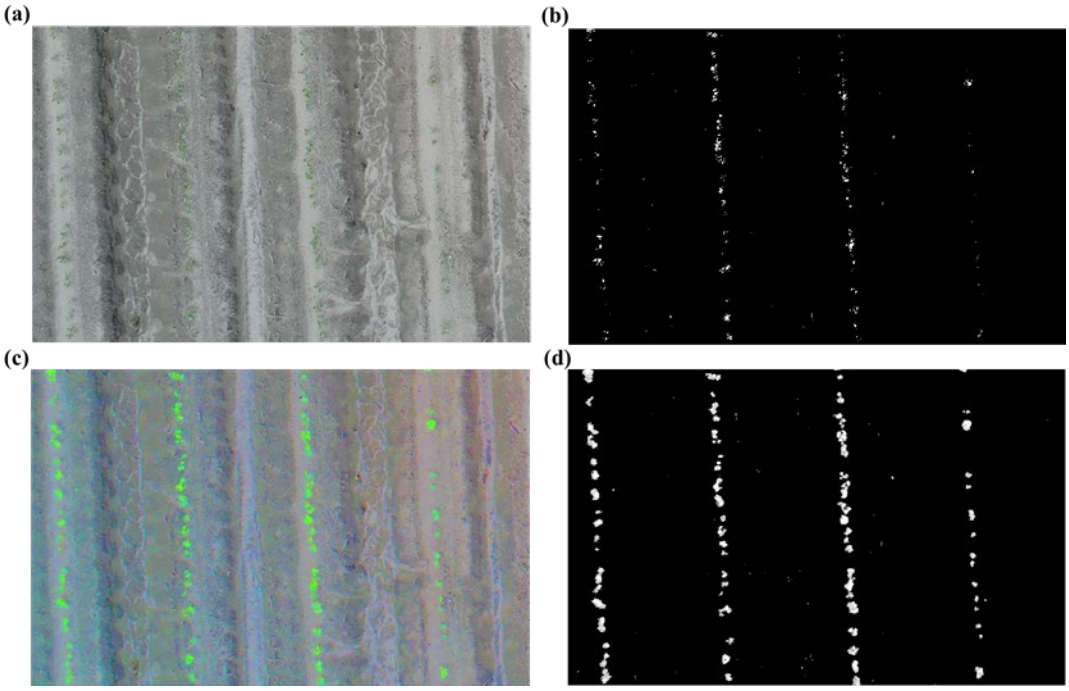

Figure 3.9: Illustration of the complexity of image background removal for segmentation of seedlings due to soil color resulting from variations in texture and/or moisture content over a field. (a) A portion of an RGB image including four crop rows; (b) A binary image showing the segmented seedlings using the ExG and Otsu's method. Some seedlings in the third and the fourth rows were not identified. (c) The pertinent image after using decorrelation stretch procedure and (d) its results of seedling segmentation.

Comparison of resnet18 and other deep learning models

The resnet18 model was running on a desktop configured as an Intel Core i9-9900K 3.60 GHz CPU, an NVIDIA GeForce RTX 2060 GPU with 6GB memory, 32GB RAM and 256 GB solid-state drive (SSD). The performance of the *resnet18* model in estimation accuracy and computation resources for training models was compared with other popular DL models, including *resnet50* (He et al., 2016), AlexNet (Krizhevsky, 2014), VGG11, VGG16 (Simonyan and Zisserman, 2014), SqueezeNet (Iandola et al., 2016) and DenseNet

(Huang et al., 2017). As shown in Table 3.3, the *resnet18* model had a lower use rate of GPU and GPU memory than other DL models except for the SqueezeNet that used fewer computation resources but had a higher MAPE. The size of the parameter file of *resnet18* was smaller than other models except for DenseNet, which had a smaller Parameter file, but used more computation resources and had a longer training time. Except for the VGG16, *resnet18* had a lower test MAPE than other models, however, VGG16 used the most GPU and GPU memory. Therefore, when considering both the low MAPE and low computation resource usage, the *resnet18* model showed more potential to integrate into UAV systems to conduct real time emergence evaluation in the future. AlexNet was the second most promising model based on Table 3.3 and could be considered as an alternative.

Table 3.3: Accuracy and computation resources comparison

Model	Train MAPE (%)	Test MAPE (%)	Training time in s (40 epoch)	CPU (%)	GPU (%)	GPU memory (GB)	RAM (GB)	Parameter file (MB)
*Resnet*18	3.3	4.4	5508	71	60	1.1	7.2	42.6
*Resnet*50	4.9	5.0	11482	69	80	2.1	8.1	89.9
AlexNet	4.3	4.4	4294	71	58	2.1	7.9	217.0
VGG11	6.5	6.9	11389	67	79	4.2	7.5	491.0
VGG16	2.9	3.9	15590	68	88	4.6	7.6	512.0
SqueezeNet	7.0	7.9	4948	71	54	1.2	7.8	2.8
DenseNet	4.6	5.0	18951	71	77	2.3	9.0	27.0

3.6 Development of a framework for evaluation of cotton emergence

An image processing and analysis framework was developed in Python with the MATLAB engine application programming interface (API) for Python. This framework included an easy to use graphical user interface (GUI) to guide users 1) to train the deep

learning model using their own data set, and 2) map their crop emergence. The framework was implemented following the flowchart in Figure 3.10. The process for training the model for specific applications is illustrated in Figure 3.10a, which includes setting GRPs, pre-processing training dataset and training the model. After the model was trained for a specific application, individual images collected in the field could be processed using the procedure illustrated in Figure 3.10b. All the cotton rows in each image frame would be automatically split into geo-referenced 1-m segments based on the GPS information in the metadata of images. The output would be the geo-referenced stand count and canopy area of seedlings in every meter of the row, which would be used to map the emergence of the field.

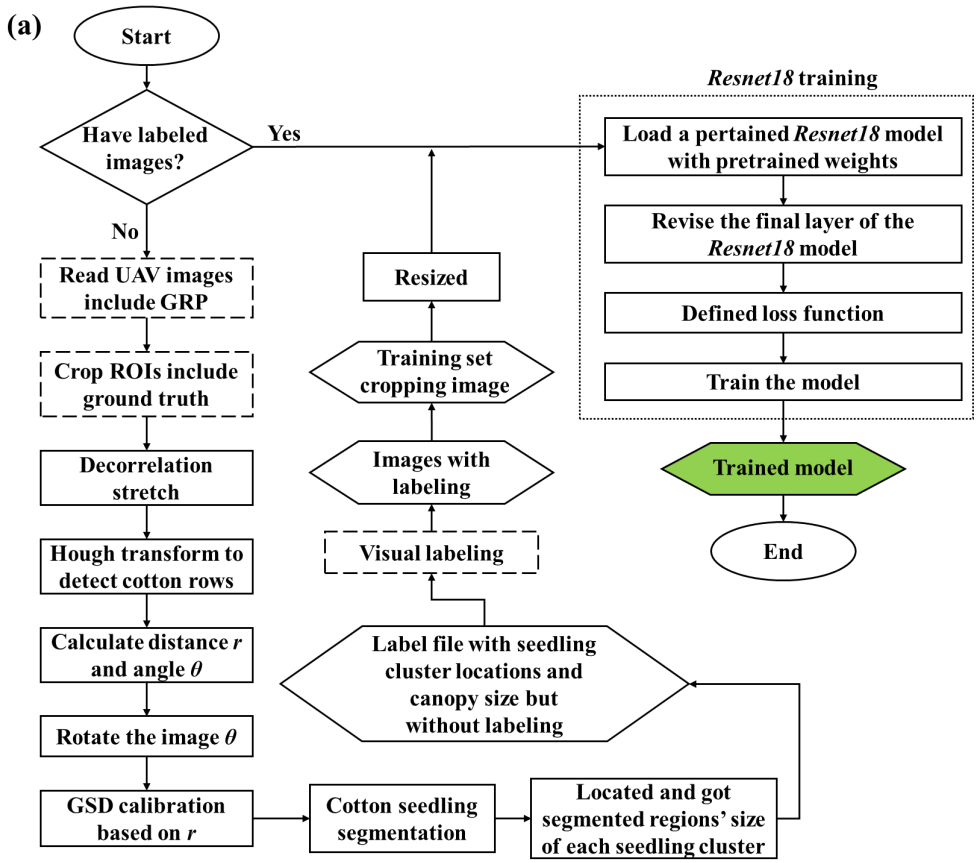

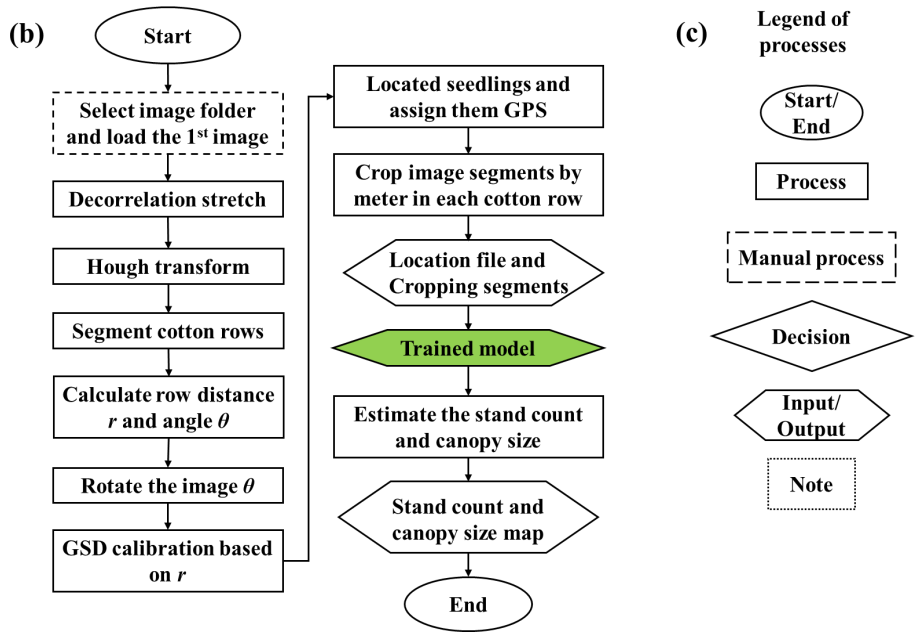

Figure 3.10: Overall processing flowchart. (a) Training procedure; (b) Cotton emergence mapping procedure; (c) Legend used in both (a) and (b).

The data processing framework was developed in a Windows 10 operating system (Microsoft, Redmond, WA, USA) environment using Python software (v3.6), Matlab software (v2018a), Matlab engine API for Python, Opencv package (v3.4) (Bradski, 2000), Scikit-learn package (v0.22) (Pedregosa et al., 2011), NumPy package (v1.16) (Oliphant, 2006), Pandas package (v0.25) (McKinney, 2010) and Pytorch package (v1.2) (Paszke et al., 2017). The framework has been uploaded to GitHub (https://github.com /AJFeng/Emergence-evaluation-Framework) and is ready for testing by other research groups.

Stand count and canopy size mapping

Manually measured and estimated stand count and canopy area per seedling from the 20000 input images were summarized using histograms as shown in Figure 3.11. The mean stand count of manual measurements was 12.5 seedlings per meter with a standard

deviation of 2.2. The mean value of 12.5 was higher than the target seeding rate of 11.0 seed m^{-1}. However, based on field observation by the farm operator, it was found that there was a planter-calibration error and the actual rate was close to the mean value in this study. The figure also shows that the manually measured canopy size per seedling was 24.3 ± 7.0 cm2, indicating a big variation in the canopy size of the measured seedlings. The estimated stand count and canopy area of the tested images for the whole field were shown in Figure 3.11c and d. This showed that the estimated values of the whole field were consistent with our manual measurement with sampling.

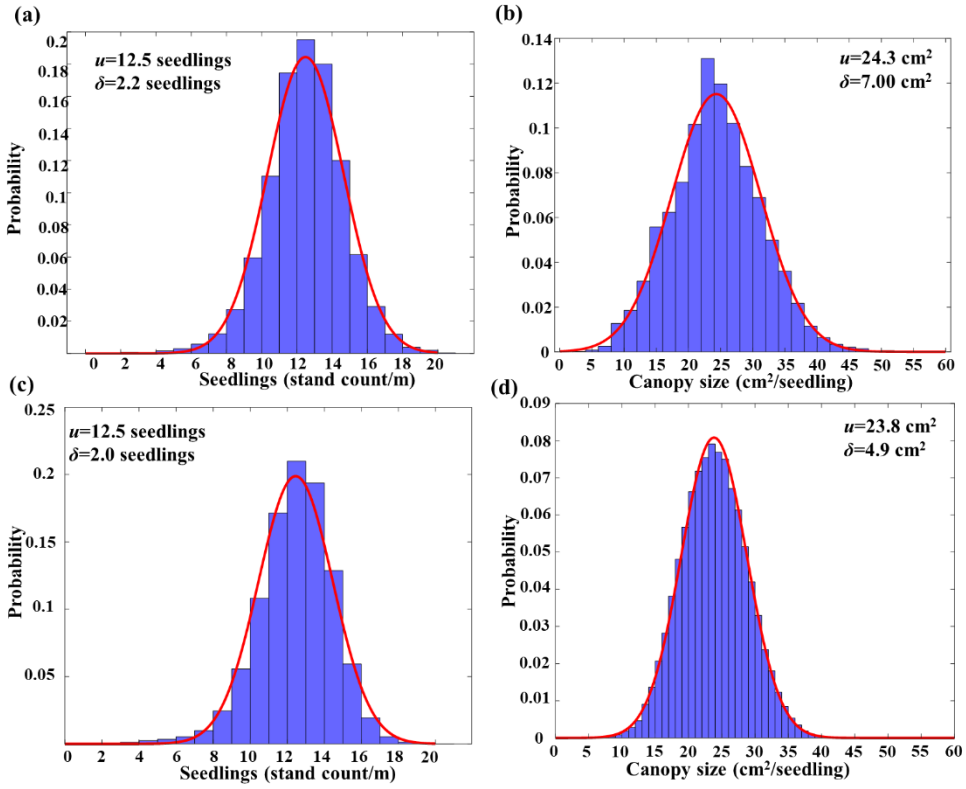

Figure 3.11: Histogram of (a) stand count per meter; and (b) canopy size of the input images that were manually labelled in the GRPs. Predicted results of (c) cotton stand count and (d) canopy size in the whole field.

The stand count and canopy size of the whole field were calculated using the developed model with all collected images. All data were geo-referenced using the metadata of the images and the GPS assignment method in this study. Time spent on the mapping was 2.2 s for each 20 M pixel image frame, which was nearly real-time image processing as the UAV took images every 2 s. When we checked the procedures, it was found that the majority of the processing time (2.2 s) was spent on the process of GPS assignment (about 1.8 s per image). The search of connected regions and SHT algorithm was the most time-consuming steps as this was the limitation of search-based methods.

Geo-referenced stand count and canopy size were imported to the open-source software QGIS (version 3.6, www.qgis. org). Figure 3.12 shows the field maps of cotton stand count and canopy size overlaid on a Google map (Google, Mountain View, CA, USA). Visual observation found that the distribution patterns of two maps (Figure 3.12a and b) were similar to that of the yield map (Figure 3.12c) and the soil EC_a map (Figure 3.12d), i.e., regions of the field with low seedling canopy sizes had low EC_a and low yield. Regions with lower EC_a corresponded to areas with a high-profile sand content (Sudduth et al., 2003) and therefore a low soil water holding capacity, which may affect the crop emergence and growth (Feng et al., 2019b). The quantitative relationship among crop emergence, soil condition and yield need further analysis. The framework developed in this paper can be used to help farmers and researchers to explore the seedling emergence status of their field efficiently and in real-time. Our GPS accuracy test showed that the accuracy of image GPS coordinates based on the 27 ground stakes was 1.72 m with a standard deviation of 1.37 m (1.72 ±1.37 m). This study aimed to enable real-time stand count and canopy size mapping with meter level spatial resolution using UAV-based RGB

images and the geo-location of each image frame may be improved using an RTK GPS, for example, DJI Phantom 4 RTK Drone (DJI, Shenzhen, Guangdong, China) that has an accuracy of 1cm + 1ppm RTK horizontal positioning.

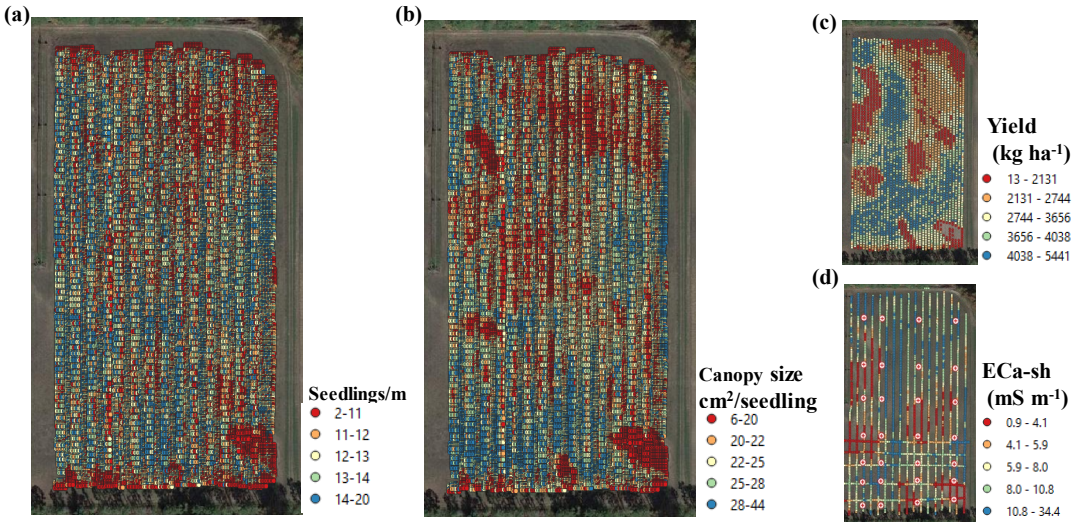

Figure 3.12: (a) Cotton stand count mapping and (b) canopy size mapping; (c) yield map; (d) soil ECa map. The red circles show the 28 GRPs.

The use of the data processing framework

The data processing framework consists of two major tasks, i.e. model training and emergence evaluation. Users may directly use the model provided to map cotton fields having similar data collection conditions to our experiment, i.e., 0.97 m fixed crop row spacing, images collected in about 16 DAP, 2.7 mm pixel-1 and 60% image overlap. Since the fixed row spacing is used for canopy size GSD calibration, the developed method can potentially be used in the conditions of different row spacing and image overlap (from 40% to 80%) when the values of the canopy size map are modified accordingly based on the ratio of our row spacing to users' specific row spacing. Users may have images with different image resolution and collected a few days earlier or later than 16 DAP that have different canopy shapes, sizes and overlapping. It is expected that users would train a

specific model using their own data by following the processing steps described in this paper. The developed framework has not been tested in other crops such as soybean and corn but will be evaluated in future studies. A detailed introduction file that explained the usage of the framework and every item appearing in the GUI was attached with the framework in GitHub.

Figure 3.13 illustrates the major steps to train a customized model using UAV imagery data. All raw image frames that include GCPs should be stored in one folder and would be read automatically by the program. The program would first conduct the seedling segmentation process following the orange mouse icon in Figure 3.13. This would generate: 1) a file that has the row spacing calculation results; 2) a folder including images with segmented crop seedlings; and 3) a file that has the GPS coordinates of the segmented images and waits for users to visually label the cotton seedlings. After visual counting, the image cropping process following the green mouse icon in Figure 3.13 would ask the user to provide the address of the rotated images folder, the labelling file, and the row spacing file (those were all generated from the above orange icon process of the seedling segmentation process) to crop the cotton seedlings into 1-m segmented images to build the training data set. This would generate: 1) input images of the model that were cropped from each individual image frame; 2) a file that included image names of these cropped images and their labels. These would be used to train the *resnet18* model (the training process following the blue mouse icon in Figure 3.13). After this training process, the model trained on the users' own data would be generated.

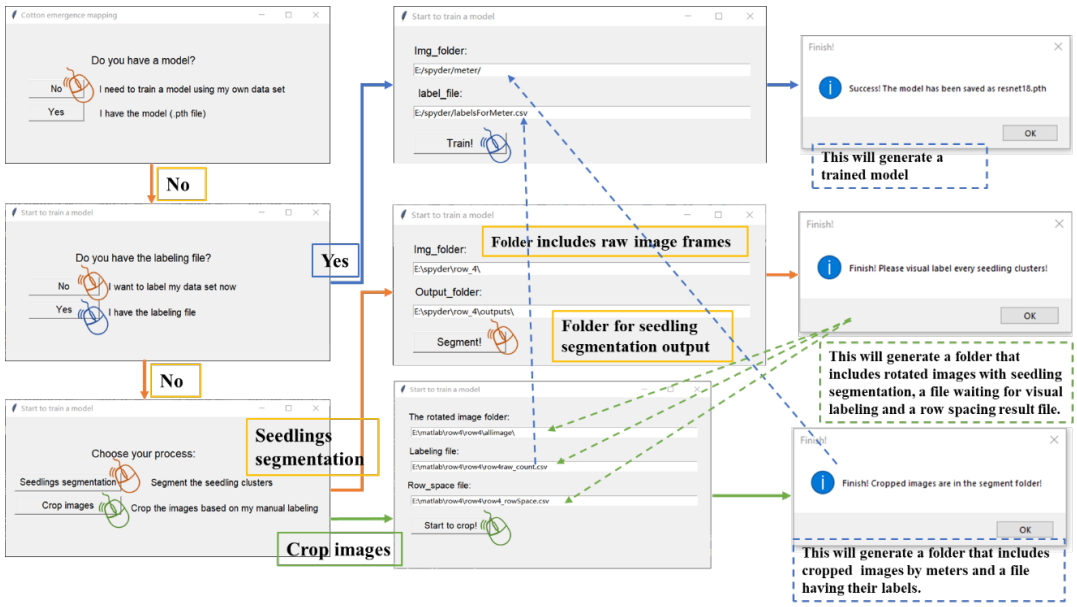

Figure 3.13: The process for training a customized model using the users' own data set. Different color of the mouse icons showed the different processing options as described in the text.

The process of mapping crop emergence is illustrated in Figure 3.14. The GPS assignment process (following the orange mouse icon in Figure 3.14) would guide users to assign GPS coordinates to each 1-meter of crop row. After geo-referencing all data of the whole field, the process would generate: 1) input images of *resnet18* cropped by a meter of each cotton row; 2) the related GPS file of each input image. Those input images and the GPS file would be used to map the cotton stand count and canopy size (the mapping process following the blue mouse icon in Figure 3.14).

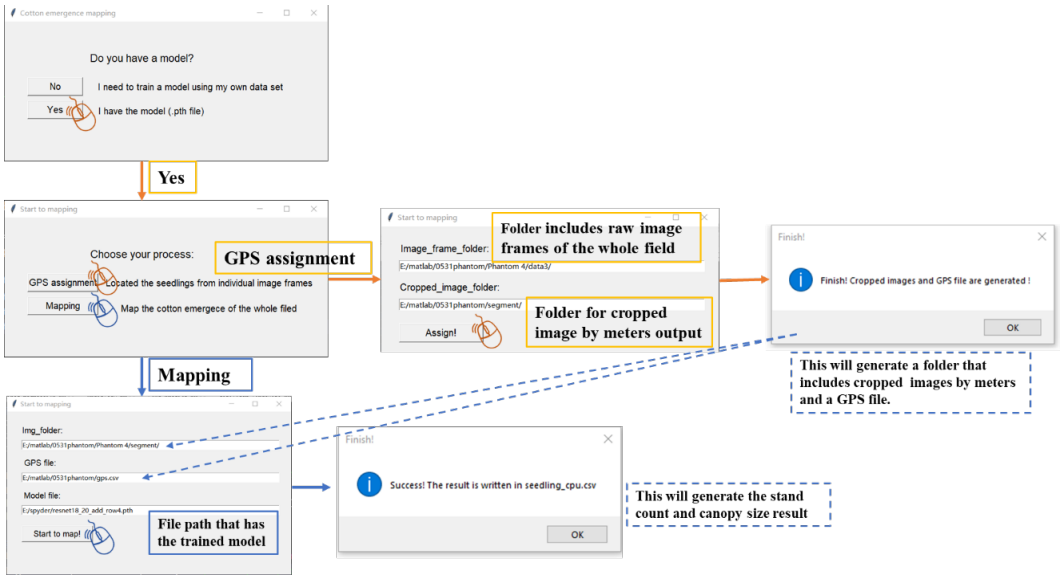

Figure 3.14: The process for mapping the cotton emergence of the whole field. Different color of the mouse icons showed the different process options as described in the text.

3.7 Conclusion

This study developed a method and related framework for real-time cotton stand count and canopy size mapping. A UAV system with a high-resolution RGB camera was used to take individual image frames. The cotton rows in each image frame were detected and the row angle was used for rotating each individual frame. The row spacing was used as a reference for dynamic GSD calibration of each image frame. Seedlings in every individual frame were located based on their position in image coordinates and the GSD. The located seedlings were used as the input to the deep learning model *resnet*18 for stand count and canopy size estimation. The results from the *resnet*18 model and the related location information were used to map cotton emergence. Results showed that the method had an overall error of MAPE = 4.4% and worked better than current traditional image segmentation methods. The framework could be used as a powerful tool for farmers and

researchers to explore the relationships between cotton emergence, soil conditions and weather conditions.

3.8 Future work

Comparing to image stitching and mosaic processing, this study processed individual image frames to map the emergence and had the problem of some same seedling that duplicate in two different image frames. For two image frames that included the same seedlings, those data would be mapped twice. Since this study mapped based on GPS of each meter of each crop row, the data may be mapped twice at the same position (due to the GPS error, they would be mapped twice at the close position). Later, average processing was needed to group those mapped data points in each meter together.

This study used MAE to evaluate the emergence prediction performance. It is worth trying other types of error measurement methods rather than MAE since the numbers of seedlings were small in each frame and the performance of the seedling prediction in each cluster of the frames needed to be evaluated.

For the current data set, we had weeds control in the field and few weeds appeared in the image data. This study did not use any methods to deal with weeds. However, for some fields with weeds, the stand count and canopy size prediction may have errors due to the difficulty of identification between weeds and cotton seedlings. Weed identification methods are needed for this case.

3.9 Literature cited

Abadi, M., Agarwal, A., Barham, P., Brevdo, E., Chen, Z., Citro, C., Corrado, G.S., Davis, A., Dean, J., Devin, M., 2016. Tensorflow: Large-scale machine learning on heterogeneous distributed systems. arXiv preprint arXiv:1603.04467.

Ayyachamy, S., Alex, V., Khened, M., Krishnamurthi, G., 2019. Medical image retrieval using Resnet-18, Medical Imaging 2019: Imaging Informatics for Healthcare, Research, and Applications. International Society for Optics and Photonics, p. 1095410.

Bargoti, S., Underwood, J., 2017. Deep fruit detection in orchards, 2017 IEEE International Conference on Robotics and Automation (ICRA). IEEE, pp. 3626-3633.

Bradski, G., 2000. The opencv library. Dr Dobb's J. Software Tools 25, 120-125.

Brown, M., Lowe, D.G., 2003. Recognising panoramas, ICCV, p. 1218.

Bugayevskiy, L.M., Snyder, J., 2013. Map projections: A reference manual. CRC Press.

Chawla, N.V., 2009. Data mining for imbalanced datasets: An overview, Data mining and knowledge discovery handbook. Springer, pp. 875-886.

Chen, R., Chu, T., Landivar, J.A., Yang, C., Maeda, M.M., 2018. Monitoring cotton (Gossypium hirsutum L.) germination using ultrahigh-resolution UAS images. Precision Agriculture 19, 161-177.

Chen, S.W., Shivakumar, S.S., Dcunha, S., Das, J., Okon, E., Qu, C., Taylor, C.J., Kumar, V., 2017. Counting apples and oranges with deep learning: A data-driven approach. IEEE Robotics and Automation Letters 2, 781-788.

Duda, R.O., Hart, P.E., 1972. Use of the Hough transformation to detect lines and curves in pictures. Communications of the ACM 15, 11-15.

Dumoulin, V., Visin, F., 2016. A guide to convolution arithmetic for deep learning. arXiv preprint arXiv:1603.07285.

Dyrmann, M., Jørgensen, R.N., Midtiby, H.S., 2017. RoboWeedSupport-Detection of weed locations in leaf occluded cereal crops using a fully convolutional neural network. Advances in Animal Biosciences 8, 842-847.

Dyrmann, M., Karstoft, H., Midtiby, H.S., 2016. Plant species classification using deep convolutional neural network. Biosystems Engineering 151, 72-80.

Egli, D., Rucker, M., 2012. Seed vigor and the uniformity of emergence of corn seedlings. Crop Science 52, 2774-2782.

Erhan, D., Manzagol, P.-A., Bengio, Y., Bengio, S., Vincent, P., 2009. The difficulty of training deep architectures and the effect of unsupervised pre-training, Artificial Intelligence and Statistics, pp. 153-160.

Feng, A., Sudduth, K., Vories, E., Zhou, J., 2019a. Evaluation of cotton stand count using UAV-based hyperspectral imagery, 2019 ASABE Annual International Meeting. American Society of Agricultural and Biological Engineers, p. 1.

Feng, A., Zhang, M., Sudduth, K.A., Vories, E.D., Zhou, J., 2019b. Cotton yield estimation from UAV-based plant height. Transactions of the ASABE 62, 393-404.

Feng, A., Zhou, J., Vories, E., Sudduth, K.A., 2020. Evaluation of cotton emergence using UAV-based narrow-band spectral imagery with customized image alignment and stitching algorithms. Remote Sensing 12, 1764.

Forcella, F., Arnold, R.L.B., Sanchez, R., Ghersa, C.M., 2000. Modeling seedling emergence. Field Crops Research 67, 123-139.

Fu, L., Majeed, Y., Zhang, X., Karkee, M., Zhang, Q., 2020. Faster R–CNN–based apple detection in dense-foliage fruiting-wall trees using RGB and depth features for robotic harvesting. Biosystems Engineering 197, 245-256.

Gao, F., Fu, L., Zhang, X., Majeed, Y., Li, R., Karkee, M., Zhang, Q., 2020. Multi-class fruit-on-plant detection for apple in SNAP system using Faster R-CNN. Computers and Electronics in Agriculture 176, 105634.

Geiger, A., Moosmann, F., Car, Ö., Schuster, B., 2012. Automatic camera and range sensor calibration using a single shot, 2012 IEEE International Conference on Robotics and Automation. IEEE, pp. 3936-3943.

Ghassemi-Golezani, K., Dalil, B., 2014. Effects of seed vigor on growth and grain yield of maize. Plant Breeding and Seed Science 70, 81-90.

Ghosal, S., Blystone, D., Singh, A.K., Ganapathysubramanian, B., Singh, A., Sarkar, S., 2018. An explainable deep machine vision framework for plant stress phenotyping. Proceedings of the National Academy of Sciences 115, 4613-4618.

Gnädinger, F., Schmidhalter, U., 2017. Digital counts of maize plants by unmanned aerial vehicles (UAVs). Remote Sensing 9, 544.

Goodell, P.B., Davis, R.M., Godfrey, L.D., Hutmacher, R.B., Roberts, P.A., Wright, S.D., M, B.V., Haviland, D.R., Munier, D.J., Natwick, E.T., 2015. UC IPM pest management guidelines cotton, Oakland, CA.

Goodfellow, I., Bengio, Y., Courville, A., Bengio, Y., 2016. Deep learning. MIT press Cambridge.

He, K., Zhang, X., Ren, S., Sun, J., 2015. Spatial pyramid pooling in deep convolutional networks for visual recognition. IEEE transactions on pattern analysis and machine intelligence 37, 1904-1916.

He, K., Zhang, X., Ren, S., Sun, J., 2016. Deep residual learning for image recognition, Proceedings of the IEEE conference on computer vision and pattern recognition, pp. 770-778.

Huang, G., Liu, Z., Van Der Maaten, L., Weinberger, K.Q., 2017. Densely connected convolutional networks, Proceedings of the IEEE conference on computer vision and pattern recognition, pp. 4700-4708.

Humphrey, E.J., Bello, J.P., LeCun, Y., 2012. Moving beyond feature design: Deep architectures and automatic feature learning in music informatics, ISMIR. Citeseer, pp. 403-408.

Iandola, F.N., Han, S., Moskewicz, M.W., Ashraf, K., Dally, W.J., Keutzer, K., 2016. SqueezeNet: AlexNet-level accuracy with 50x fewer parameters and< 0.5 MB model size. arXiv preprint arXiv:1602.07360.

Jin, X., Liu, S., Baret, F., Hemerlé, M., Comar, A., 2017. Estimates of plant density of wheat crops at emergence from very low altitude UAV imagery. Remote Sensing of Environment 198, 105-114.

Kamilaris, A., Prenafeta-Boldú, F.X., 2018. Deep learning in agriculture: A survey. Computers and electronics in agriculture 147, 70-90.

Koh, J.C., Hayden, M., Daetwyler, H., Kant, S., 2019. Estimation of crop plant density at early mixed growth stages using UAV imagery. Plant Methods 15, 64.

Krizhevsky, A., 2014. One weird trick for parallelizing convolutional neural networks. arXiv preprint arXiv:1404.5997.

Li, B., Xu, X., Han, J., Zhang, L., Bian, C., Jin, L., Liu, J., 2019. The estimation of crop emergence in potatoes by UAV RGB imagery. Plant methods 15, 15.

Lipan, F., Groza, A., 2010. Mining traffic patterns from public transportation GPS data, Proceedings of the 2010 IEEE 6th International Conference on Intelligent Computer Communication and Processing. IEEE, pp. 123-126.

Liu, S., Baret, F., Allard, D., Jin, X., Andrieu, B., Burger, P., Hemmerlé, M., Comar, A., 2017. A method to estimate plant density and plant spacing heterogeneity: application to wheat crops. Plant methods 13, 38.

McKinney, W., 2010. Data structures for statistical computing in python, Proceedings of the 9th Python in Science Conference. Austin, TX, pp. 51-56.

Mohanty, S.P., Hughes, D.P., Salathé, M., 2016. Using deep learning for image-based plant disease detection. Frontiers in plant science 7, 1419.

Monawar, T., Mahmud, S.B., Hira, A., 2017. Anti-theft vehicle tracking and regaining system with automatic police notifying using Haversine formula, 2017 4th International conference on Advances in Electrical Engineering (ICAEE). IEEE, pp. 775-779.

Nanni, L., Ghidoni, S., Brahnam, S., 2017. Handcrafted vs. non-handcrafted features for computer vision classification. Pattern Recognition 71, 158-172.

Nielsen, M.A., 2015. Neural networks and deep learning. Determination press San Francisco, CA, USA:.

Oliphant, T.E., 2006. A guide to NumPy. Trelgol Publishing USA.

Otsu, N., 1979. A threshold selection method from gray-level histograms. IEEE transactions on systems, man, and cybernetics 9, 62-66.

Pan, S.J., Yang, Q., 2009. A survey on transfer learning. IEEE Transactions on knowledge and data engineering 22, 1345-1359.

Paszke, A., Gross, S., Chintala, S., Chanan, G., Yang, E., DeVito, Z., Lin, Z., Desmaison, A., Antiga, L., Lerer, A., 2017. Automatic differentiation in pytorch.

Pedregosa, F., Varoquaux, G., Gramfort, A., Michel, V., Thirion, B., Grisel, O., Blondel, M., Prettenhofer, P., Weiss, R., Dubourg, V., 2011. Scikit-learn: Machine learning in Python. Journal of Machine Learning Research 12, 2825-2830.

Rahnemoonfar, M., Sheppard, C., 2017. Deep count: fruit counting based on deep simulated learning. Sensors 17, 905.

Ribera, J., Chen, Y., Boomsma, C., Delp, E., 2017. Counting plants using deep learning, 2017 IEEE Global Conference on Signal and Information Processing (GlobalSIP). IEEE, Montreal, QC, Canada, pp. 1344-1348.

Russakovsky, O., Deng, J., Su, H., Krause, J., Satheesh, S., Ma, S., Huang, Z., Karpathy, A., Khosla, A., Bernstein, M., 2015. Imagenet large scale visual recognition challenge. International Journal of Computer Vision 115, 211-252.

Sankaran, S., Khot, L.R., Carter, A.H., 2015. Field-based crop phenotyping: Multispectral aerial imaging for evaluation of winter wheat emergence and spring stand. Computers and Electronics in Agriculture 118, 372-379.

Sankaran, S., Quirós, J.J., Knowles, N.R., Knowles, L.O., 2017. High-resolution aerial imaging based estimation of crop emergence in potatoes. American Journal of Potato Research 94, 658-663.

Sansone, C., Isakeit, T., Lemon, R., Warrick, B., 2002. Texas cotton production: Emphasizing integrated pest management. Texas Cooperative Extension Service, the Texas A & M University System, Texas, USA.

Selvaraju, R.R., Cogswell, M., Das, A., Vedantam, R., Parikh, D., Batra, D., 2017. Grad-cam: Visual explanations from deep networks via gradient-based localization, Proceedings of the IEEE International Conference on Computer Vision, pp. 618-626.

Simonyan, K., Zisserman, A., 2014. Very deep convolutional networks for large-scale image recognition. arXiv preprint arXiv:1409.1556.

Snyder, J.P., 1987. Map projections--A working manual. US Government Printing Office.

Sudduth, K.A., Kitchen, N., Bollero, G., Bullock, D., Wiebold, W., 2003. Comparison of electromagnetic induction and direct sensing of soil electrical conductivity. Agronomy Journal 95, 472-482.

Supak, J., 1990. Making replant decisions, 1990 Beltwide cotton production conference. National Cotton Council of America, pp. 45-48.

Szegedy, C., Liu, W., Jia, Y., Sermanet, P., Reed, S., Anguelov, D., Erhan, D., Vanhoucke, V., Rabinovich, A., 2015. Going deeper with convolutions, Proceedings of the IEEE conference on computer vision and pattern recognition, pp. 1-9.

Varela, S., Dhodda, P.R., Hsu, W.H., Prasad, P., Assefa, Y., Peralta, N.R., Griffin, T., Sharda, A., Ferguson, A., Ciampitti, I.A., 2018. Early-season stand count

determination in corn via integration of imagery from unmanned aerial systems (UAS) and supervised learning techniques. Remote Sensing 10, 343.

Wang, Z., Yang, J., 2017. Diabetic retinopathy detection via deep convolutional networks for discriminative localization and visual explanation. arXiv preprint arXiv:1703.10757.

Wiles, L.J., Schweizer, E.E., 1999. The cost of counting and identifying weed seeds and seedlings. Weed Science 47, 667-673.

Zeiler, M.D., Fergus, R., 2014. Visualizing and understanding convolutional networks, European conference on computer vision. Springer, pp. 818-833.

Zhang, Z., 2000. A flexible new technique for camera calibration. IEEE Transactions on pattern analysis and machine intelligence 22.

Zhao, B., Zhang, J., Yang, C., Zhou, G., Ding, Y., Shi, Y., Zhang, D., Xie, J., Liao, Q., 2018. Rapeseed seedling stand counting and seeding performance evaluation at two early growth stages based on unmanned aerial vehicle imagery. Frontiers in Plant Science 9.

Chapter 4. SOIL AND ELEVATION EFFECTS ON COTTON EMERGENCE

4.1 Abstract

Crop emergence is an important agronomic factor for farmers and researchers to explore crop development in the early growth stage, as well as explore the relationship between emergence, subsequent growth and environment (such as soil texture and field elevation). A method and related framework were developed for near real-time emergence mapping using Unmanned aerial vehicle (UAV)-based images in our previous study. However, analysis of the emergence data, soil and field elevation, as well as the UAV image data collected in the later growth stages needed ways to align those data from different sensor systems together. The GPS error of the previous study depended on the UAV GPS system, which was 1.72 ±1.37 m comparing with the ground RTK measurement. To improve the alignment accuracy, the goal of this study is to improve the GPS accuracy of cotton emergence mapping and then evaluate the feasibility of a UAV-based imaging system in quantifying the relationship between emergence, subsequent growth and environment. A crop row alignment method was developed based on feature detection and matching, and then the geo-referenced crop emergence data were registered with its subsequent growth data (UAV-based vegetation indices) in July as well as soil and field elevation data. Pearson correlation, ANOVA and machine learning model XGBoost were used to analyze the relationships between stand count and canopy size with field elevation, soil, as well as with the UAV-based vegetation indices in the next growth stages in July. Results showed that the GPS error comparing with the ground RTK was 0.17 ± 0.13 m,

which was higher accuracy than our previous methods. Emergence, $EC_{a\text{-}sh}$, $EC_{a\text{-}dp}$ and clay10-clay30 were ranked the first six important features to cotton emergence. The seedling size had about 0.4-0.5 Pearson correlation coefficients with the image features collected in July but about 0.3 with the final yield, which showed the low correlation between emergence and its later growth.

Keyword: emergence evaluation, soil texture, field elevation, row geo-reference; real-time processing

4.2 Introduction

Crop emergence is an important agronomic factor for crop development assessment and field management in the early stages, which can be evaluated using plant population, stand count, uniformity and seedling size (Sansone et al., 2002; Supak, 1990). Accurate and timely assessment of crop stand count and seedling size at the emergence stage may help farmers make important field management decisions (e.g., replanting) to reduce production loss (Goodell et al., 2015) as well as explore the environmental effects on the crop emergence and development (Anda and Pinter, 1994; Benvenuti, 2003; Domenech and Vila, 2008; Forcella et al., 2000; Ghassemi-Golezani and Dalil, 2014; Valdés-Rodríguez et al., 2013). Acquisition of high-resolution site-specific crop emergence information is the baseline for the above decisions and studies. Conventionally, crop emergence is assessed through visual observation (manual stand counts and seedling size evaluation) in a small number of sampling sites (Wiles and Schweizer, 1999), which is time-consuming, labor-intensive, and not suited to cover a large production field.

In recent years, unmanned aerial vehicle (UAV)-based imaging technology has been tested as a high-throughput tool for crop emergence assessment in various crops as

summarized by Feng et al. (2020b). Some examples include the assessment of wheat density (Jin et al., 2017; Sankaran et al., 2015), cotton uniformity (Feng et al., 2019), and stand count in cotton (Chen et al., 2018; Feng et al., 2019), corn (Varela et al., 2018), potato (Sankaran et al., 2017) and rapeseed (Zhao et al., 2018). Those published studies used similar approaches to process UAV imagery data, i.e., using commercial UAV image processing software, such as Agisoft PhotoScan (Agisoft LLC, St. Petersburg, Russia) and Pix4D (Pix4D S.A., Lausanne, Switzerland), to generate orthomosaic images before further processing. The procedure of generating orthomosaic images included image feature detection, matching, alignment and blending based on mosaic blending models as described by Brown and Lowe (2003), takes a very long time (days or weeks) and requires extensive computational resources. However, emergence evaluation is a time-sensitive analysis and the challenge in timely processing of imagery data becomes one of the most critical barriers for adopting UAV imagery in applications of crop emergence assessment (Forcella et al., 2000; Supak, 1990). In our previous study (Feng et al., 2020a), an efficient imagery data processing and analysis framework for timely evaluation of cotton emergence using UAV-based RGB imagery and deep learning technology was developed. It was different from previously published studies in the approach of directly processing individual image frames rather than developing orthomosaic images to reduce the processing time.

With the above methods and framework, timely emergence mapping and accurate emergence data could be obtained. Exploring the relationship between crop emergence, its subsequent growth and the environment are the next important topic (Feng et al., 2020a, b). Soil texture correlates with soil water holding capacity and is one of the most important

factors that affect crop emergence (Anda and Pinter, 1994; Benvenuti, 2003; Domenech and Vila, 2008; Valdés-Rodríguez et al., 2013). The study of Stewart (2020) showed that topography and slope had the potential effects on soil erosion, water runoff and field microclimate, which influenced corn emergence. Some studies (Carter and Nafziger, 1990; Nafziger et al., 1991) showed that uneven crop emergence resulting in plant competition in the later growth stages decreased crop yield. Although there have been studies on the relationships between emergence, subsequent growth, yield and environment many years ago, the emerging sensing technologies (i.e. soil EC sensors, field elevation sensors and UAV imaging sensors) in recent years can provide more reliable and large amounts of data for these studies to draw more credible conclusions. Analysis of the emergence data, soil and field elevation, as well as crop growth in the later growth stages, needed ways to alignment those data from different sensor systems (i.e. different UAV systems used in the emergence growing stage and in the later growth stages, soil EC sensor systems, field elevation measurement system and yield monitor system) together. The GPS error of the mapping methods used in our previous study (Feng et al., 2020a) depended on the specific UAV GPS system used, which was 1.72 ±1.37 m comparing with the ground RTK measurement. Therefore, to improve the crop row alignment with the plants in later growth stages and the ECa-based soil texture as well as the field elevation data, improving alignment algorithm is needed to add to the previous study to conduct the environment effects on emergence as well as explore the relationships between emergence with the later grow stages and yield. The goal of this study is to improve the GPS accuracy of cotton emergence mapping and then evaluate the feasibility of UAV-based imaging system in quantifying the relationship between emergence, subsequent growth and environment. The

specific objectives are: 1) increasing the accuracy of emergence maps to register with its subsequent growth data as well as soil and elevation data; and 2) using the developed mapping methods to explore the soil and field elevation effects on emergence, as well as the relationships between the emergence with its subsequent growth and yield.

4.3 Emergence row register from individual RGB frame

Feature detection and matching

The crop row alignment algorithm was based on previous customized image alignment and stitching algorithms described in Feng et al. (2020b). Feature detection and matching were conducted to the rotated images based on the SHT crop row identification. Image features were detected using the method of Speeded-Up Robust Features (SURF), a 128-dimension (8 orientation bins for each of the 4 × 4 location bins) local feature detector and descriptor developed in (Bay et al., 2008). As a scale-invariant feature, SURF used image pyramids and different sized box filters to find points of interest at different scale-spaces (Lowe, 2004). The scale-space of SURF was divided into octaves and each octave was subdivided into a constant number of scale levels. The number of pyramid octaves and octave layers were both set to 3 in this study. After feature detection, the k-nearest neighbors (KNN) algorithm was used to match the most similar feature pairs in two successive raw images. The KNN calculated all of the Euclidean distances of features with each other to find the closest K matches. In this study, K was set to two ($K = 2$); therefore, the KNN algorithm returned the two closest key points for each key point to be matched.

Removal of false matches

False matches were those pixels that had the shortest Euclidean distance but were different objects in the successive images. To detect and remove false matches, a distance ratio test was conducted to compare the Euclidean distance of the closest key point to that of the second-closest key point identified by KNN (Lowe, 2004). It was assumed that the first closest key point came from the same object as the key point to be matched, while the second closest key point came from another object. Distance ratio tests checked the similarity of the two nearest matches to select the matches with high similarity in successive images that were not reliable and should be removed. All matches whose distance ratio test was greater than 0.65 were removed in this study.

The images were collected on a calm day, and the UAV was parallel flying with the ground with minimum variations in roll and pitch, but small adjustments in yaw angle due to navigation error (flight heading, speed and height). Therefore, the geometric transformations for matching any two successive images only included the operations of translation, scale and rotation. Considering the rotation and scale factor of two successive images were small in this study, in the case where scale and rotation were small enough to be negligible, the matching lines of the correct matches should have similar slopes and lengths. The slope and length of the matching lines were calculated using Eq 4.1 and 4.2:

$$slope = \frac{y_2 - y_1}{x_2 - x_1} \tag{4.1}$$

$$length = \sqrt{(x_2 - x_1)^2 + (y_2 - y_1)^2} \tag{4.2}$$

where, (x_1, y_1) and (x_2, y_2) are the coordinates of a key point and its matching point in two successive images. The matches were considered to be false matches if the slopes and lengths of the matching lines had a large difference from other matches.

Another way to determine false matches was to calculate the ratio of the slope and the length of one matching line to the mean value of all matching lines in two successive images. The ratios of the slope and length of the correct matches would be close to 1. The thresholds for false matches were set as lower than 0.9 and greater than 1.1. Both the methods discussed above were used in this study to remove false matches. Figure 4.1 shows an example of feature detection and matching in two successive frames after all the false matches were removed.

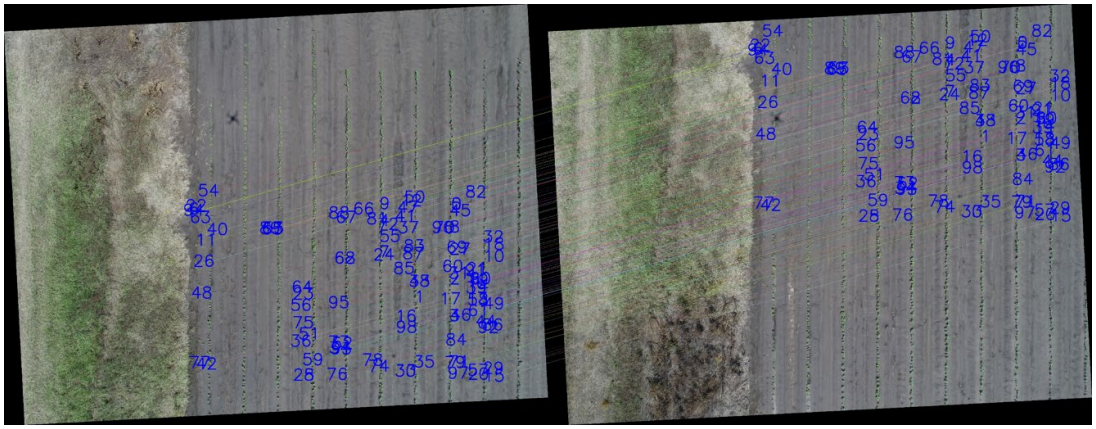

Figure 4.1: Feature detection and matching in two example frames. The blue numbers in each frame are the detected image features and the same number IDs with a color line connect two matched image features.

Calculation of the geometric transformation matrix

Once the correct matches were identified, transformation matrices of each pair of two successive images were calculated. As mentioned earlier, the scale factor of two successive images was small in this study and the image frames were rotated to obtain cotton rows aligned with the vertical axis of the images, therefore, only translation was considered in this study. The transform matrix *M* is shown as Eq 4.3 (Szeliski, 2007):

$$M = \begin{bmatrix} t_x \\ t_y \end{bmatrix} \quad (4.3)$$

where, t_x and t_y are the distance in pixels of translation in the horizontal and vertical directions. Assuming a pixel value of an image coordinate *I(x, y)* was to be transformed into its previous image coordinate *I'(x',y')*, Eq 4.4 shows the transformation of these two images based on the transform matrix *M*:

$$\begin{bmatrix} x' \\ y' \end{bmatrix} = M \cdot \begin{bmatrix} x \\ y \\ 1 \end{bmatrix} \quad (4.4)$$

where, (x, y) and (x', y') are image coordinates of image *I(x, y)* and *I'(x',y')*.

Crop rows alignment based on the geometric transformation matrix

After conducting the SHL to the original image frames, the images rotated and each crop row positions in the rotated images could be obtained. There were 152 crop rows in total and the crop row numbers of the first image frame were identified manually. The t_x in the geometric transformation matrix *M* controls the distance in pixels of translation in the horizontal directions. When each crop rows in the second image frame translated t_x pixels, they would match with the positions of each crop rows in the first image and would be assigned row numbers corresponding with the row numbers in the first image. New crop rows that appeared on the right side of the second image frame would be assigned a successive number of the last crop row in the first image frame. This process would continue in every two consecutive image frames until all pictures have been assigned the corresponding crop row numbers. Figure 4.2 shows the crop rows alignment of the first two image frames.

Figure 4.2: Crop rows alignment. There were 10 cotton rows identified manually in the first image frame. The numbers of 9 cotton rows identified by the SHL in the second image frame were aligned with the first image frame based on the geometric transformation matrix *M*.

Image frame positions within each entire crop row

The t_y in the geometric transformation matrix *M* controls the distance in pixels of translation in the vertical directions. When the UAV flew through north to south then south to north, the regions included in each image frame moved from the beginning to the end then from the end to the beginning of the entire crop rows. A specific image frame moved t_y pixels from its previous image frame in the vertical directions. However, uncontrol factors such as wind and low batteries during the flight made the UAV flew unstably and resulted in different GSD in each image frame and the pixels of translation in the vertical directions cannot represent the true translation in the meters of the entire crop rows in the

vertical directions. Since the GSD of each image frame was calculated based on the fixed row spacing in Chapter 3.1, translation in meters in the vertical directions can be calculated by Eq 4.5. The first image frame at the beginning of the data collection (the beginning of the first crop rows) was used as the reference of zero of the entire field, and positions of other image frames were calculated as the meters of distance between them and these zero references in the vertical directions.

$$t_{y\_meter} = \frac{t_y}{GSD} \qquad (4.5)$$

where t_{y_meter} is the translation in meters in the vertical directions, t_y is the pixels of translation in the vertical directions and GSD is the ground sample distance.

Emergence mapping based on the image alignment

For each 1-m seedling segment in Figure 3.3b, the algorithm would first recognize its crop row numbers based on the crop row assignment results described above. The t_{y_meter} described the translation in meters in the vertical directions for the geometric center of each image frame. To calculate the translation in meters of each 1-m seedling segment in Figure 3.3b between them and the zero reference in the vertical directions, the distance in meters between the 1-m seedling segments and the geometric center of the image frames were needed to calculate. The translation in meters between each 1-m seedling segment and the zero reference in the vertical directions was the result of t_{y_meter} added or subtracted the distance in meters between the 1-m seedling segments and the geometric center of the image frames. If some 1-m seedling segments from different image frames were geometrically close (less than 1 meter distance), the average of their predicted stand count and their predicted canopy size would be used when mapped the emergence of the whole field.

4.4 Limitation of the crop row alignment algorithm

Low overlapping of the image frames

The success of feature detection and matching relied on the overlapping of every two successive frames. If the two successive frames had a very small overlapping rate in the forward direction, the feature detection and matching would fail. Figure 4.3 shows two alignment examples with one about 30% and the other one less than 5% overlapping in the forward direction. Although a 60% overlapping in both forward and sideward directions were set for the UAV flight plan, uncontrol factors such as wind and low batteries during the flight made the UAV flew unstably and resulted in low overlapping images. There are 2200 images in total and 11 images were found out unsuccessful alignment due to the low overlapping rate. There were two solutions for those 11 images to align correctly: 1) used the side overlapping images instead. The sideward overlapping images could be found based on the closest of the image GPS in the nearby UAV flight path. Figure 4.4 shows an example of the successfully sideward overlapping images alignment; 2) if both the forward and sideward overlapping rate were less than 5%, this image frame cannot be aligned successfully using the provided algorithm. Manually identified the crop row numbers of this image frame with crop row numbers in its nearby image frames were needed to assign the correct crop row numbers. There were 3 images out of those 11 images needed to assign the correct crop row numbers manually.

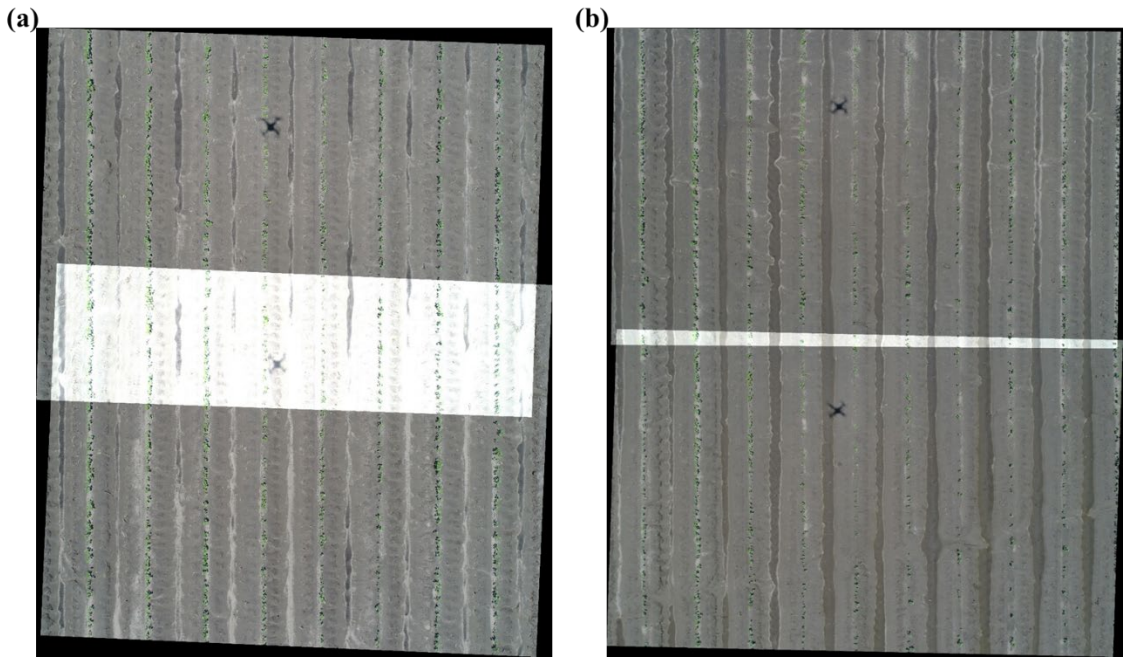

Figure 4.3: Two examples of the image frame alignment: (a) successfully aligned with about 30% overlapping in the forward direction between those two successive frames; (b) less than 5% overlap in the forward direction between these two successive frames and cannot be aligned successfully with the algorithm. The alignment result in (b) was the result of manual alignment.

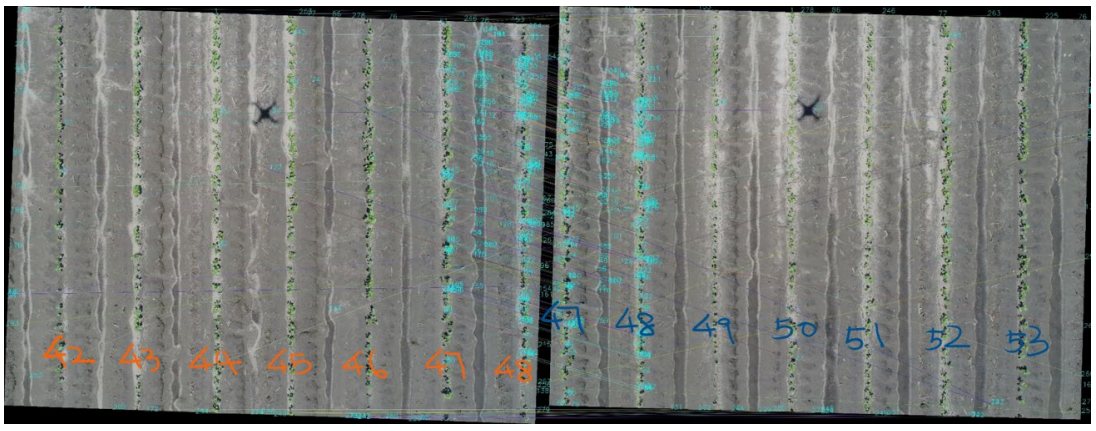

Figure 4.4: Image frames aligned successfully using sideward overlapping images. This is one of the solutions for the 11 image frames that cannot be successfully aligned due to

the low forward overlapping. The color numbers in each image were the crop row numbers assigned to each image.

Incorrect image alignment when changing UAV batteries

When the UAV batteries were about to use up, the UAV usually cannot have a well-control of the stable flying, especially for the flight height controlling, which resulted in a low UAV flight height, smaller numbers of crop rows including in one image and larger GSD of the image frames. We considered scale factor of two successive images were small and only translation was considered in the geometric transformation matrix *M*. When the UAV batteries were used up and changed to new batteries, the UAV would become well-control of the stable flying again and had a different flight height with the last image frame that using the previous about to use up batteries, which resulted in a larger scale factor between these two image frames and unsuccessful crop rows alignment. We used four sets of batteries in total for the entire field data collection, and the crop row numbers of the first image frame in each set of batteries needed to be identified manually. For crop row numbers of the first image collected with the first set of the UAV batteries were easy to assign the row numbers, as shown in Figure 4.2. For the crop row numbers of the first image collected with the second to the fourth set of the UAV batteries, the crop row numbers can be assigned based on the feature detection and matching results, as shown in Figure 4.5.

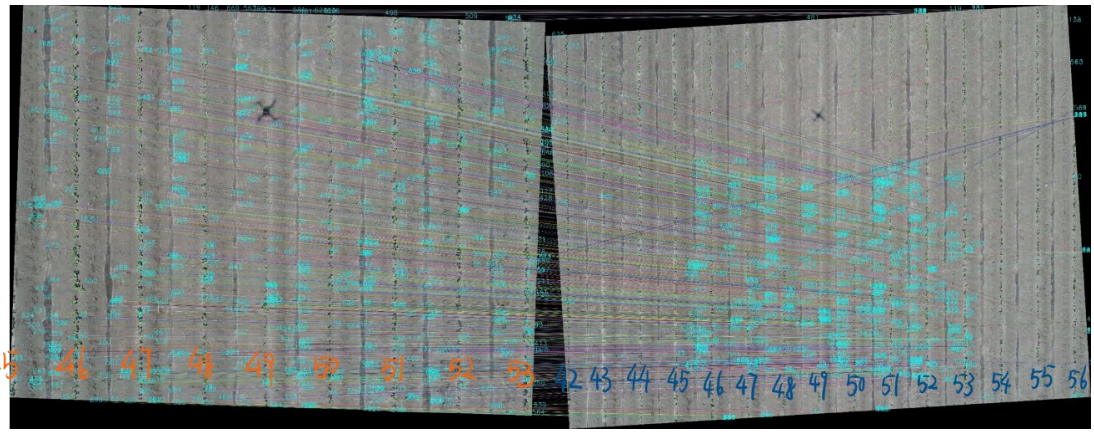

Figure 4.5: Crop row alignment of image frames collected in the UAV batteries changed based on the feature detection and matching results. The color numbers in each image were the crop row numbers assigned to each image.

4.5 GPS accuracy

GPS accuracy of the row alignment mapping method was measured between ground RTK measurement and image measurement, as shown in Figure 4.6. Ground RTK measurement measured the distance in meter between each two GPS coordinates of the 28 GRPs, while image measurement measured the distance in meter between every two ground stakes in the 28 GRPs in images. The row spacing determination affected the accuracy of the ground distance calculation between two subsequent image frames within a UAV flight path based on the Eq. 4.5. The row spacing was set as 0.97 m of the seed planter, however, in Chapter 3, the row spacing was 0.99 m based on image measurement in the GRPs. We tested the GPS accuracy using 0.97, 0.975, 0.98, 0.985, 0.99 m as the row spacing of the Eq. 4.5 respectively, and 0.98 m using as the row spacing had the lowest GPS accuracy, which was 0.17 ± 0.13 m. This was higher accuracy than the methods used in Chapter 3, which was 1.72 ±1.37 m.

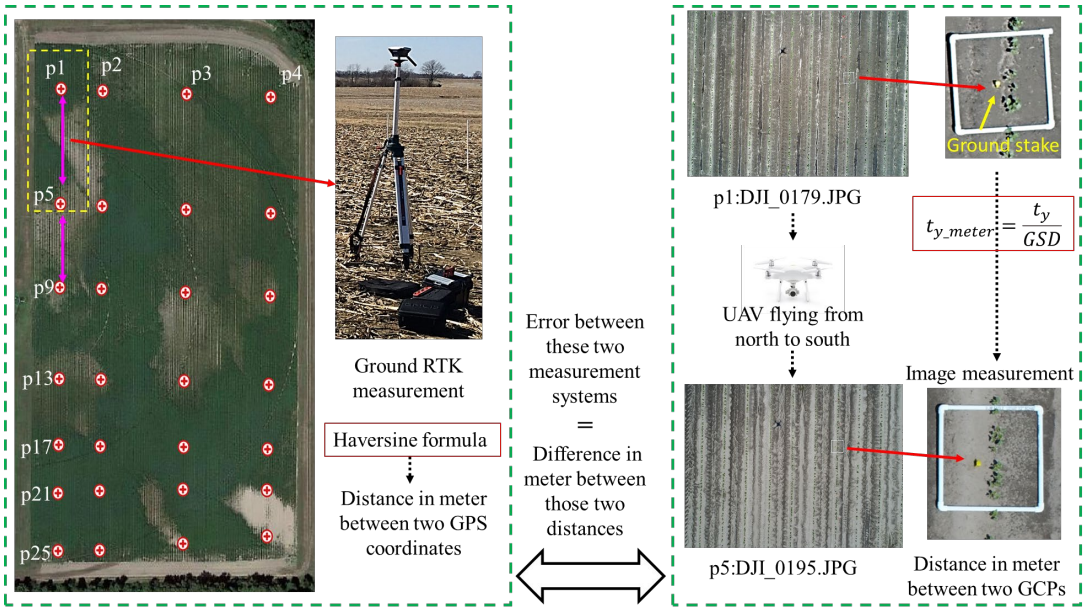

Figure 4.6: GPS error measurement between two different kinds of systems: ground RTK measurement and image measurement.

4.6 Factors affected the stand count and canopy size

The emergence maps

There were 152 crop rows in total and each crop row was about 315 m lengths, therefore a stand count map (seedlings meter^{-1}) and a canopy size map (cm^2 seedling^{-1}) with a dimension of 152 crop row × 315 m length of each crop row could be generated, shown as Figure 4.7a-b. Then, those maps were downsampled to a dimension of 38 × 63 maps to match with the lower special dimension data such as soil EC_a, elevation, yield and vegetation indices maps in July. Each data point in the 38 × 63 maps equates to a 4 m × 5 m area.

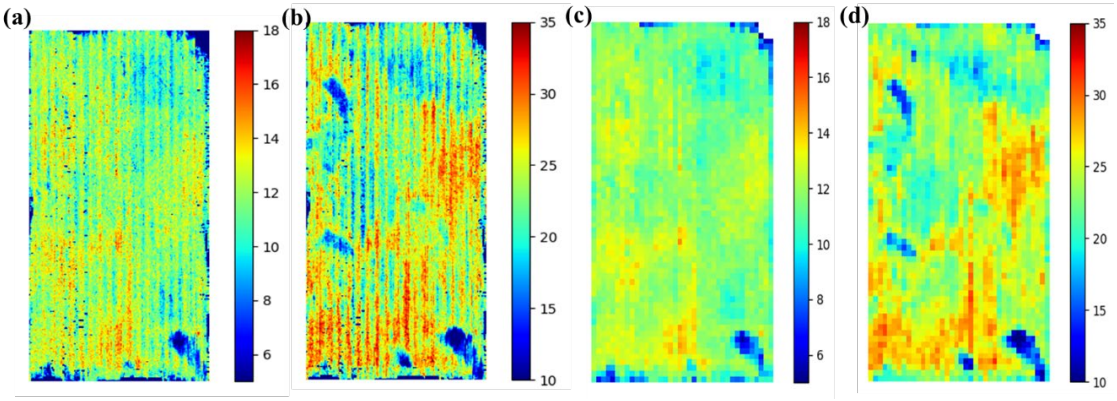

Figure 4.7: Emergence maps of (a) stand count (seedlings meter^{-1}) and (b) canopy size (cm^2 seedling^{-1}) with a dimension of 152 crop row × 315 m length of each crop row. (c) and (d) are the stand count (seedlings meter^{-1}) and (b) canopy size (cm^2 seedling^{-1}) that downsampled from (a) and (b). Their dimension was 38 × 63, and each data point equates to a 4 m × 5 m area.

Soil and elevation effects on the stand count and canopy size

Some studies had shown that clay content had a negative relationship while sand content had a positive relationship with crop emergence rate (Anda and Pinter, 1994; Benvenuti, 2003; Domenech and Vila, 2008; Valdés-Rodríguez et al., 2013). In this study, the EC_a-based clay% were split into five groups evenly: low clay% (0, 5.95], medium_low clay% (5.95, 8.69], medium clay% (8.69, 10.58], medium_high clay% (10.58, 12.72], and high clay% (12.72, 28.39]. Analysis of variance (ANOVA) was conducted to compare differences in the means of stand count and canopy size for different clay% groups using Tukey's Honest method at a 0.05 level of significance, as shown in Figure 4.8a-b. Kernel density estimation (KDE) was used to model the probability distribution of stand count and canopy size in the five clay% groups using Gaussian kernels, as shown in Figure 4.8c-d. The results show that a majority of stand count of all the clay% groups were in the range

of 10 to 14, and the low and medium-low clay% groups had a slightly higher stand count. The planting rate was 11 seedlings meter^{-1} but with some planter-calibration errors. For the canopy size, the low clay% group had the lowest average canopy size and there was higher probability distribution of less than 20 cm^2 seedling^{-1} than other clay% groups. Except for the low clay% group, the average canopy size decreases from the medium_low to the high clay% groups, which shows a negative relationship between canopy size and clay%.

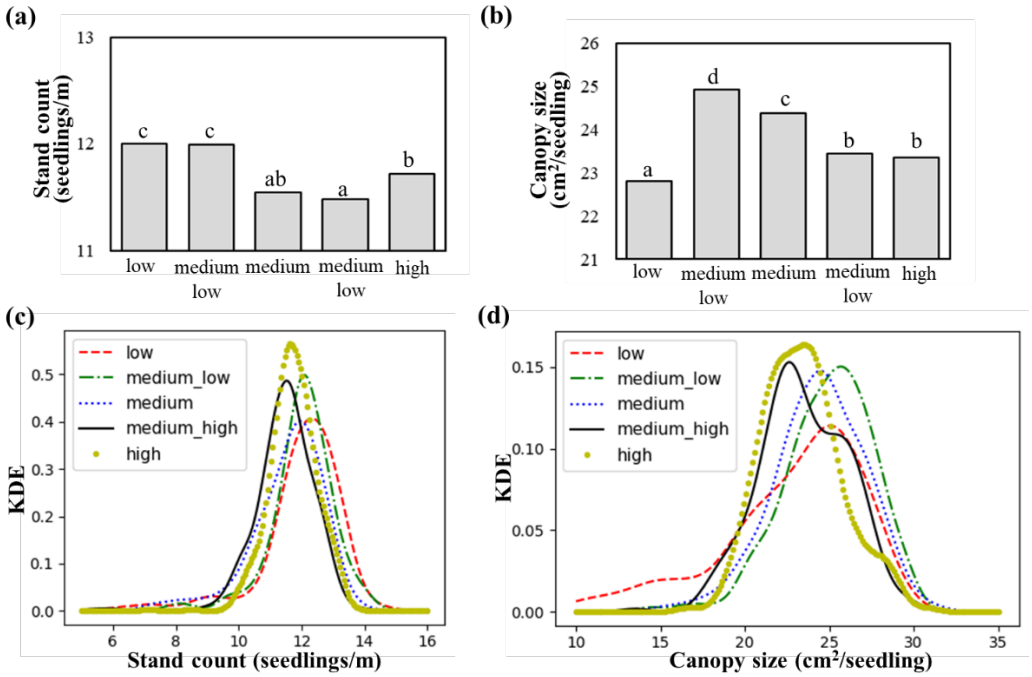

Figure 4.8: Relationships between emergence (stand count and seedling size) and EC_a-based soil clay%. Low clay%: (0, 5.95], medium_low clay%: (5.95, 8.69], medium clay%: (8.69, 10.58], medium_high clay%: (10.58, 12.72], and high clay%: (12.72, 28.39]. Each clay% group had the same numbers of clay% data points. (a) Mean stand count and (b) seedling size difference of five clay% content groups. Different lower-case letters indicate a significant difference at the 5% level of Tukey's honest significant difference test. The KDE of the (c) stand count and (d) seedling size in the five clay% content groups.

A scalable tree boosting model XGBoost (Chen and Guestrin, 2016) was used to explore how much the soil features contributed to the stand count and canopy size variation. The XGBoost model included hundreds of decision trees trained by the inputs of soil features (included the $EC_{a\text{-}sh}$, $EC_{a\text{-}dp}$, clay10-clay70, WP, FC, TAW and field elevation; soil data processing details were written in Chapter 5.4) and used the stand count and canopy size as the prediction with an additive strategy (build trees one following another, with the current one trying to predict what the previous trees did not predict well). Each decision tree was trained using 70% of the training data and built its branches (decision boundary) based on the residual of the previously built trees. The procedure of building tree branches of each decision tree was the procedure of choosing features from inputs for prediction, and a certain proportion of features instead of all the inputs would be used to build each tree to avoid overfitting. Therefore, the XGBoost model itself has the ability for feature selection and to address collinearity problems (Hayes et al., 2015). The overall dataset was split into 85% training set and 15% test set, and the coefficient of determination (R^2) in the test set was used to quantify how well the model explained the data. The R^2=0.43 and mean absolute percentage error (MAPE)=5.97% were obtained for the stand count prediction of the test set, while R^2=0.43 and MAPE=8.51% were obtained for the canopy size prediction of the test set.

Shapley values (Shapley, 1953) were used to explain how much each of the soil input feature values contributed to the stand count and canopy size prediction. We computed the predicted stand count and canopy size with a difference of each soil feature value and take the predicted difference to get the marginal contribution. The Shapley value is the (weighted) average of marginal contributions (Molnar, 2020). When the Shapley

value was zero for a specific soil feature, it means that this feature does not have any contribution to the stand count and canopy size prediction, while if the Shapley value was a negative (or positive) value for a specific soil feature, it means this feature had a negative (or positive) contribution to the prediction. Soil features with large absolute Shapley values are important to the stand count and canopy size prediction (Molnar, 2020). SHapley Additive exPlanations (SHAP) tool (Lundberg et al., 2020) was used to calculate the Shapley value in this study. Figure 4.9 shows the Shapley value of the soil features in stand count and canopy size prediction. Elevation ranks at the first important to both the stand count and canopy size prediction, and the elevation shows a positive relationship with both of them. The clay10 to clay70 show decrease important to the canopy size prediction, while clay10 and clay30 show more important to the stand count than the clay content in other depth layers. WP, FC and TAW did not show too much important to both the stand count and canopy size prediction. Elevation, $EC_{a\text{-}sh}$, $EC_{a\text{-}dp}$ and clay10-clay30 were ranked the first six important to both the stand count and canopy size prediction.

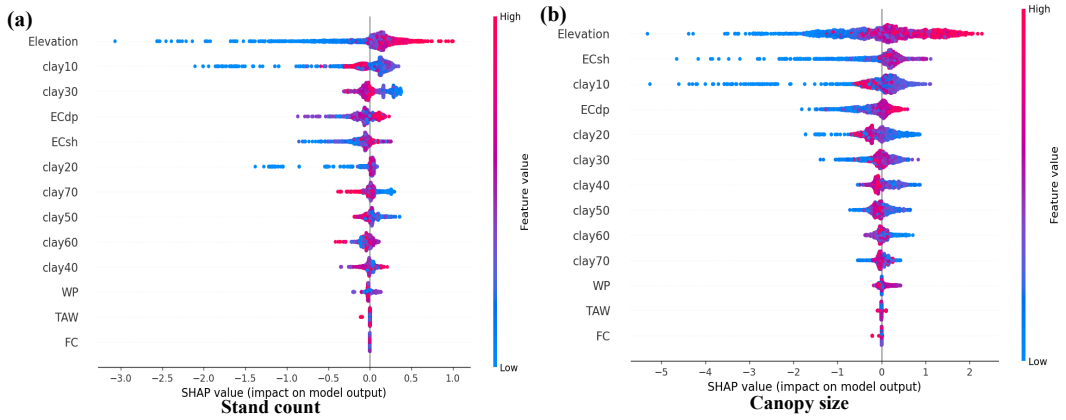

Figure 4.9: Shapley value of the soil features in (a) stand count and (b) canopy size prediction.

The SHAP tool (Lundberg et al., 2020) includes a function named SHAP dependence plot, which can help to explore the details of how Shapley values changes with specific soil feature value changes, as shown in Figure 4.10 and Figure 4.11. The overall elevation difference of the field is 1.5 m and increases from the north side to the south side. The prediction of the stand count decreases 1-2 seedlings and canopy size decreased 1-5 cm^2 $seedlings^{-1}$ compared to the overall average seedling numbers and canopy size if the elevation is lower than 87.2 m. For clay10 and clay20, stand count and canopy size prediction decreases largely when the clay content is less than 6%, and the highest stand count and canopy size prediction appear in the range of 6%-8%. When the clay content is larger than 8%, stand count and canopy size prediction decrease slightly. The clay30 has a similar trend with the clay10 and clay20 for the canopy size prediction, but stand count had a decreasing trend when clay30 increases. $EC_{a\text{-}sh}$ had an increasing trend for the stand count prediction in the range of 0-15, while $EC_{a\text{-}dp}$ had an increasing trend for the canopy size prediction in the range of 0-15.

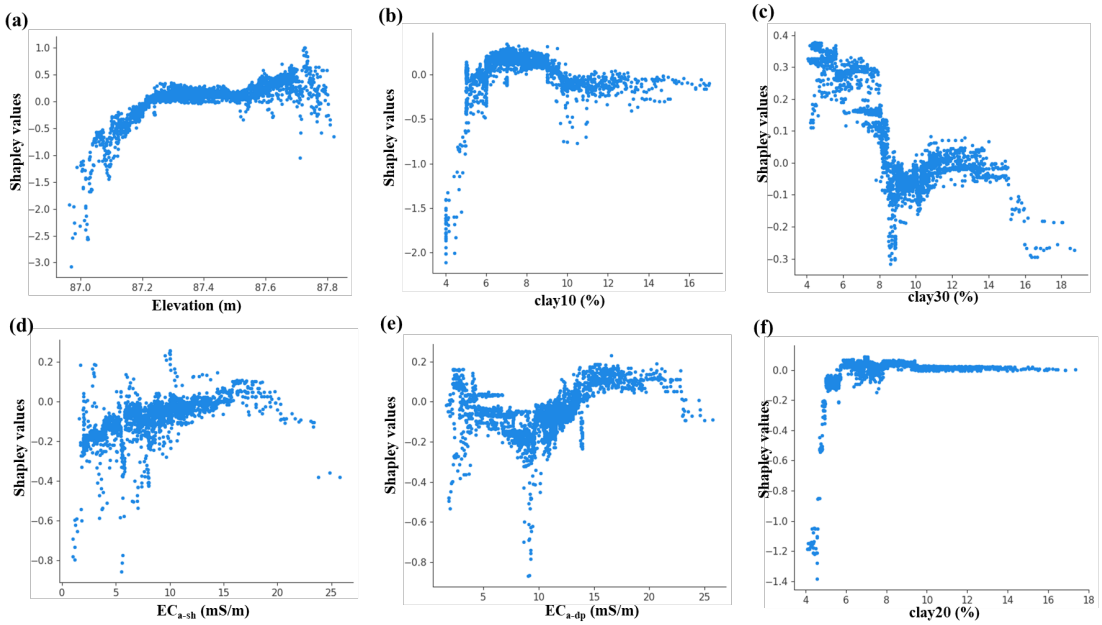

Figure 4.10: Shapley value changes corresponding to the top six important soil feature values changes for stand count prediction.

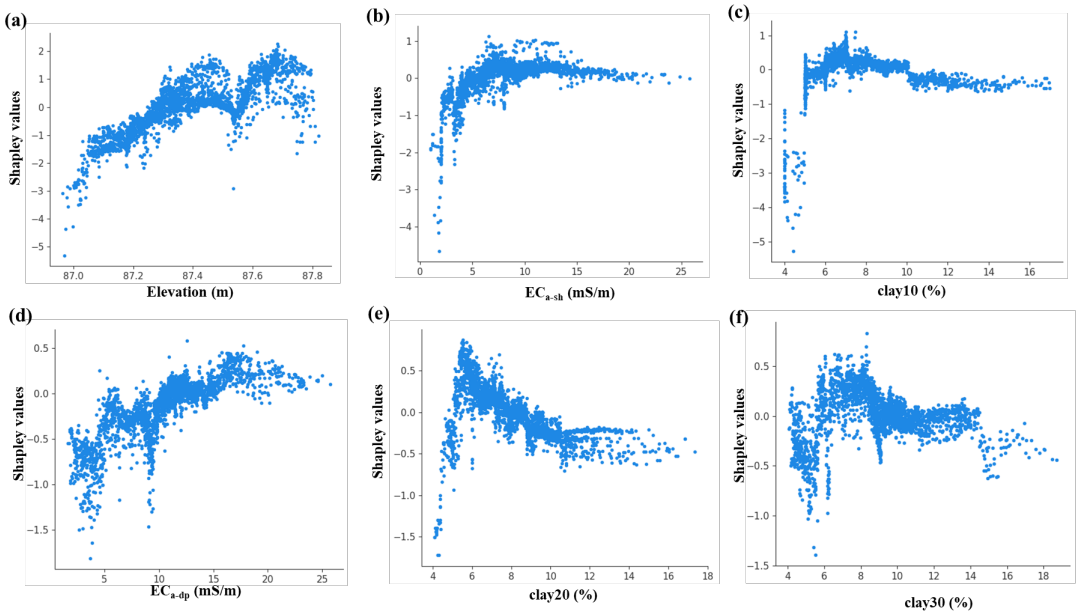

Figure 4.11: Shapley value changes corresponding to the top six important soil feature values changes for canopy size prediction.

Emergence and the crops' subsequent development

The stand count and seedling size data in the emergence were conducted the Pearson correlation with the NDVI, canopy size, GNDVI, NDRE, a* in the image collected on July 12, 2019 (image processing details were written in Chapter 5.3) and the final yield in 2019, as shown in Table 4.1. Canopy size had higher correlation coefficients with the image features and yield than the stand count. The coefficients between seedling size with NDVI, canopy size, GNDVI and NDRE were 0.4-0.5. The coefficients between stand count with image features and yield were less than 0.4. Both the stand count and seedling size had low correlation coefficients with the final yield (0.3 and 0.35).

Table 4.1: Pearson correlation coefficients between emergence (stand count and seedling size) and image features collected on July 12, 2019 and the final yield in 2019.

	NDVI	Canopy size	GNDVI	NDRE	a*	Yield
Stand count	0.25	0.33	0.26	0.18	0.02	0.3
Seedling size	0.42	0.5	0.4	0.41	0.16	0.35

4.7 Conclusion

This Chapter improved the mapping GPS accuracy for real-time cotton stand count and canopy size mapping. A UAV system with a high-resolution RGB camera was used to take individual image frames. A crop row alignment method on each individual frame was developed. The results showed that the GPS accuracy of the improved method of emergence mapping was 0.17 ± 0.13 m. Field elevation, $EC_{a\text{-}sh}$, $EC_{a\text{-}dp}$ and clay10-clay30 were ranked the first six important features to both the stand count and canopy size prediction. The seedling canopy had about 0.4-0.5 Pearson correlation coefficients with the image features collected in July but a low correlation coefficient with the final yield. The methods developed could be used as a powerful tool for farmers and researchers to explore the relationships between cotton emergence, soil conditions and weather conditions.

4.8 Future work

Compared to the emergence mapping methods in Chapter 3, the row alignment mapping method in this Chapter had higher GPS accuracy. However, the image processing time increased a lot (about 17 s / image) and did not reach near real-time mapping as the

methods in Chapter 3. Other low time cost image features rather than the SUFT for image alignment could be tried to reduce the processing time in the future.

4.9 Literature cited

Abadi, M., Agarwal, A., Barham, P., Brevdo, E., Chen, Z., Citro, C., Corrado, G.S., Davis, A., Dean, J., Devin, M., 2016. Tensorflow: Large-scale machine learning on heterogeneous distributed systems. arXiv preprint arXiv:1603.04467.

Anda, A., Pinter, L., 1994. Sorghum germination and development as influenced by soil temperature and water content. Agronomy Journal 86, 621-624.

Bay, H., Ess, A., Tuytelaars, T., Van Gool, L., 2008. Speeded-up robust features (SURF). Computer vision and image understanding 110, 346-359.

Benvenuti, S., 2003. Soil texture involvement in germination and emergence of buried weed seeds. Agronomy Journal 95, 191-198.

Carter, P.R., Nafziger, E.D., 1990. Uneven emergence in corn.

Chen, R., Chu, T., Landivar, J.A., Yang, C., Maeda, M.M., 2018. Monitoring cotton (Gossypium hirsutum L.) germination using ultrahigh-resolution UAS images. Precision Agriculture 19, 161-177.

Chen, T., Guestrin, C., 2016. Xgboost: A scalable tree boosting system, Proceedings of the 22nd acm sigkdd international conference on knowledge discovery and data mining, pp. 785-794.

Domenech, R., Vila, M., 2008. Cortaderia selloana seed germination under different ecological conditions. acta oecologica 33, 93-96.

Feng, A., Sudduth, K., Vories, E., Zhou, J., 2019. Evaluation of cotton stand count using UAV-based hyperspectral imagery, 2019 ASABE Annual International Meeting. American Society of Agricultural and Biological Engineers, p. 1.

Feng, A., Zhou, J., Vories, E., Sudduth, K.A., 2020a. Evaluation of cotton emergence using UAV-based imagery and deep learning. Computers and Electronics in Agriculture 177, 105711.

Feng, A., Zhou, J., Vories, E., Sudduth, K.A., 2020b. Evaluation of cotton emergence using UAV-based narrow-band spectral imagery with customized image alignment and stitching algorithms. Remote Sensing 12, 1764.

Forcella, F., Arnold, R.L.B., Sanchez, R., Ghersa, C.M., 2000. Modeling seedling emergence. Field Crops Research 67, 123-139.

Ghassemi-Golezani, K., Dalil, B., 2014. Effects of seed vigor on growth and grain yield of maize. Plant Breeding and Seed Science 70, 81-90.

Goodell, P.B., Davis, R.M., Godfrey, L.D., Hutmacher, R.B., Roberts, P.A., Wright, S.D., M, B.V., Haviland, D.R., Munier, D.J., Natwick, E.T., 2015. UC IPM pest management guidelines cotton, Oakland, CA.

Hayes, T., Usami, S., Jacobucci, R., McArdle, J.J., 2015. Using Classification and Regression Trees (CART) and random forests to analyze attrition: Results from two simulations. Psychology and Aging 30, 911.

Jin, X., Liu, S., Baret, F., Hemerlé, M., Comar, A., 2017. Estimates of plant density of wheat crops at emergence from very low altitude UAV imagery. Remote Sensing of Environment 198, 105-114.

Lowe, D.G., 2004. Distinctive image features from scale-invariant keypoints. International Journal of Computer Vision 60, 91-110.

Lundberg, S.M., Erion, G., Chen, H., DeGrave, A., Prutkin, J.M., Nair, B., Katz, R., Himmelfarb, J., Bansal, N., Lee, S.-I., 2020. From local explanations to global understanding with explainable AI for trees. Nature machine intelligence 2, 56-67.

Molnar, C., 2020. Interpretable machine learning. Lulu. com.

Nafziger, E.D., Carter, P.R., Graham, E.E., 1991. Response of corn to uneven emergence. Crop Science 31, 811-815.

Sankaran, S., Khot, L.R., Carter, A.H., 2015. Field-based crop phenotyping: Multispectral aerial imaging for evaluation of winter wheat emergence and spring stand. Computers and Electronics in Agriculture 118, 372-379.

Sankaran, S., Quirós, J.J., Knowles, N.R., Knowles, L.O., 2017. High-resolution aerial imaging based estimation of crop emergence in potatoes. American Journal of Potato Research 94, 658-663.

Sansone, C., Isakeit, T., Lemon, R., Warrick, B., 2002. Texas cotton production: Emphasizing integrated pest management. Texas Cooperative Extension Service, the Texas A & M University System, Texas, USA.

Shapley, L.S., 1953. A value for n-person games. Contributions to the Theory of Games 2, 307-317.

Stewart, S., 2020. Planting depth within-field soil variability effects on corn stand establishment and yield. University of Missouri--Columbia.

Supak, J., 1990. Making replant decisions, 1990 Beltwide cotton production conference. National Cotton Council of America, pp. 45-48.

Szeliski, R., 2007. Image alignment and stitching: A tutorial. Foundations and Trends® in Computer Graphics and Vision 2, 1-104.

Valdés-Rodríguez, O.A., Sánchez-Sánchez, O., Pérez-Vázquez, A., 2013. Effects of soil texture on germination and survival of non-toxic Jatropha curcas seeds. Biomass and Bioenergy 48, 167-170.

Varela, S., Dhodda, P.R., Hsu, W.H., Prasad, P., Assefa, Y., Peralta, N.R., Griffin, T., Sharda, A., Ferguson, A., Ciampitti, I.A., 2018. Early-season stand count determination in corn via integration of imagery from unmanned aerial systems (UAS) and supervised learning techniques. Remote Sensing 10, 343.

Zhao, B., Zhang, J., Yang, C., Zhou, G., Ding, Y., Shi, Y., Zhang, D., Xie, J., Liao, Q., 2018. Rapeseed seedling stand counting and seeding performance evaluation at two early growth stages based on unmanned aerial vehicle imagery. Frontiers in Plant Science 9.

Chapter 5. COTTON DEVELOPMENT VARIATION AFFECTS BY SOIL AND WEATHER

5.1 Abstract

Crop development and production are partly determined by soil conditions, plant available water, and weather conditions. Quantification of their interactions is the key for optimizing field management, such as precision irrigation and fertilization, to achieve optimal production. The goal of this study was to quantify the effects of soil and weather conditions on cotton development and production using temporal areal imagery data and soil apparent electrical conductivity (EC_a) of the field. Soil texture, i.e., sand and clay content, calculated using EC_a based on a model from a previous study, was used to estimate the soil characteristics, including field capacity, wilting point and total available water. Water stress coefficient K_s was calculated using soil texture and weather data. Unmanned aerial vehicle (UAV)-based multispectral imaging systems were used to acquire imagery data at three growth stages of cotton in 2018 and 2019, respectively. Image features of canopy size and several vegetation indices (VIs) were extracted from the derived orthomosaic images. Pearson correlation, analysis of variance (ANOVA) and a machine learning method (XGBoost) were used to quantify the relationships between crop response (variables extracted from UAV images) and environments (soil texture and weather conditions). Results show that the cotton NDVI was various monthly under different soil textures in both 2018 and 2019. Soil clay content in shallower layers (0-0.4 m) affected crop development in early growth stages (June and July) while clay content in deeper layers (0.4-0.7 m) affected the mid-season growth stages (August and September). It was also

found that soil clay content at 0.4-0.7 m had a higher impact on crop development when water inputs were not sufficient, while features related to crop water stress had a higher contribution to the prediction of crop growth when water stress was less. The study indicates that the integration of soil and weather information was able to predict crop growth and yield.

Keywords Cotton; plant growth; soil texture; UAV; multispectral imagery

5.2 Introduction

The world population is estimated to increase by 2 billion in the next 30 years, from 7.7 billion currently to 9.7 billion in 2050, although the growth speed is at a slower pace (United Nations, 2019). It is estimated that global crop production needs to double by 2050 to meet the projected demands from rising population, diet shifts, and increasing biofuels consumption (Alexandratos and Bruinsma, 2012; Hickey et al., 2019; Ray et al., 2013). However, the current yearly increases of crop production for maize (*Zea mays* L.) at 1.6%, rice (*Oryza sativa* L.) at 1.0%, wheat (*Triticum aestivum* L.) at 0.9%, and soybean [*Glycine max* (L.) Merr.] at 1.3% are insufficient to meet the projected demands of ~2.4% in 2050 (Alexandratos and Bruinsma, 2012; Ray et al., 2013). How to improve the production of the major crops has become an impressing pressure to the global research communities (Hatfield and Walthall, 2015).

Crop development and yield are complex and determined by many factors, such as crop genotypes (varieties), growing environments (e.g., weather, soil, microclimate and location), and agronomic management strategies (e.g., seed treatment and placement, planting, fertilizer and pest management) (Cobb et al., 2013). To develop next-generation and high-efficiency agriculture production systems, we will have to solve the complex

equation consisting of the interactions of genotype, environment and management (G×E×M) using emerging technologies (Beres et al., 2020; Russell, 2017; Xin and Tao, 2019). Although crop yield potentials have been improved through advanced crop breeding technologies, the yield gap, i.e., the difference between farm yield (final yield) and potential yield, is still substantial (Beres et al., 2020). Precision agriculture is a promising agriculture practice to increase profitability and reduce the environmental impact using site-specific and accurate measurement of crop, soil and environment (Basso and Antle, 2020; Walter et al., 2017). However, the success of precision agriculture technology heavily relies on the access of accurate and high-resolution spatiotemporal data and reliable prediction models of crop development and yield (Feng et al., 2020b). To-date, most research projects have been focused on development of crop development and yield predication models using single factors, such as crop response to irrigation (Bell et al., 2018; Onder et al., 2005), fertilizer (Cuong et al., 2017; Schut et al., 2018). There are few studies that have integrated effects of environment and management in their prediction due to the lack of data and complex interactions (Beres et al., 2020). In this study, we tested the feasibility of modelling crop development using multiple factors of soil, weather and management practices.

Soil texture is an important soil property related to crop growth (Scherer et al., 2017). The size of solid particles has been used to classify soil texture into different types, including clay (less than 0.002 mm), silt (from 0.002 mm to 0.05 mm) and sand (from 0.05 mm to 2 mm) (Easton and Bock, 2016). The percentages of sand, clay and silt in the soil affect the movement of air and water, as well as the water holding capacity (Bittelli, 2011; Datta et al., 2017; Easton and Bock, 2016). Soil texture is a determining factor for soil

water holding capacity that is one of the important factors affecting crop development. Soil texture can affect seedling emergence date and emergence rate (Forcella et al. (2000)), root development (Oosterhuis, 1990). Soil texture can be measured using a laboratory-based wet chemistry method that is expensive and time-consuming (Vos et al., 2016). An alternative method is to use a sensor-based method that is efficient to acquire data with high spatial resolution and low cost. The most acceptable method is to predict soil texture using soil apparent electrical conductivity (EC_a) with a good calibration (James et al., 2003; Stępień et al., 2015; Sudduth et al., 2005). Many studies have found that soil texture (or soil EC_a) was related to the yield of cotton (Vories et al., 2020), corn (Kitchen et al., 2003; Kitchen et al., 2005) and soybean (Jiang and Thelen, 2004; Kitchen et al., 2005).

Weather conditions, including temperature, wind, humidity and solar irradiance, that are determining factor for crop evapotranspiration and water requirements, also have a great impact on crop development and yield (Allen et al., 1998). Addy et al. (2020) showed that the cereal grain yield had different responses to nitrogen application under various weather conditions during 1968-2016. Tremblay et al. (2012) showed that weather conditions could influence the corn response to nitrogen. Battisti et al. (2018) showed that weather condition was an important component for soybean yield estimation. Van Bussel et al. (2016) used weather data for long-term (30 years) wheat yield estimation.

Compared to crop yield, which is easy to measure and quantify, crop development effects due to the soil texture and weather conditions within a season could be challenging to measure and quantify. Evaluation of crop development by visual observation at field scale is time-consuming and subjective. In recent years, sensor-based methods have provided a promising way to measure and quantify crop development (Bendig et al., 2015;

Hunt et al., 2013). Vegetation indices (VIs) such as normalized difference vegetation index (*NDVI*), chlorophyll vegetation index, triangular greenness index, and green red vegetation index, can be used to quantify the crop growth status (Xue and Su, 2017). Unmanned aerial vehicles (UAVs) equipped with visual sensors, multispectral sensors and/or hyperspectral sensors have been used as a high-throughput data collection tool by many researchers to monitor crop development at the desired time efficiently at field-scale (Feng et al., 2019; Feng et al., 2020a; Feng et al., 2020b; Turner et al., 2014). Studies have used UAV-based remote sensing technologies to estimate crop evaporation (Hoffmann et al., 2016b), crop water status (Romero et al., 2018) and water stress (Gago et al., 2017; Hoffmann et al., 2016a; Zhang et al., 2019). These studies explored the relationships between VIs and evapotranspiration (latent heat flux) calculated by energy balance models, water status measured by pressure bomb, ground measured stomatal conductance and sap flow under different irrigation treatments.

Using UAV-based remote sensing technologies to study the relationships between soil texture (or EC_a), weather conditions and crop development is an important and ongoing topic. For example, Santesteban et al. (2017) and Křížová et al. (2018) showed that the crop canopy temperature captured by a UAV-based thermal camera was related to soil EC_a. This study focused on examining the effects of soil texture and weather conditions on cotton growth variation. The specific objectives included: (1) extracting features of the crop, soil and weather from different sensing systems; and (2) quantifying soil texture and weather effects on cotton growth variation.

5.3 Multi-sensors UAV system and experimental design

To monitor crop development during the whole growth season (from July to September), imagery data were collected using a UAV imaging system integrating a UAV platform (DJI Matrice 600 Pro, DJI, China) with multiple cameras and thermal camera. The multiple cameras used in 2017, June and July of 2018 were an RGB camera (HERO 5, GoPro, San Mateo, CA, USA) and a customized multispectral camera (XNiteCanonElph130, LDP LLC, Carlstadt, NJ, USA). The camera used in August and September of 2018 and in 2019 was a multispectral camera (RedEdge-M, MicaSense Inc., WA, USA). The thermal camera used in all three years was an infrared thermal camera (ICI 8640P, Infrared Cameras Inc., Beaumont, TX, USA). Because the thermal camera had an uncooled detector, it was warmed up by connecting to a power bank for more than half an hour before data collection to produce stable temperature readings. The firmware provided by the thermal camera company was installed on a Raspberry Pi (model 3B, Raspberry Pi Foundation, UK) to collect thermal images at a snapshot rate of 1 s image^{-1} and images were saved on the SD card of the Raspberry Pi. Image data were collected at the east field in 2017 and 2019, and the west field in 2018. The UAV imaging system flew at 30 m above the ground level (AGL) when using the RedEdge-M, and at 50 m AGL when using the HERO 5 and XNiteCanonElph130. The specifications of the cameras, flight height and ground sampling distance (GSD) are listed in Table 5.1: Specifications of the cameras used in the study Table 5.1. The cameras collected images with about 75% overlap in both sideward and forward directions. A UAV control app (Autopilot, Hangar Technology, Austin, TX, USA) was used to plan flight paths and set waypoints, flight speed (7.5 km h^{-1}), and height (30 or 50 m AGL). Imagery data were collected near solar

noon (around 1 pm Central Daylight Time). The specific conditions during image collection in two years are shown in Table 5.2: Weather conditions during imaging. The values are the means and standard deviations from 11 am to 2 pm of the imaging days, i.e., the weather conditions from 11:00 pm to 2:00 pm CDT. The on-board GPS system on the UAV system and on the cameras continuously recorded the coordinates and altitude and provided geo-referencing for each image frame in the metadata of each image. Geo-referenced images were downloaded after the flight for further processing.

Table 5.1: Specifications of the cameras used in the study

Camera type	Model	Spectrum range (nm)	Frame rate (s image^{-1})	Resolution (pixel)	Flight height (m)	GSD * (cm pixel^{-1})
Multispectral	XNiteCanon Elph130	NIR (820 ± 80), R (630 ± 80), G (550 ± 50)	2.5	4608 × 3456	50	1.56
RGB	GoPro Hero5	R-G-B	0.5	4000 × 3000	50	2.6
Multispectral	Micasense RedEdge-M	B (475±10), G (560±10), R (668±5), red-edge (717±5) NIR (840±20)	1	1280 × 960	30	2
Thermal	ICI 8640 P	7,000 – 14,000	1	640 × 512	50	6.8

* GSD = ground sampling distance.

Table 5.2: Weather conditions during imaging. The values are the means and standard deviations from 11 am to 2 pm of the imaging days

Year	Date	Air temperature (ºC)	Relative humidity (%)	Wind speed (m s^{-1})	Solar irradiance (W m^{-2})
2017	Aug. 12	26.8 ± 0.2	63.0 ± 1.0	1.3 ± 0.2	989 ± 35
2018	Jun. 29	29.3 ± 0.5	68.5 ± 1.3	2.3 ± 0.5	759 ± 71
	Jul. 18	30.7 ± 0.3	51.3 ± 1.5	2.8 ± 0.5	737 ± 96
	Aug. 22	25.4 ± 0.3	64.8 ± 2.6	2.0 ± 0.0	655 ± 38
	Sept. 15	30.0 ± 1.2	61.5 ± 4.7	2.5 ± 0.6	773 ± 38

	Jul. 12	31.0 ± 0.9	48.7 ± 4.8	2.0 ± 0.0	914 ± 30
2019	Aug. 14	31.3 ± 0.9	51.0 ± 5.2	1.5 ± 0.6	850 ± 71
	Sept. 6	27.4 ± 1.0	53.0 ± 3.9	2.0 ± 0.0	828 ± 34

Ground truth and reference data, including ground reference points (GRPs) and soil moisture content, were collected prior to UAV flights on the same day as image data collection. In this study, 28 GRPs were randomly set in the field and kept in the same locations for all flights in each growing season. The GRPs consisted of sixteen fence posts (~ 1.1 m in height) with white-black polytechnic boards (0.3 m × 0.3 m) on the top and twelve 0.53 m × 0.53 m squares constructed with half-inch plastic polyvinyl chloride (PVC) pipes on the ground. A ground stake was placed at each GRP to be used as a permanent mark of GPS position in the growing season. A real-time kinematic (RTK) GNSS survey kit (REACH RS+, Emlid Ltd., Saint Petersburg, Russia) was used to obtain the coordinates of the 28 GRPs. Soil samples were obtained at those 28 GRPs at two depths (0-0.075 m and 0.075-0.15 m) in 2019 during imagery data collection. The soil samples were put in sealed plastic bags and weighted in the lab (wet weight). Then the soil samples were put in an oven to dry 24 hours at 105 ºC. Soil samples were weighed again after drying (dry weight). Gravimetric soil moisture content was obtained by Eq. 2.2.

$$Soil\ moiture\ content\ \% = \frac{wet\ weight - dry\ weight}{dry\ weight} \quad (2.2)$$

Soil moisture sensors (TDR-315, Acclima, Meridian, ID, USA) were installed at five selected locations within the field at nominal 0.15, 0.30, 0.45, and 0.60 m depths to measure soil water content. Data loggers (CR206X, Campbell Scientific, Logan, UT, USA) were set to record the data every 15 minutes and wirelessly transmit it to a central computer from July to October each year.

As crop temperature affects by the daily air temperature, five poster boards (1.0 m ×1.5 m) painted with different colors (blue, black, green, white, and yellow) were distributed in the field and their temperature was measured using the thermal camera and a handheld IR thermometer (59 MAX+, FLUKE Corporation, Everett, WA, USA) during the flight each time, as shown in Figure 5.1 . In 2019, not only the five color poster boards, we also included the dry-wet artificial reference surface (including a wet white cotton sheet and a dry black cotton sheet) (Meron et al., 2010) as the reference to check how canopy temperature changes during different daily air temperature, as shown in Figure 5.2.

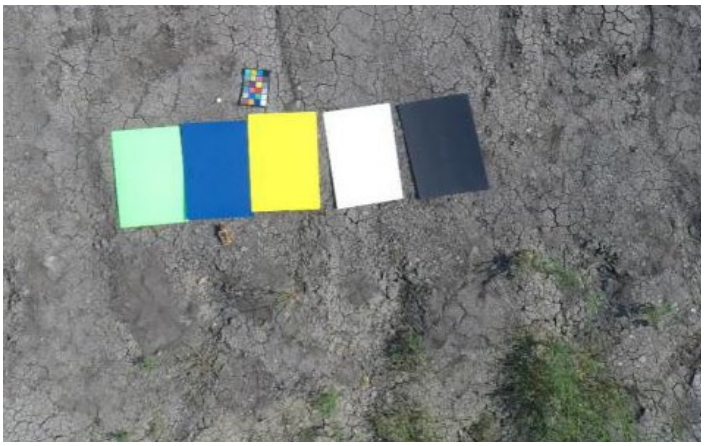

Figure 5.1: Five poster boards painted with different colors.

Figure 5.2: Dry-wet artificial reference surfaces.

5.4 UAV-based multispectral and thermal images processing

Images were uploaded to Agisoft PhotoScan Pro software (Version 1.2.2, Agisoft LLC., Russia) to generate orthomosaic images, which is created out of many individual image frames that have been stitched together and geometrically corrected (Dukowitz, 2017) based on a mosaic blending model described by Brown and Lowe (2003), as shown in Figure 5.3a. The GPS locations of the GRPs were used for GPS calibration of the orthomosaic images.

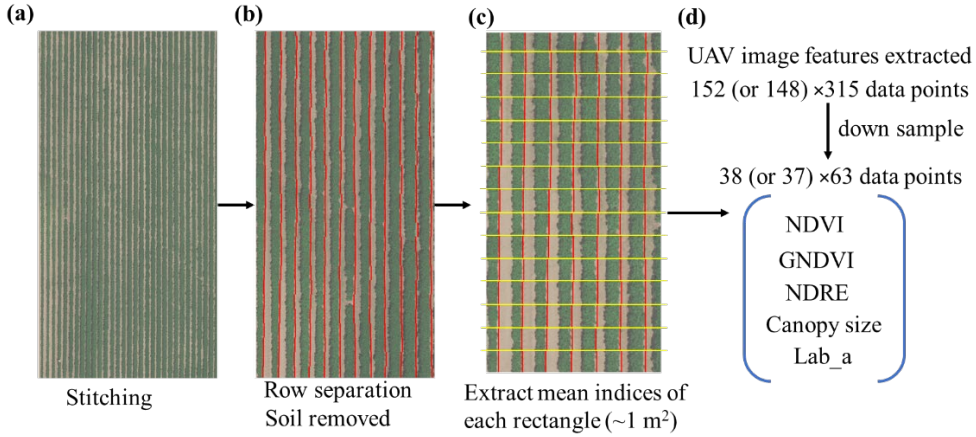

Figure 5.3: Image processing and image feature extraction. (a) Part of an orthomosaic image with corresponding row separation by the red lines and background removal (b). (c) Illustration of unit area (1 m^2) used to extract image features to generate (d) 152 (or 148) × 315 data points of the UAV image features. Then the data points were downsampled to 38 (or 37) × 63 data points. Each data point corresponded to a 4 m × 5 m area of the field.

Each cotton row was identified from the orthomosaic images using the method developed in previous studies (Feng et al., 2019; Feng et al., 2020b) based on the identification of image features along the edge of the crop rows (such as low NDVI and v*

values in hue, saturation, lightness (HSV) color space that represented darker color due to shadows). An example of separated crop rows is shown in Figure 5.3b. Then, the soil background was removed using a threshold of NDVI<0.5 determined by the image histogram (Feng et al., 2020a). Five image features were extracted from each ~1-m^2 rectangle (0.97 m crop row spacing × 1 m length of row based on the GSD calculated by the image resolution, as shown in Figure 5.3c). These image features were NDVI, green normalized difference vegetation index (GNDVI), the normalized difference red edge index (NDRE), the values of a channel in the CIE-LAB color space (a*) and canopy size. These indices have shown to be useful to monitor and evaluate crop growth status in other studies (Table 5.3). For example, canopy size had a strong relationship with crop biomass (Maimaitijiang et al., 2019). Studies found that healthier plants had lower reflectance in the red channel (about 600 nm to 660 nm wavelength) than unhealthy plants so that NDVI values would be higher for the healthier plants (Ihuoma and Madramootoo, 2019). The NDRE calculated by the red edge channel (about 680 nm to 760 nm wavelength) was also useful for nitrogen status evaluation and had a linear relationship with leaf area index (LAI) and chlorophyll content (Hansen and Schjoerring, 2003). GNDVI and a* were related to crop leaf greenness and chlorophyll content (Friedman et al., 2016; Reyes et al., 2017). There were 152 (or 148 in 2018) cotton rows and the fields were about 320 m in the south-north direction, so 152 (or 148) × 315 data points with related image features were obtained (the north and south edges of the field were removed to avoid edge effects). Then, the data points were down sampled to 38 (or 37) × 63 data points by spatial averaging, with each data point equal to 4 cotton rows (matched with the four-row harvested yield data) × 5 m length (integer 315/5 rectangle instead of non-integer 315/4 square). The GPS locations of

the center of each 4 m × 5 m area were also extracted from the geo-referenced orthomosaic images.

Table 5.3: Image features from the three cameras used in this study

Features	Equations	Related traits	References
NDVI	$NDVI = \frac{NIR - R}{NIR + R}$ where *NIR* and *R* are pixel values in the near-infrared and red channels, respectively	Yield, chlorophyll content, biomass	(Dalezios et al., 2001; Hunt et al., 2011; Moges et al., 2005; Ren et al., 2008)
GNDVI	$GNDVI = \frac{NIR - G}{NIR + G}$ where *G* are pixel values in the green channel	Yield, chlorophyll content, biomass	(Hunt et al., 2011; Moges et al., 2005)
NDRE	$NDVI = \frac{NIR - RE}{NIR + RE}$ where *RE* are pixel values in the red edge channel	Crop senescence, maturity	(Barnhart et al., 2019; Thompson et al., 2019)
Canopy size *(CS)*	$CS = \frac{number\ of\ pixels\ of\ crop\ in\ a\ ROI}{overall\ number\ of\ pixels\ \ in\ the\ ROI}$	Yield, biomass, crop density	(Hunt et al., 2011; Liu et al., 2017; Steduto et al., 2012; Walton et al., 2008)
a^*	a^* channel in the CIE-LAB color space; a* represents the green–red color components	Yield, water content, nitrogen, chlorophyll content	(Friedman et al., 2016; Hunt et al., 2013; Reyes et al., 2017; Schwarz et al., 1987)
CWSI	$CWSI = \frac{T_c - T_w}{T_b - T_w}$ where T_c is the crop canopy temperature, T_b is the temperature of the black poster board and T_w is the temperature of the white poster board	Yield, water stress	(Ludovisi et al., 2017; Rischbeck et al., 2016)

[$]ROI: region of interest.

Canopy temperature is also an important variable that has been found to be related to leaf water content and respiration of crops (Baluja et al., 2012; Hoffmann et al., 2016a; Hoffmann et al., 2016b; Ludovisi et al., 2017), and has the potential for yield prediction (Feng et al., 2020b; Rischbeck et al., 2016). The canopy temperature in this study was extracted from the thermal images collected in 2018-2019. The camera readings were factory calibrated using a calibration file provided by the camera supplier.

To validate the readings of the thermal camera, the average temperature of each of the five reference color boards was extracted from the UAV thermal images, and measured

three times using the handheld thermometer (Figure 5.4). The intent of the comparison was not to calibrate the camera, but to validate the sensor readings using an additional device. A linear regression analysis was conducted between the temperature from the thermal camera and the handheld thermometer for the five reference boards, and results show a good fit (R^2 = 0.99 and RMSE = 0.69 °C) between two sensors, indicating the readings of the thermal camera were valid.

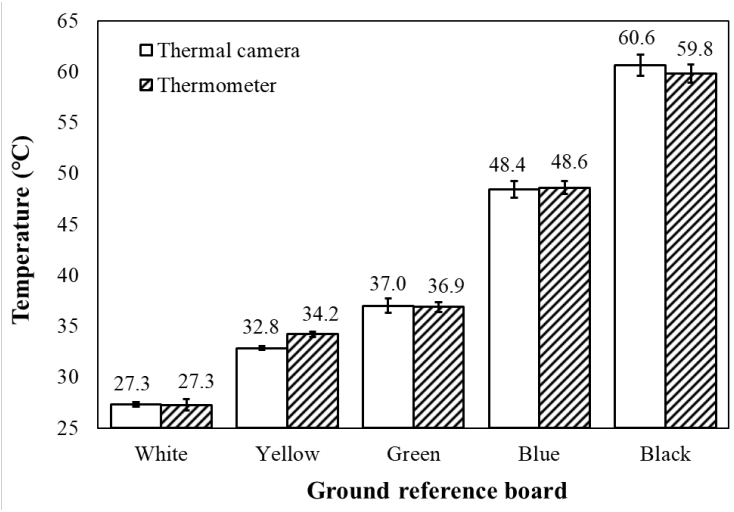

Figure 5.4: Temperature of the ground reference boards measured by the UAV-based thermal camera and handheld thermometer. The numbers above the columns show the means of the measurements.

As crop canopy temperature affects by the daily air temperature, a crop water stress index (*CWSI*) instead of the original canopy temperature was used to quantify the crop water stress and crop growth variation in this study. The *CWSI* used the temperature of the black and white poster boards as the temperature reference.

5.5 Soil and weather data processing

5.5.1 Soil texture data

A soil EC_a survey was conducted in both fields on the same day using the Veris 3100, which measured the soil EC_a at two depths, i.e. shallow (0.3 m, $EC_{a\text{-}sh}$) and deep (1 m, $EC_{a\text{-}dp}$). There were about 5500 EC_a readings (data points) in the research fields (around half in each field). The Kriging method of spatial interpolation was used to generate soil $EC_{a\text{-}sh}$ and $EC_{a\text{-}dp}$ maps (2946×1716 raster for each field, with each grid representing about 0.1 m × 0.1 m area) based on the discrete EC_a points and their GPS coordinates. In this study, a python package pyKrige (Revision db07202a, PyKrige developers adopted from an Open-Source Project. http://pykrige.readthedocs.io) and its build-in variogram models were used to generate the block kriging soil $EC_{a\text{-}sh}$ and $EC_{a\text{-}dp}$ maps. A variogram plot was created. Four variogram models (spherical, exponential, gaussian, cubic models) were fitted to the variogram plot and the exponential model was chosen as it had the lowest RMSE. Then the ordinary kriging estimator was used to predict soil $EC_{a\text{-}sh}$ and $EC_{a\text{-}dp}$ of those unknown points in the raster based on the variogram model and the distance between the unknown points and the measured points (ArcGIS Pro 2.7, 2020; Oliver and Webster, 1990). Once the maps were generated, then soil $EC_{a\text{-}sh}$ and $EC_{a\text{-}dp}$ could be extracted for the grid where the image features were extracted to connect the soil data points and image data. Kriging spatial interpolation was also conducted for the yield data, to allow it to be connected to soil data and image features.

To develop field-wide estimates of soil texture, linear regressions were calculated for laboratory-measured sand and clay content as a function of $EC_{a\text{-}sh}$ (Sudduth et al., 2017; Vories et al., 2020). Calibration data came from profile soil cores that were obtained at

eight locations selected across the field to span differences in EC_a and analyzed by the pedogenic horizon. Combined data from the top two soil horizons (mean depth 0.34 m) yielded the best results, likely because approximately 90% of the $EC_{a\text{-}sh}$ response comes from the top 0.3 m of the soil profile (Sudduth et al., 2003). Results indicated a high correlation between clay and $EC_{a\text{-}sh}$ (R_2=0.85) and between sand and $EC_{a\text{-}sh}$ (R_2= 0.80). These calibrations were then applied to the kriged EC_a datasets to estimate sand and clay for the entire field (EC_a-based sand% and EC_a-based clay%).

Field capacity (*FC*) and wilting point (*WP*) are two variables used to describe the water holding capacity. *FC* is defined as the level of soil moisture content in the soil after water drainage by gravity, and the wilting point is defined as the level of soil moisture content where plants cannot exert enough force to obtain the moisture from the soil (Easton and Bock, 2016; Scherer et al., 2017). The amount of water between field capacity and wilting point can be considered to be the total available water (*TAW*) for plant use. Based on the studies of Saxton et al. (1986) and Saxton and Rawls (2006), the field capacity and wilting point were estimated based on the percentage sand and clay content:

$$FC = (\frac{1}{3\times A})^{\frac{1}{B}} \quad (5.1)$$

$$WP = (\frac{15}{A})^{\frac{1}{B}} \quad (5.2)$$

where *FC* is field capacity (cm^3 water / cm^3 soil) and *WP* is wilting point (cm^3 water / cm^3 soil). *A* and *B* are coefficients that are calculated as:

$$A = e^{(-4.396-0.0715\times C-0.000488\times S^2-0.00004285\times S^2\times C)} \quad (5.3)$$

$$B = -3.14 - 0.00222 \times C^2 - 0.00003484 \times S^2 \times C \quad (5.4)$$

where *C* is the percentage clay content, and *S* is the percentage sand content (the ECa-based sand% and clay% were used in this study). *TAW* could be calculated by Eq. 5.5 (Allen et al., 1998).

$$TAW = 1000 \times (FC - WP) \times Z_r \quad (5.5)$$

where TAW is the total available water (mm), Z_r is the rooting depth (m). Z_r in the emergence stage was set to 0.25 m (Allen et al., 1998; Oosterhuis, 1990; Savva and Frenken, 2002) and in the full development stage was set to 0.69 m based on prior research in fields with irrigation management in the Mid-South (Sui and Vories, 2020). However, because it is difficult for plants to extract all the available water in the soil, a fraction should be applied to the TAW based on a specific crop to calculate the readily available water (RAW) as shown in Eq. 8 (Allen et al., 1998):

$$RAW = \rho\, TAW \quad (5.6)$$

where ρ is the fraction, which was set to 0.6 in this study based on Allen et al. (1998).

In addition, to explore the effects of soil texture at different depths on crop development, clay content in 10-cm layers from the surface to a 70 cm depth was estimated using EC_a data obtained by Veris MSP3 system following the methods developed by Sudduth et al. (2017) with the invVERIS software package (EMTOMO, Odivelas, Portugal), which used a quasi-3D (Q3D) inversion method (Koganti et al., 2017).

5.5.2 Evapotranspiration and water stress coefficient

Crop evapotranspiration determines the crop water requirement and could be estimated by weather parameters and soil conditions. Based on Allen et al. (1998) and Snyder and Eching (2002), daily evapotranspiration of the reference crop (i.e. 20 cm height grass), defined as ET_o, can be calculated using the Penman-Monteith model based on latitude and elevation of the research field, solar radiation, wind speed, dew point temperature, and maximum and minimum air temperature. The American Society of Civil Engineers (ASCE) standardized equation was recommended to simplify the ET_o

calculations (ASCE-EWRI, 2005; Walter et al., 2000). The ET_o of the research field was directly provided from a weather station 400 m from the field using the ASCE standardized equation. The evapotranspiration of cotton was estimated based on the ET_o and the crop coefficient of cotton (K_c) calculated using Eq. 5.7. The appropriate K_c has been found to vary in different growth stages and different crop types (Allen et al., 1998; Hong et al., 2017). The K_c was set to 0.35 in the emergence growth stage and 1.2 in mid-season in this study (Allen et al., 1998; Ko et al., 2009). The length of the crop emergence, crop development and reproductive periods were set to 20, 50 and 55 days respectively (Allen et al., 1998; Ko et al., 2009).

$$ET_c = K_c \times ET_o \qquad (5.7)$$

where ETc is the evapotranspiration of crop and K_c is the crop coefficient of cotton.

Root zone depletion (D_r) could be used to determine the soil water storage relative to field capacity (Allen et al., 1998) with D_r = 0 indicating no depletion of water (at the field capacity level after rain and/or irrigation). The D_r would increase when crops used soil water due to evapotranspiration. A value of $D_r > RAW$ indicates that the readily available water stores in the soil are less than the plant water required, and therefore crops are under water stress. A water stress coefficient (Ks) ranging from 0 to 1 was used to describe the level of crop water stress (Allen et al., 1998). When $D_r < RAW$, K_s = 1, which means no water stress. When $D_r > RAW$, K_s was calculated as:

$$K_s = \frac{TAW - D_{r,i}}{TAW - RAW} \qquad (5.8)$$

where TAW and RAW were calculated based on Eq. 4.5 and Eq. 5.6, $D_{r,i}$ was the D_r on a specific day i and was determined by:

$$D_{r,i} = D_{r,i-1} + ET_{c,i} - P_i - I_i \qquad (5.9)$$

where $D_{r,i-1}$ was the D_r on the last day, $ET_{c,i,}$, $P_{i,}$ and I_i were the ET_c, precipitation and the irrigation amounts for the specific day. Precipitation and/or irrigation amounts greater than D_r were assumed lost through runoff and/or deep percolation below the root zone and were not available to the crop.

Using 2019 data as an example, the daily K_s was calculated for each of the 38 × 63 = 2,394 raster (each data point was the 4 m × 5 m area) using the weather data and irrigation data from May 15 (planting date in 2019) to September 6 (the last date of image collection), or a total of 113 days as shown in Figure 5.5. For each position (or data point) in the 38 × 63 rasters of the 113 days, 113 K_s maps were calculated based on the weather data, irrigation data and soil data using Eq. 5.8 and Eq. 4.9. These two equations connected each day's weather (there were 113 days in Figure 5.5 so that 113 K_s maps were generated) and the spatially variable soil together. After all 113 K_s maps were generated, the following features were calculated (up to the imaging date, i.e. Aug 14 in Figure 5.5) to match each data point of the image features (i.e. images collected on Aug 14 in Figure 5.5) with the soil features raster as shown in Figure 5.5, including K_s on the imaging date; the number of days after planting when Ks < 1 first occurred; the total number of days with K_s < 1 (as well as 0.9 ≤ K_s <1, 0.8≤ K_s <0.9, 0.7≤ K_s <0.8, 0.6≤ K_s <0.7, 0.5≤ K_s <0.6, 0.4≤ K_s <0.5 and K_s <0.4; the K_s was classified as 8 different stress levels); the largest number of continuous days with K_s < 1 (as well as K_s <0.9, K_s <0.8, K_s <0.7, K_s <0.6, K_s <0.5, K_s <0.4 and K_s <0.3). The main reasons for using this method to connect the soil and image feature maps with the K_s maps instead of directly connecting the 113 K_s maps with the image feature and soil raster were: 1) there were many instances of K_s = 1 in the overall 63 × 38 × 113 matrix; and 2) the overall 63 × 38 × 113 matrix was a large matrix and dimension

reduction methods were needed. Similar processing was conducted for the 2018 data from May 16 to Sep 15 (122 K_s maps).

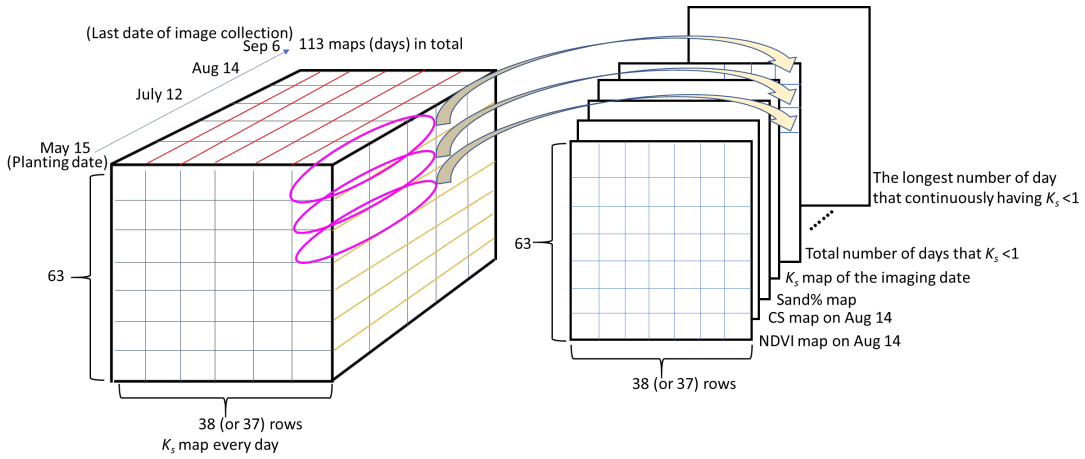

Figure 5.5: The K_s maps and the connection method of soil, image features and K_s maps. K_s was calculated for each position in the 38 (or 37 in 2018) × 63 spatial raster with each K_s map representing a day

5.6 Soil and weather effects on crop development

5.6.1 Data analysis methods

The goal of this study was to evaluate variations in cotton development due to the variation of soil and weather. The soil condition of the field was quantified using the features extracted from EC_a data, including the EC_a-based sand% (the EC_a-based clay% did not be included due to the high linear correlation with the EC_a-based sand% came from the same EC_a data source), EC_a-based clay content percentage in seven different depths of soil (clay10 – clay70), *FC*, *WP*, *TAW* and *RAW*. Soil water input included irrigation data and the watered plots recorded for the center pivot irrigation system and precipitation from the weather station. The K_s feature was calculated based on water input, ET_c (Eq. 4.7) and soil features. The image features extracted were used to represent the crop development.

Pearson correlation coefficients between soil features and image features were calculated to evaluate their relationships. Analysis of variance (ANOVA) was conducted to compare differences in the means of NDVI for different K_s groups and sand% groups using Tukey's Honest method at a 0.05 level of significance. A scalable tree boosting model XGBoost (Chen and Guestrin, 2016) was used to explore how much the soil features and Ks features contributed to the crop growth variation (as quantified by image features). XGBoost, standing for eXtreme Gradient Boosting, is an implementation of gradient boosted decision trees designed for efficiently processing structured or tabular data. The XGBoost model, as one of the tree ensemble methods, included hundreds of decision trees that were trained using soil features and K_s features as inputs and image features as the prediction (outputs) based on an additive strategy. The overall dataset was split into 85% training set and 15% test set, and the training process for each tree used 70% of the training dataset. The XGBoost model has the ability to automatically select features and to address collinearity problems (Hayes et al., 2015). Another benefit of using XGBoost model is that the model can retrieve importance scores for each input feature, indicating how useful or valuable each feature was in the construction of the boosted decision trees within the model (Friedman et al., 2001; Lee, 2017). The developed model was tested using the test dataset and the coefficient of determination (R^2) of a regression between the prediction and true data (imagery features) was used to quantify how well the model explained the true data.

All data analysis was conducted in Matlab (version 2018a, MathWorks, Natick, MA, USA), and in Python software with the packages NumPy (v1.16) (Oliphant, 2006), Pandas (v0.25) (McKinney, 2010) and SciPy (v1.5.2) (Virtanen et al., 2020).

5.6.2 Correlation between soil features and image features

Even though there were nonlinear relationships between EC_a -based sand%, *FC*, *WP* and *TAW* based on Eqs. 4.1-4.6 and between clay contents through the soil profile (clay10-clay70) based on inversion methods using the invVERIS software package, Pearson correlation coefficients (*r*) observed between them were high. For example, correlations were over 0.9 between clay% in every adjacent depth layer (clay10-clay70) as shown in Figure 5.6. This high similarity in clay% distribution between adjacent depth layers can also be seen in Figure 5.7. The first three layers (i.e. 0 to 10 cm, 10 to 20 cm and 20 to 30 cm) had similar spatial clay% distribution patterns with *r* around 0.7-0.9. The last three layers (i.e. 40 to 50 cm, 50 to 60 cm and 60 to 70 cm) also had similar spatial clay distribution patterns with *r* over 0.95. However, the first three layers and the last three layers had different spatial clay distribution patterns with the *r* around 0.2-0.8. Figure 5.7 shows the clay content was higher in the deeper soil layers.

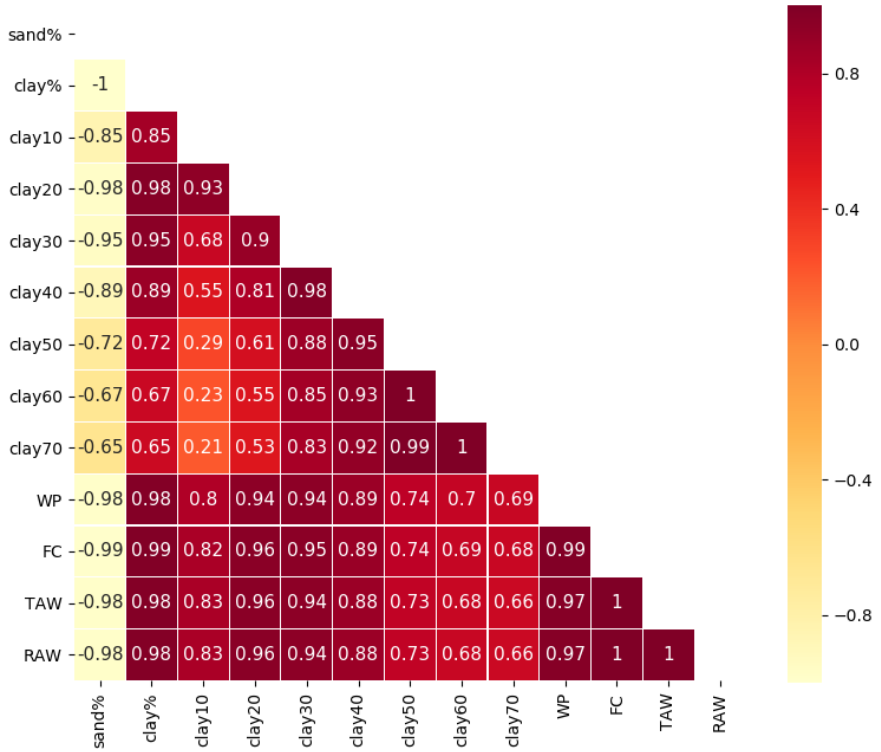

Figure 5.6: Pearson correlation coefficients between soil features. Clay% and sand% are the average EC_a-based clay and sand content in the top two soil horizons.

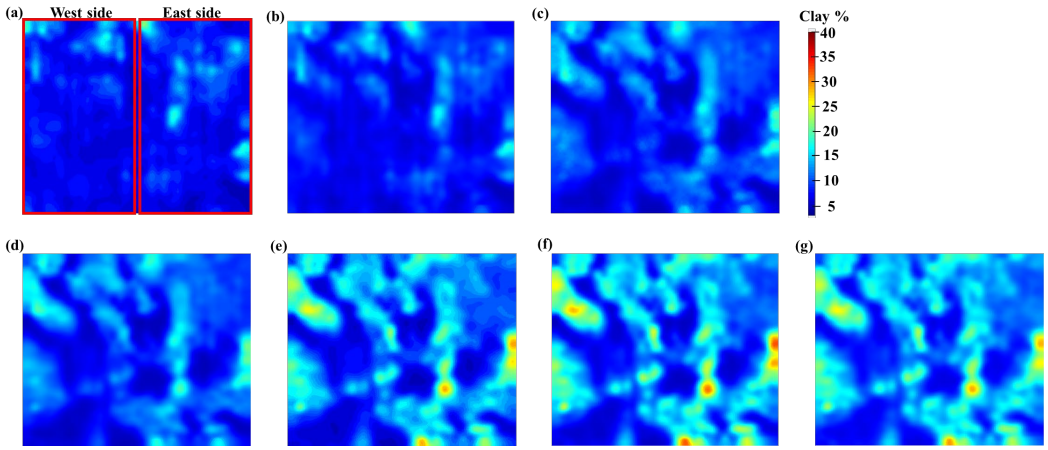

Figure 5.7: Kriged maps of clay content in different depth layers. (a) to (g) are the soil clay% distribution in the field at the seven different depths (clay10 – clay70)

Table 5.4 shows the mean and standard deviation of the 28 soil moisture samples collected in 2019. In July, August and September, the soil had a low average moisture level

around 6%-7% in the top ~15 cm, which was lower than the average calculated WP around the whole field (about 3000 data points in the east field; average WP: 8.73%, FC: 21.48%) and indicated that crop could not obtain water from the upper layers of the soil. The standard deviation in moisture content was around 2% between the 28 samples that had various EC_a-estimated soil textures. Pearson correlation coefficients (r) between soil clay10-clay20 and NDVI, GNDVI, canopy size, and NDRE that represented the crop growth variation of 2019 (Figure 5.8) were as low as 0.2-0.5, and most of them were lower than the r between image features and clay content at other deeper soil layers. The above three points indicated that the clay10-clay20 had low effects on crop growth variation.

Table 5.4: Mean and standard deviation of the moisture content of 28 soil samples in the top 0-0.075 and 0.075-0.15 m

Date	Mean (%)		Std (%)	
	0-0.075 m	0.075-0.15 m	0-0.075 m	0.075-0.15 m
May 7	11.06	13.38	2.46	2.46
May 31	14.52	16.64	3.27	3.04
July 12	6.11	6.86	1.70	1.50
August 14	6.38	-	2.37	-
September 6	7.37	-	1.94	-

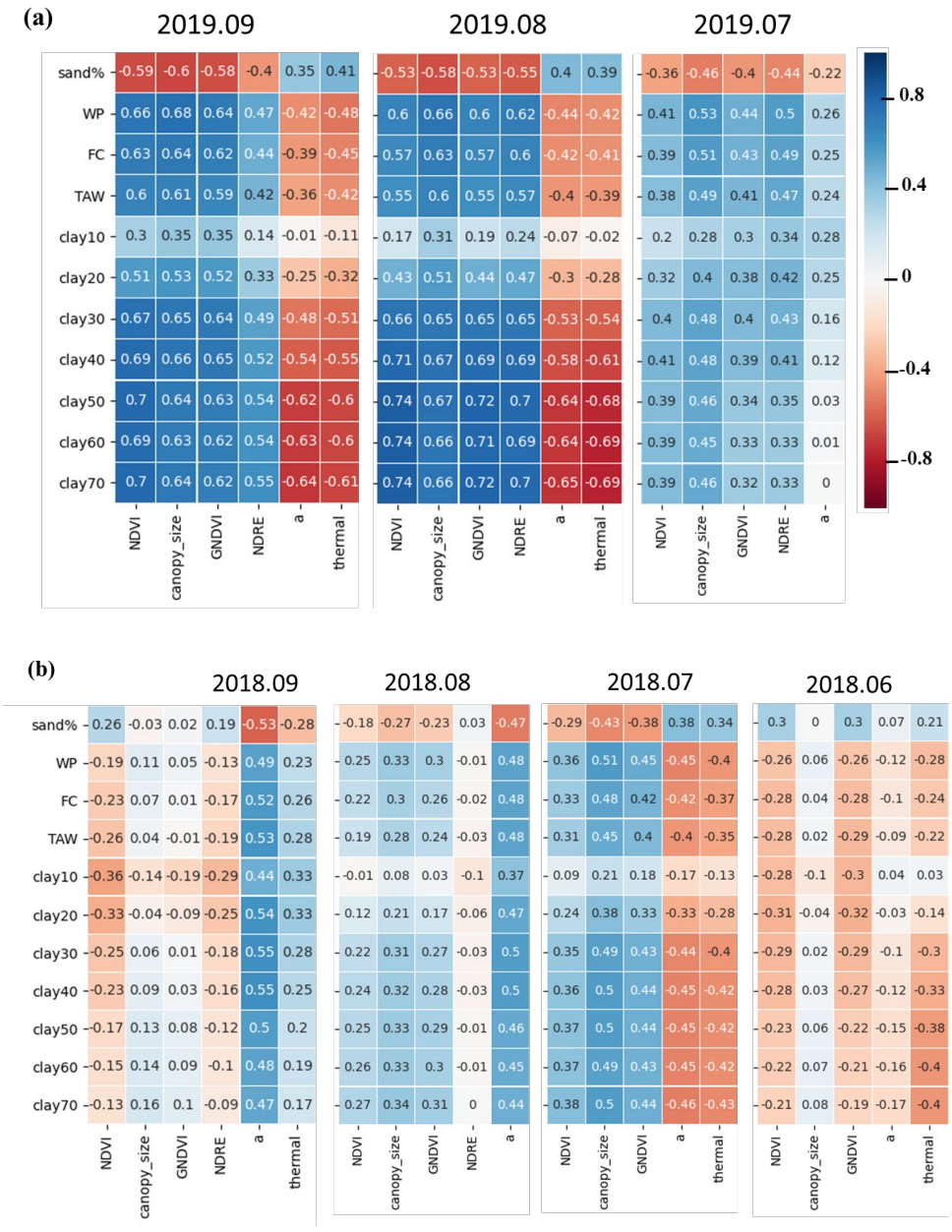

Figure 5.8: Pearson correlation coefficients between soil features and image features. NRRE were not available before August of 2018. Thermal data were not available in August 2018 and July 2019

Clay content in different depths had a different correlation with crop growth during different growth stages (Figure 5.8). The highest *r* values between the clay content and the NDVI, GNDVI, canopy size, and NDRE in Jul. 2019 were around 0.4-0.5 in the middle

layers (i.e., clay30 - clay40), while the highest *r* values in Aug. and Sep. 2019 were around 0.55-0.75 in deeper layers (i.e., clay50 - clay70). The study of Ritchie et al. (2007) showed that the root mass peaked at the flowering stage (Aug.), and the highest mass was at the 55 cm soil depth for a mature cotton plant (Aug. and Sep.). The cotton on July 12, 2019 was 58 days after planting, and the length of the roots may have reached 70 cm depth (Oosterhuis, 1990). However, the mass of the roots may have been small in July in 50-70 cm depth. Based on the crop water requirement curve during the growing season (Allen et al., 1998; Scherer et al., 2017), cotton required less water in the vegetation development stage and early reproductive stage (July) than in the peak reproductive stage (Aug. and Sep.), which may be the reason that the soil clay content had 0.2-0.3 higher *r* with the crop growth in Aug. and Sep. than in July.

The *r* values between soil features (i.e., *WP* and *FC*) and image features (NDVI, GNDVI, canopy size, and NDRE) increased from July to September in 2019 (Figure 5.8). There was 0.8 cm average daily rainfall on 19-27 of June and 0.34 cm on 5-10 of July in 2019 (Figure 2.3), and there was no irrigation during the period. The *r* between soil water holding capacity (*WP* and *FC*) and crop growth variation (NDVI, GNDVI, canopy size, and NDRE) were around 0.4-0.5 on July 12. The r values between soil water holding capacity and crop growth variation were around 0.5-0.6 in Aug. and around 0.6-0.7 in Sep., suggesting that the effect of soil water holding capacity on crop growth status may be a cumulative process.

The *r* values between soil features (i.e., clay% in 0-70 cm) and image features (NDVI, GNDVI, canopy size, and NDRE) were around -0.3-0 in Jun., 0.3-0.5 in July, 0-0.3 in Aug. and -0.3-0 in Sep. of 2018. Due to an equipment error, many of the 7 irrigation

applications in 2018 were applied to the whole field, rather than site-specific, resulting in over-irrigation in parts of the field (see Figure 2.3), and this may be one of the reasons for the low *r* values between clay content and the image features in 2018, which will be discussed with more details in the three following Chapters. Since the irrigation was only conducted three times at a few plots in 2019 but having an over-irrigation problem in 2018 and the crop growth variation had more correlation with soil texture in 2019 than in 2018, we will talk about the data in 2019 before that in 2018 in all following Chapters.

5.6.3 Water stress coefficients

The daily K_s of the 38 × 63 (2019) or 37x63 (2018) positions (raster) of the field were calculated using the Eq. 4.8, and the lowest K_s (min K_s) was checked to decide if water stress presented in the field. As shown in Figure 5.9a there were three periods having min $K_s < 1$ larger than 3 days, beginning on July 9, Aug 1 and Sep. 2 of 2019 as marked by black lines in Figure 5.9a. The K_s returned to 1 again when rains > 1 cm per day occurred on July 16, and Aug. 23. Figure 5.9a shows that the crops imaged in July had experienced only 3 days (from July 9 to July 11) of min $K_s = 0.84$, while the crops imaged in Aug. had a lower min K_s around 0.31 after being subjected to water stress for several days, which matched with the conclusion in the previous Chapter that higher *r* values between clay content and crop growth were found in Aug. 2019 than that in July 2019.

In 2018, images were collected on dates where min $K_s = 0.90$ in June (Figure 5.9b), min $K_s = 0.41$ in July, and non-water stressed days with min $K_s = 1$ in Aug. and Sep. Some regions were irrigated on July 14 and July 17, which was just a few days before image collection. These may be another two reasons that NDVI, GNDVI, canopy size and NDRE have lower *r* values with clay content, *WP* and *FC* in 2018 than those in 2019.

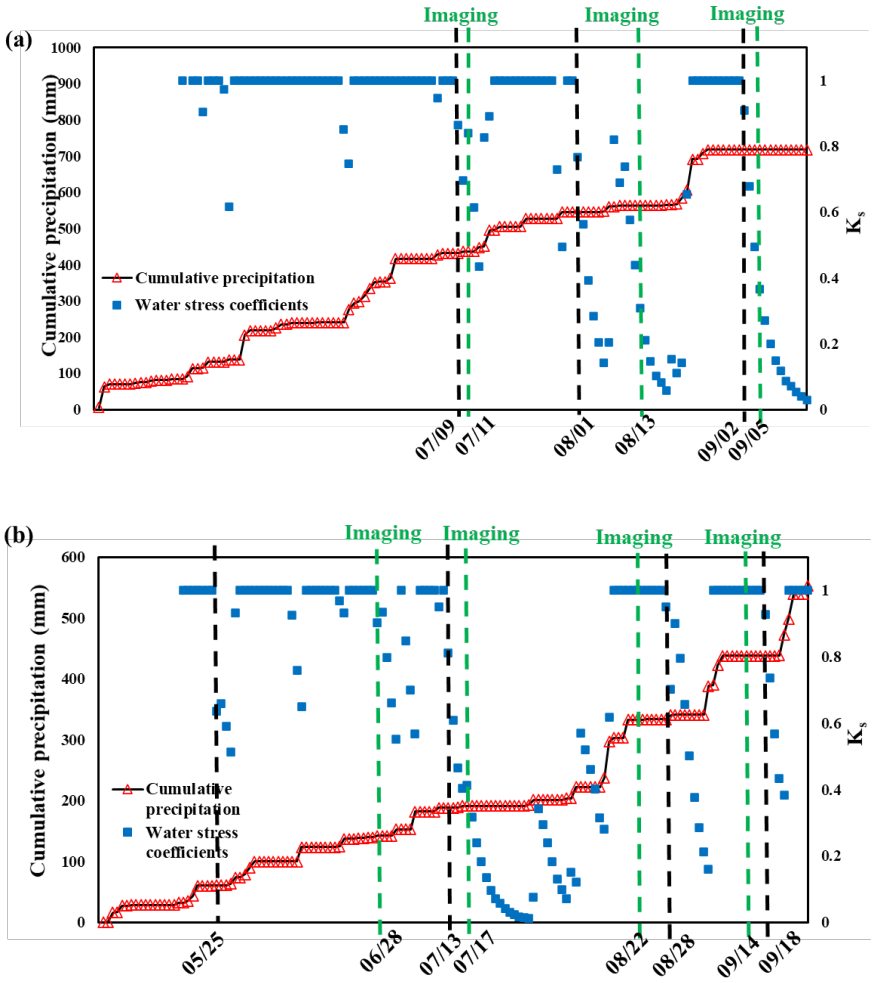

Figure 5.9: Cumulative precipitation and the lowest water stress coefficients in each day of (a) 2019 and (b) 2018. The black vertical lines mark the starting dates for K_s <1. The green lines mark the dates of imaging. Irrigation was site-specific and did not show in the figures

Figure 5.10 shows an example of the K_s maps on Aug. 8, Aug. 10, and Aug. 13 in 2019. Crops were affected by the lack of water beginning on Aug. 1 (Figure 5.9a) and then rainfall on Aug. 7 helped the crop recovered the most on Aug. 8. However, no rainfall and irrigation was applied between Aug. 8- 13, and the lack of water effects accumulated until August 13 resulting in a large variation of K_s due to different soil water storage capacities

(Figure 5.10b-c). The NDVI map collected on Aug 14 (Figure 5.10d) had similar patterns with the K_s map on Aug 13. Figure 5.10e shows the different mean NDVI at different K_s levels. When $K_s < 0.44$, the mean NDVI was 0.77; while, when $K_s > 0.67$, the mean NDVI was 0.89. In the K_s intervals of 0.44-0.56 and 0.56-0.67, a similar mean NDVI of around 0.85 was observed. The result indicated that the K_s has a good correlation with crop growth (NDVI).

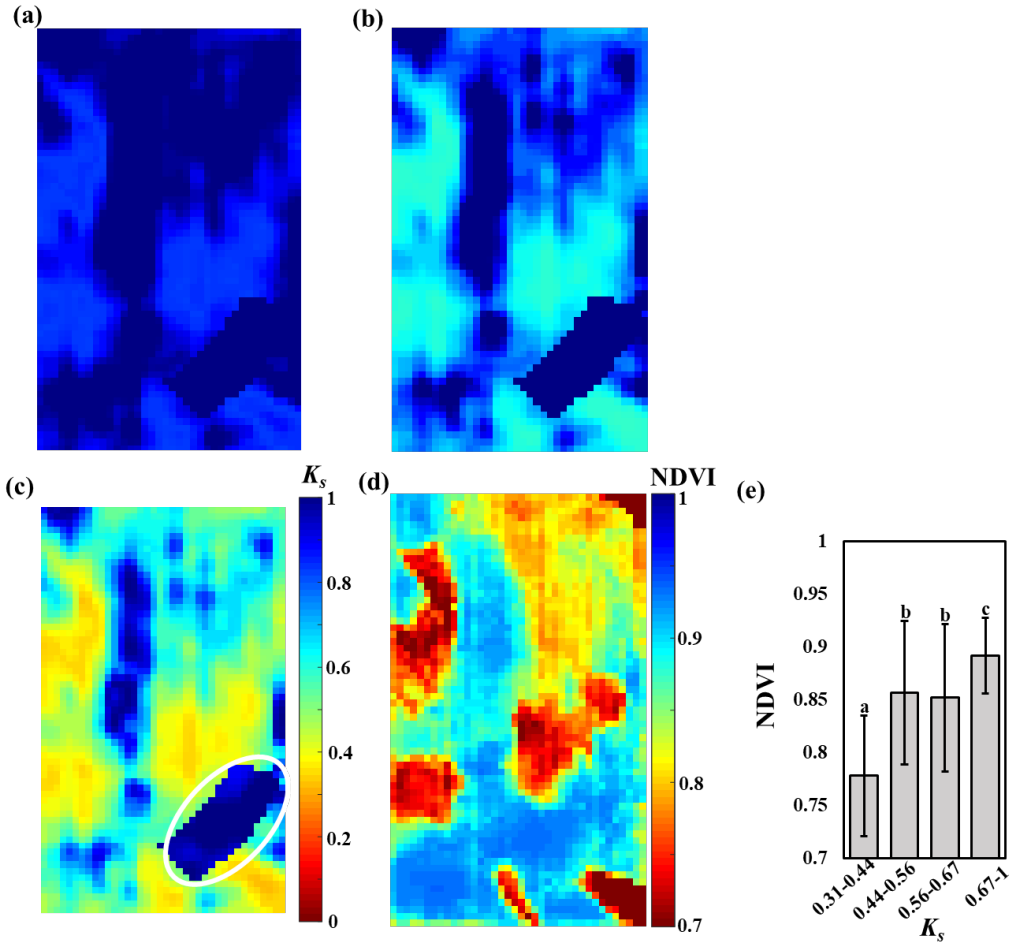

Figure 5.10: K_s maps on (a) Aug 8, (b) Aug 10 and (c) Aug 13. The legend in (c) is also used in (a)-(b). The white circle in (c) marks a plot that had about 22 mm irrigation applied on Aug 6. (d) NDVI map collected on Aug 14. (e) relationship between NDVI and the Aug 13 K_s map. Different lower-case letters indicate a significant difference at

the 5% level of Tukey's honest significant difference test. The mean NDVI in K_s levels from 0-0.25 is 0.77, from 0.25-0.5 is 0.86, from 0.5-0.75 is 0.85, from 0.75-1 is 0.89.

The K_s maps were compared to the thermal data to exam their ability of water stress identification. Firstly, the color poster boards' temperature collection on each imaging date were compared, shown as Figure 5.11. The color poster board's temperature difference can reflect the air temperature difference on the imaging date. The temperature of the white color poster boards did not have too much difference and the different range was around 2 °C. The temperature difference of the yellow, green and blue color poster boards was around 10 °C. The temperature difference of the black poster boards was 7 °C. The Sep. 2018 and Aug. 2019 had the highest temperature of the black poster boards.

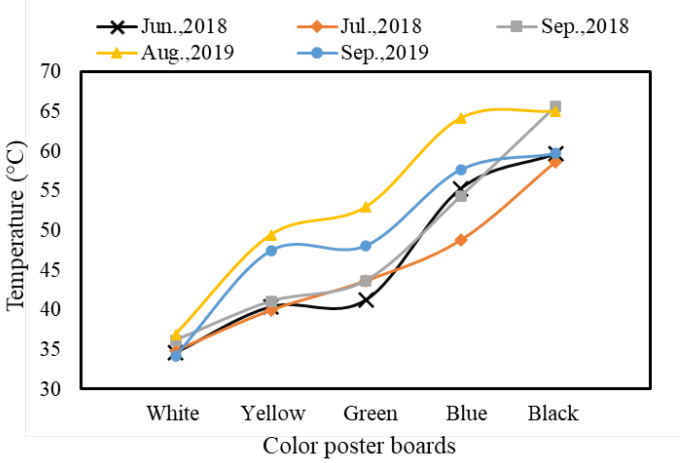

Figure 5.11: Temperature of the five color poster boards on each day of image collection.

Figure 5.12 shows the CWSI maps of Aug. 14 and Sep. 6 in 2019; and K_s maps of Aug. 13 and Sep. 5 in 2019 (since images were collected at noon of the day and the CWSI maps were compared with the Ks maps in the previous days). As mentioned above, min K_s was around 0.31 on Aug. 13 and around 0.37 on Sep. 5 in 2019. The K_s maps showed there was water stress identification on Aug. 13 shown as the marked black circle regions in

Figure 5.12c, which also be identified by the CWSI maps on Aug. 14 shown as the marked black circle regions in Figure 5.12a. The right upper region of the field also was identified as a water stress region in CWSI on Aug. 14 in Figure 5.12a but the K_s map on Aug. 13 in Figure 5.12c did not show too much serious water stress as the other water stress regions in the black circles. CWSI map of Sep. 6 in Figure 5.12b shows less water stress level than that on Aug. 14, and the K_s map of Sep. 5 in Figure 5.12d also shows less water stress level than that on Aug. 13. The K_s maps were estimated water stress level maps based on soil texture and weather condition, while the CWSI maps were the images of the crop canopy. Although they are focus on different objects, they almost gave the same water stress region identification results, which showed that the results of those maps were consistent and both of them could be used as the tool for crop water stress identification.

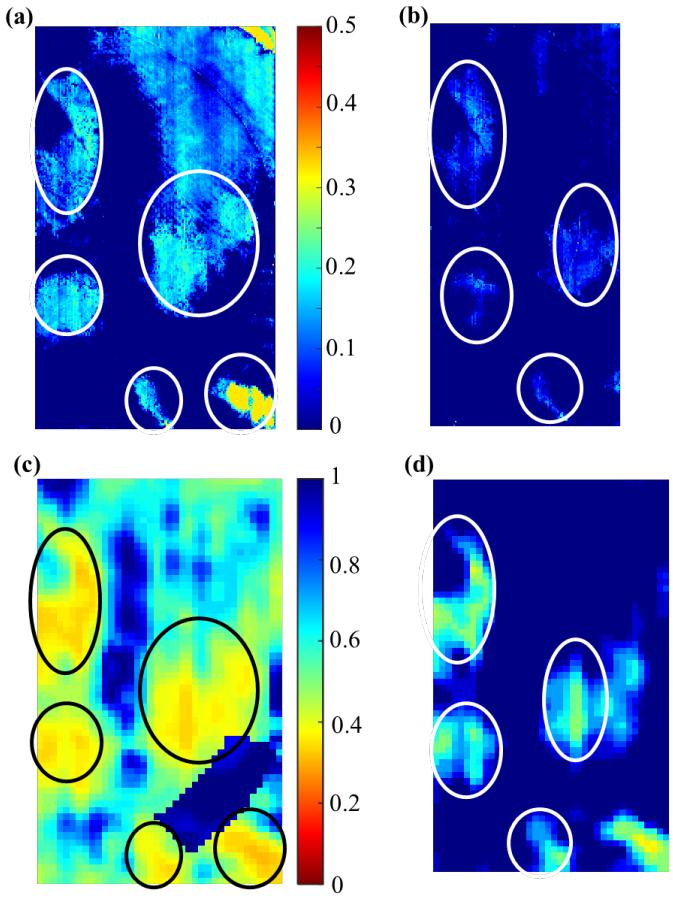

Figure 5.12: CWSI maps of Aug. 14 (a) and Sep. 6 (b) in 2019; and Ks maps of Aug. 13 (c) and Sep. 5 (d) in 2019. There was a problem with the camera on Sep 6, 2019 and the images in (d) were lost of the east edge part of the field. The legend in (a) is also used in (b), and the legend in (c) is also used in (d). The black and white circles mark the regions discussed in the text.

Figure 5.13 shows K_s maps of Jun. 29, Jul. 18 and Sep. 15 in 2018; and K_s maps of Jun. 29, Jul. 18 and Sep. 15 in 2018. Unlike the thermal images collection in 2019, two of the three images were collected in the days that did not have too much water stress identification, with the highest CWSI values of 0.06 on Jun. 29 in Figure 5.13a and of 0.01 on Sep. 15 in Figure 5.13c. Min K_s was around 0.90 on Jun. 29 in Figure 5.13d and 1.0 on

Sep. 15 in Figure 5.13f. Unlike other vegetation indices maps (such as NDVI maps described in Chapter 4.4.4), if no water stress identification on that specific day, CWSI would not show value variation through the field even though the daily air temperature was high (i.e. Sep. 15). If no water stress identification on that specific day, K_s maps also would not show value variation through the field (Figure 5.13c). The min K_s was around 0.41, and it could be seen in Figure 5.13b and Figure 5.13e that the K_s map and the CWSI map almost mark the same regions that identifying water stress. However, the K_s map in Figure 5.13e has a very hard boundary of the irrigation regions, while the boundary of the CWSI was much soft. This is because when calculated the K_s map, only soil, weather and water input were considered, and the irrigation plots were considered as the exact same positions as our irrigation design. But in fact, when irrigation was applied in the field with no physical separation, winds and water flow at the boundary of the irrigation regions could not be accurate control, which resulted in the soft boundary of water stress variation in the CWSI maps. For this reason, the boundary of water stress in the K_s map may not reflect real crop condition, while CWSI captured by UAV thermal images had better performance to indicate water stress than the K_s maps.

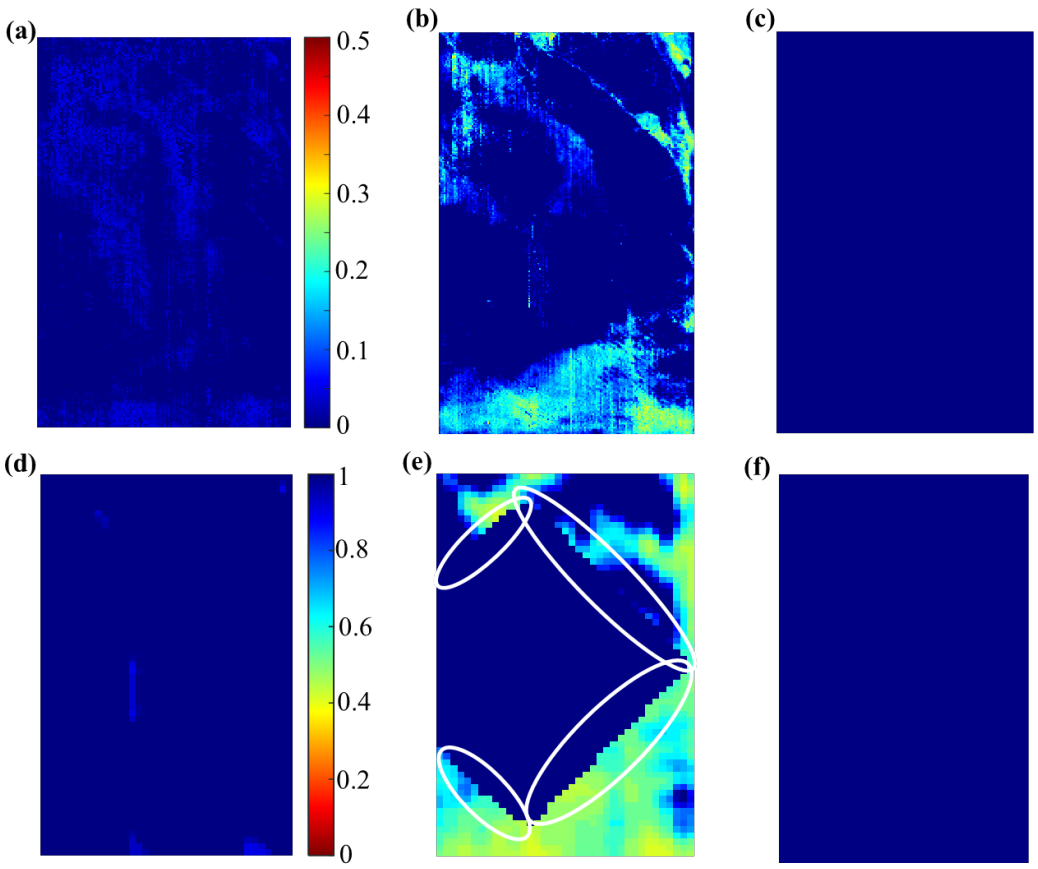

Figure 5.13: CWSI maps of Jun. 29 (a), Jul. 18 (b) and Sep. 15 (c) in 2018; and Ks maps of Jun. 29 (d), Jul. 18 (e) and Sep. 15 (f) in 2018. CWSI map of Aug. 22 in 2018 was not available due to a thermal camera problem. The legend in (a) is also used in (b) and (c), and the legend in (d) is also used in (e) and (f).

5.6.4 Difference in NDVI under various soil and weather conditions

Through comparison of the image features collected through 2018-2019, different crop growth rates under varying soil and weather conditions were observed. The NDVI maps collected in the west field in 2018 and in the east field in 2019 were used as examples here to explain the different growth rates, as shown in Figure 5.14 to Figure 5.19.

Figure 5.14a-c is the NDVI maps of 2019. NDVI in July (Figure 5.14a) ranged from 0.75-0.91 (mean=0.85, Figure 5.15a) within the whole field and Figure 5.16a shows

significant NDVI differences associated with four different sand% groups of the field. However, Figure 5.14b shows that NDVI values in regions with more sand (Figure 5.14d and Figure 5.15d) decreased into the range of [0.6, 0.8] ($0.6 \leq NDVI \leq 0.8$) and increased into [0.8, 0.95] in regions having lower sand content percentage (Figure 5.14d and Figure 5.15d) in Aug. This result was consistent with the results in Figure 5.16 that NDVI dropped from Jul. to Aug. in the (67,89] sand% group ($67 < sand\% \leq 89$) while the other three groups showed NDVI increased from Jul. to Aug. NDVI increased more in the (0,42] sand% group than in the (42,53] and (53,67] sand% groups. Figure 5.14c shows that most of the NDVI values were in the range of [0.85, 0.9] (Figure 5.15c), and only a few values were less than 0.8 in Sep. Some of the NDVI values increased from Aug. to Sep. and some decreased (less than 0.1) as shown in Figure 5.14e and Figure 5.15e. The decreasing values were in the regions with lower sand content. NDVI of the regions that had more sand content increased. Figure 5.16 also shows this trend. The crops in high sand content regions were under water stress from Aug. 8 to Aug. 20 (Figure 5.9a) and the early stress causes the plants to develop more slowly. But the rainfall in 21-28 Aug. helped the stressed crops to recover and the plant started growing more in September with the nitrogen that wasn't used earlier and grows at the time of year that it should be senescing.

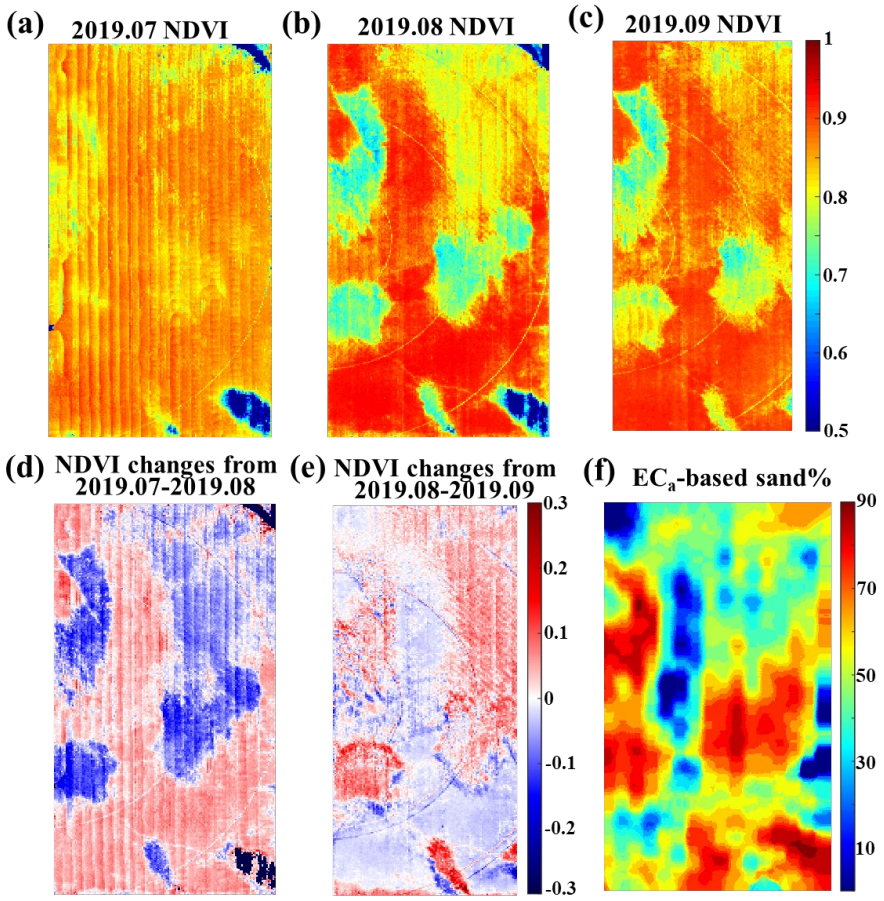

Figure 5.14: NDVI maps collected on east field in 2019. (a)-(c) NDVI of Jul., Aug. and Sep in 2019. There was a problem with the camera on Sep 5, 2019 and the images in (c) were lost of the east edge part of the field. The legend in (c) is also used in (a) and (b). (d)-(e) show the NDVI changes from Jul. to Aug. and Aug. to Sep. in 2019. (f) EC_a-based sand% map of the east field.

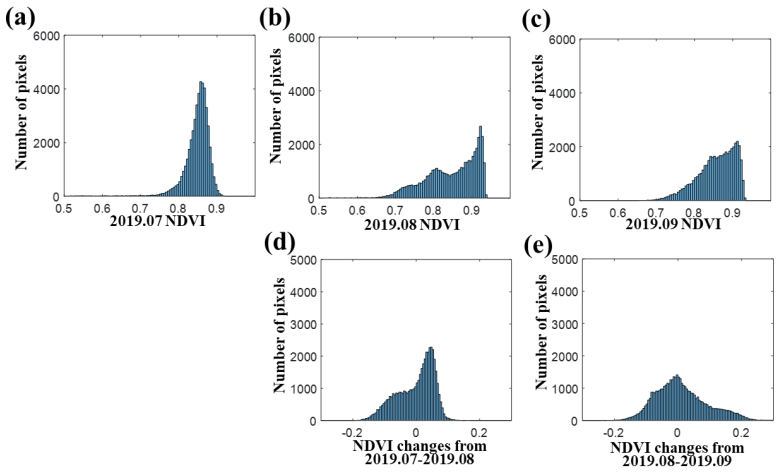

Figure 5.15: (a)-(c) Histogram of NDVI maps of Jul., Aug. and Sep in 2019. (d)-(e) Histogram of NDVI changes from Jul. to Aug. and Aug. to Sep. in 2019.

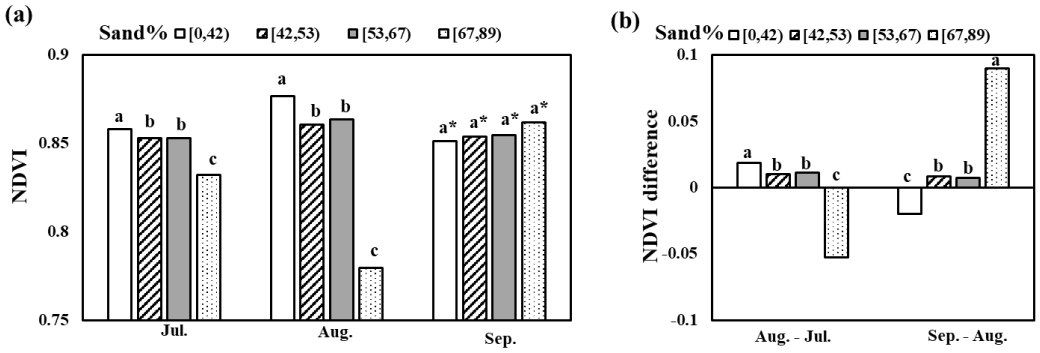

Figure 5.16: (a) Mean NDVI and (b) NDVI difference of four sand% content groups in 2019. ANOVA test was conducted to compare the mean NDVI and its difference in four sand% levels. Different lower-case letters indicate a significant difference at the 5% level of Tukey's honest significant difference test. The results of Sep. 2019 may be misleading due to missing NDVI values on the right side of the field. The sand% groups were split based on quartiles of the soil data of each side of the field.

Difference in NDVI were also observed in 2018 (Figure 5.17a-d and Figure 5.18a-d). No decrease in NDVI was observed from Jun. to Jul. when the crop was in the vegetative development stage, but a potentially different growth rate could be observed as shown in

Figure 5.17e and Figure 5.18e that crops in the regions having higher clay content were associated with a faster NDVI increase. A faster NDVI increase was observed in the (0,50] sand% group and (50,65] sand% group than the (65,72] sand% group and (72,85] sand% group from Jun. to Jul. in Figure 5.19. The camera was changed from XNiteCanonElph130 to Micasense RedEdge-M in Aug. 2018 and the XNiteCanonElph130 camera had a smaller dynamic NDVI range due to the broad spectral bands (Feng et al., 2020b). In order to compare NDVI maps collected by these two cameras, two 40 m × 40 m regions of the field were imaged at the same time using these two cameras and Figure 5.20 shows the NDVI histograms of the collected frames. The region in Figure 5.20a was with full canopy cover and no soil background was observed, while the region in Figure 5.20b was with non-full canopy cover and soil background was observed. NDVI values less than 0.7 in the Micasense image and less than 0.1 in the XNiteCanonElph130 image were soil background. Therefore, there was a 0.60 NDVI shift between these two cameras when the soil background was removed. Obviously, different growth rates were observed in Aug. 2018 in Figure 5.17f and Figure 5.18f, with some of the NDVI decreasing and the other increasing, which was the same trend with the east field of Aug. 2019 in Figure 5.17d. Mean NDVI increased in the (0,50] sand% group (a little bit), (50,65] sand% group and (65,72] sand% group but dropped in the (72,85] sand% group from Jul. to Aug. in Figure 5.19. The mean NDVI in the (0,50] sand% group dropped the most in Sep. 2018. The crop in the low sand content region may have first entered the senescence stage. Higher NDVI values were found in the (50,65] sand% and (65,72] sand% groups than the (0,50] sand% group during the whole 2018 growing season (Figure 5.19). Soil moisture sensor data showed that the (50,65] sand% groups had the highest water content in July (Figure 5.21),

and this result was consistent with the NDVI data in July in Figure 5.19. Soil water content in the (50,65] sand% was still higher than the (0,50] sand% group in Aug. except for the first 0-15 cm depth. The last irrigation was applied on Aug. 7, 2018, and then the soil water content in (0,50] sand% group became the highest one in Sep., resulting from the higher-than-average rainfall (Figure 2.3). However, due to the sufficient soil moisture content in the Jul. and Aug., crop in (50,65] sand% and (65,72] sand% groups still showed high NDVI on Sep. 15.

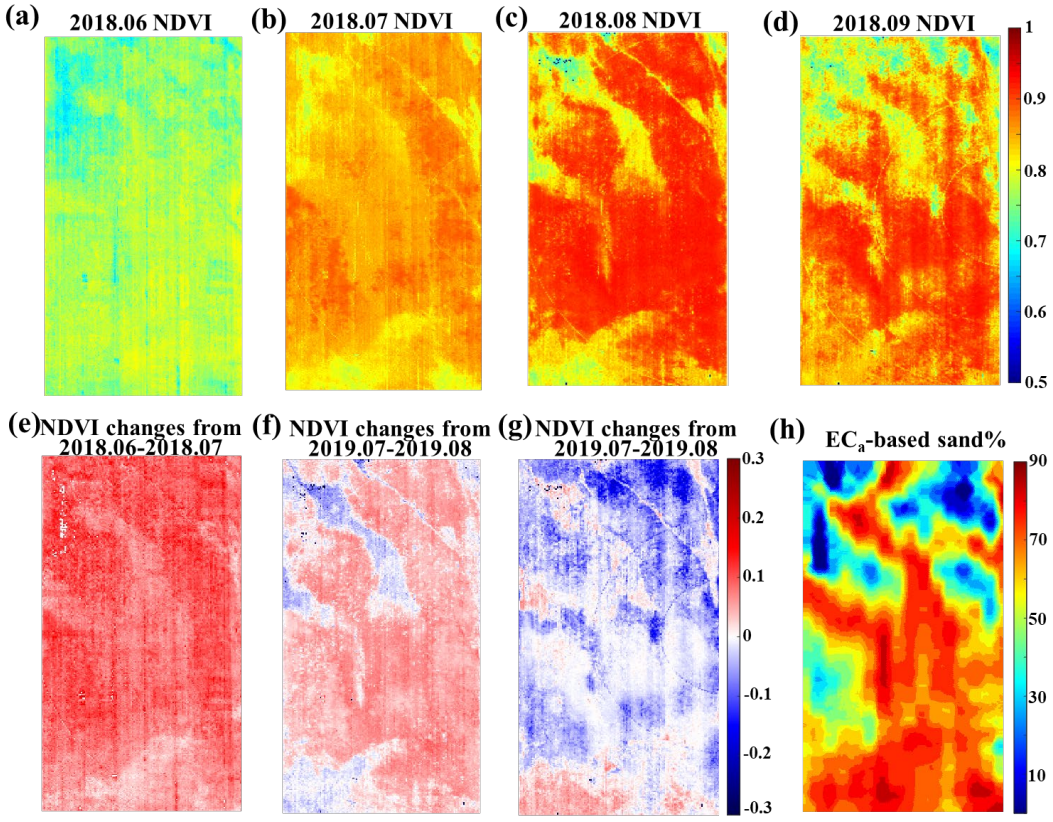

Figure 5.17: NDVI maps collected on the west field in 2018. (a)-(d) NDVI of Jun., Jul., Aug. and Sep in 2018. (e)-(g) NDVI changes from Jun. to Jul., July to Aug. and Aug. to Sep. in 2018. (h) EC_a-based sand% map of the west field.

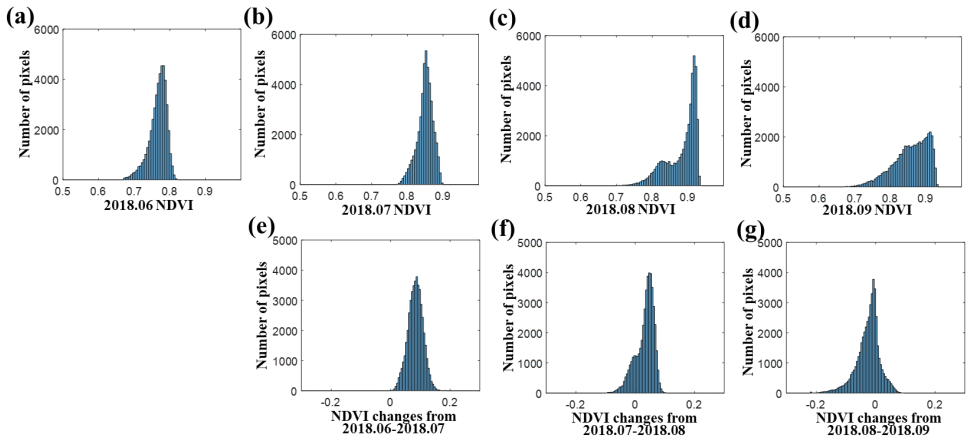

Figure 5.18: (a)-(d) Histogram of NDVI maps of Jun., Jul., Aug. and Sep in 2018. (e)-(g) Histogram of NDVI changes from Jun. to Jul., July to Aug. and Aug. to Sep. in 2018.

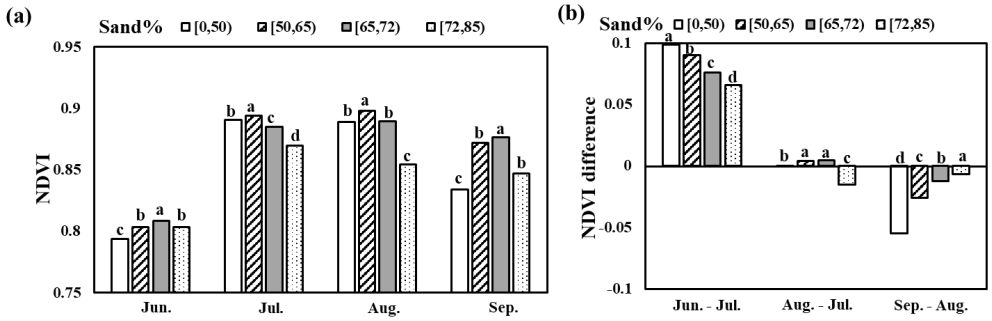

Figure 5.19: (a) Mean NDVI and NDVI difference of four sand% content groups in the year 2018. ANOVA test was conducted to compare the mean NDVI in different sand% levels. Different lower-case letters indicate a significant difference at the 5% level of Tukey's honest significant difference test. The sand% groups were split based on quartiles of the soil data of each side of the field

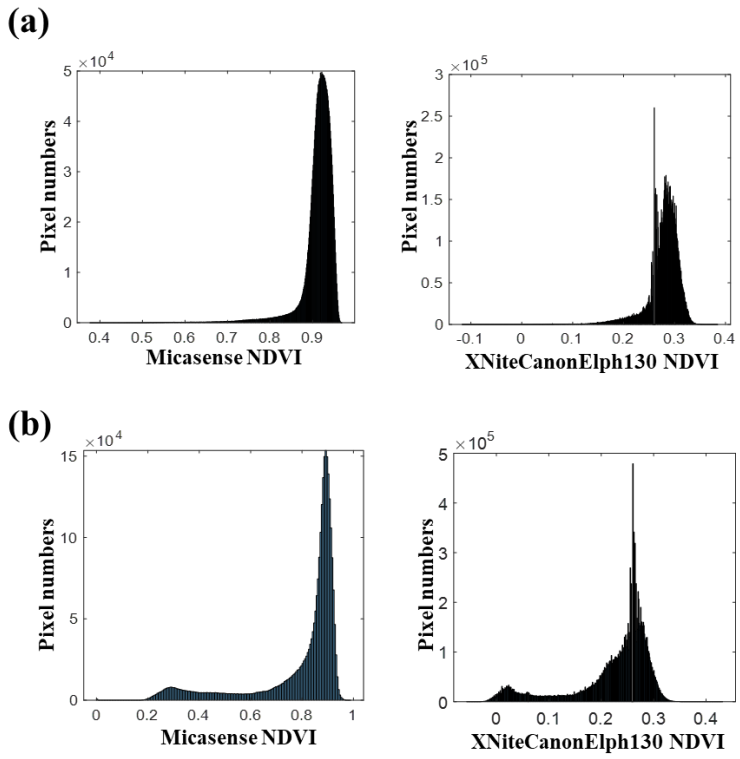

Figure 5.20: Histogram compares two NDVI images collected by two cameras at the same time with (a) full canopy cover and no soil background visible and (b) non-full canopy cover and soil background visible.

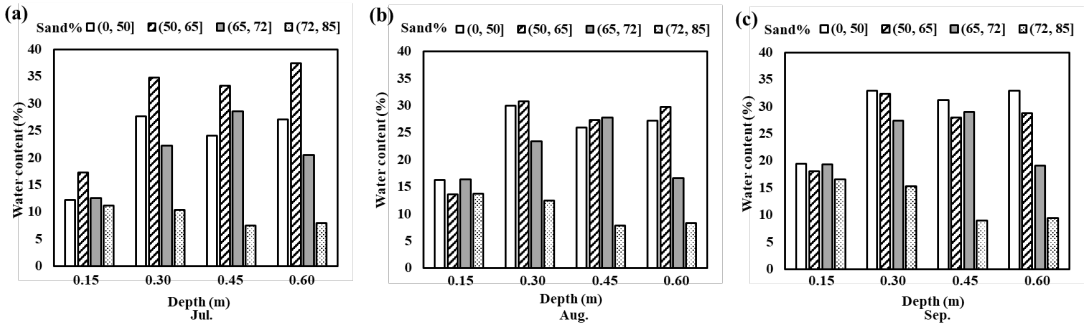

Figure 5.21: Soil moisture content (%) in different sand% groups at 4 different depth (0.15, 0.30, 0.45 and 0.60 m) in (a) Jul., (b) Aug. and (c) Sep. in 2018

5.6.5 The effects of soil and weather features on crop growth

To explore the contribution of soil and weather features on crop growth, the soil features and K_s features were used as the inputs to train the XGBoost model to predict each image feature and yield. Table 5.3 shows the R^2 obtained for the test set. The R2 in Aug. and Sep. in 2019 were around 0.6-0.7 and Jul., Aug. and Sep. in 2018 were around 0.5-0.6. Soil features and K_s features cannot fit the variance of the crop growth accurately in the early growth stages (i.e. Jul. 2019 and Jun. 2018) with R^2 around 0.2-0.4. The accuracy of yield prediction based on soil and weather features increased from Jun. (R^2 = 0.57) to Jul.-Sep. (around 0.62) in 2018 as well as from Jul. (0.65) to Aug.-Sep. (around 0.7) in 2019.

Table 5.5: R^2 for each image features predicted by soil features and K_s features on the test set

	2019			2018			
	July	Aug	Sep	June	July	Aug	Sep
NDVI	0.40	0.75	0.73	0.29	0.59	0.65	0.62
Canopy size	0.52	0.72	0.77	0.29	0.60	0.53	0.52
GNDVI	0.46	0.73	0.65	0.26	0.56	0.54	0.53
NDRE	0.39	0.70	0.54	-*	-	0.50	0.50
Lab_a	0.22	0.65	0.65	0.28	0.56	0.59	0.55
Yield	0.65	0.70	0.71	0.57	0.64	0.62	0.62

* XNiteCanonElph130 did not have red-edge spectral band.

The XGBoost model could not fit the crop growth variation accurately in June 2018 when all the plants were small (could not explain the June 2018 data well), therefore they were not used to analyze feature contribution. Figure 5.22 shows the feature contribution of soil features and K_s features for each image feature and yield in July, Aug. and Sep in 2018 and 2019 based on the analysis of the decision trees built into the XGBoost model,

with the percentage (%) represented the ratio of a specific feature used in trees to the total trees of the XGBoost (details of the first five important features are shown in Fig. S4 in the Supplementary data).

Figure 5.22 shows that there are more grids with darker red color in the soil features rather than K_s features with image features and yield in 2019, indicating that soil features might contribute more than the K_s features did to crop development. The contribution of clay content at deeper layers (i.e., contribution cumulated from all the clay40 to clay70) accounted for 34%-58% (Figure 5.23a) to each of the prediction of NDVI, GNDVI, a* and NDRE in Aug 2019, while the shallow layers (i.e. contribution cumulated from all the clay10 to clay30) contributed less. However, the contribution of the clay content at deep layers (i.e., contribution cumulated from all the clay40 to clay70) dropped to 16-40% (Figure 5.23a) in September. The longest period of days continuously having K_s <0.3 (L_0.3 in Figure 5.22) was 7%-13% (Figure 5.23a) contribution to the NDVI, GNDVI, a* and NDRE prediction in Aug. This may indicate that crops' development might be seriously affected if they were under a long period of K_s <0.3. Clay content percentage at deep layers (i.e. clay40 to clay70) had about 33%-69% (Figure 5.23a) contribution on the final yield prediction. In summary, the result indicated the clay content in deeper layers played an important role to crop development in 2019. It also showed that L_0.3 was a more important feature than other K_s features to the crop growth in Aug.

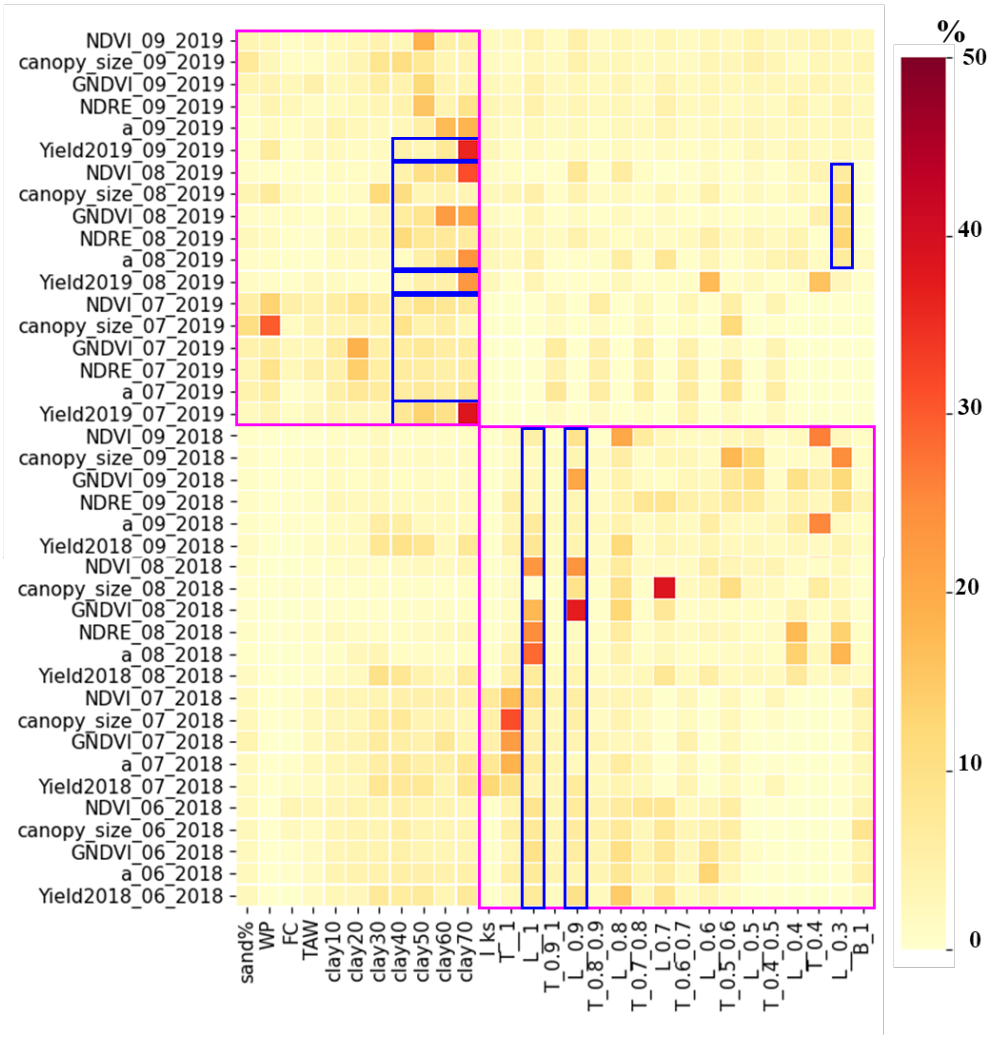

Figure 5.22: Heat map for the feature importance (%) of soil features and K_s features for each image feature and yield. I_ K_s: the K_s in the imaging date; T_1: total days having K_s <1; T_0.9_1: total days having K_s in [0.9,1]; L_1: the largest number of continuous days having K_s <1; B_1: number of days after planting to first instance of K_s <1. Yield_2019_08_2019: the K_s features for the 2019 yield estimation were calculated from the date of planting to the imaging date in Aug. The pink and blue boxes mark the values described in the text

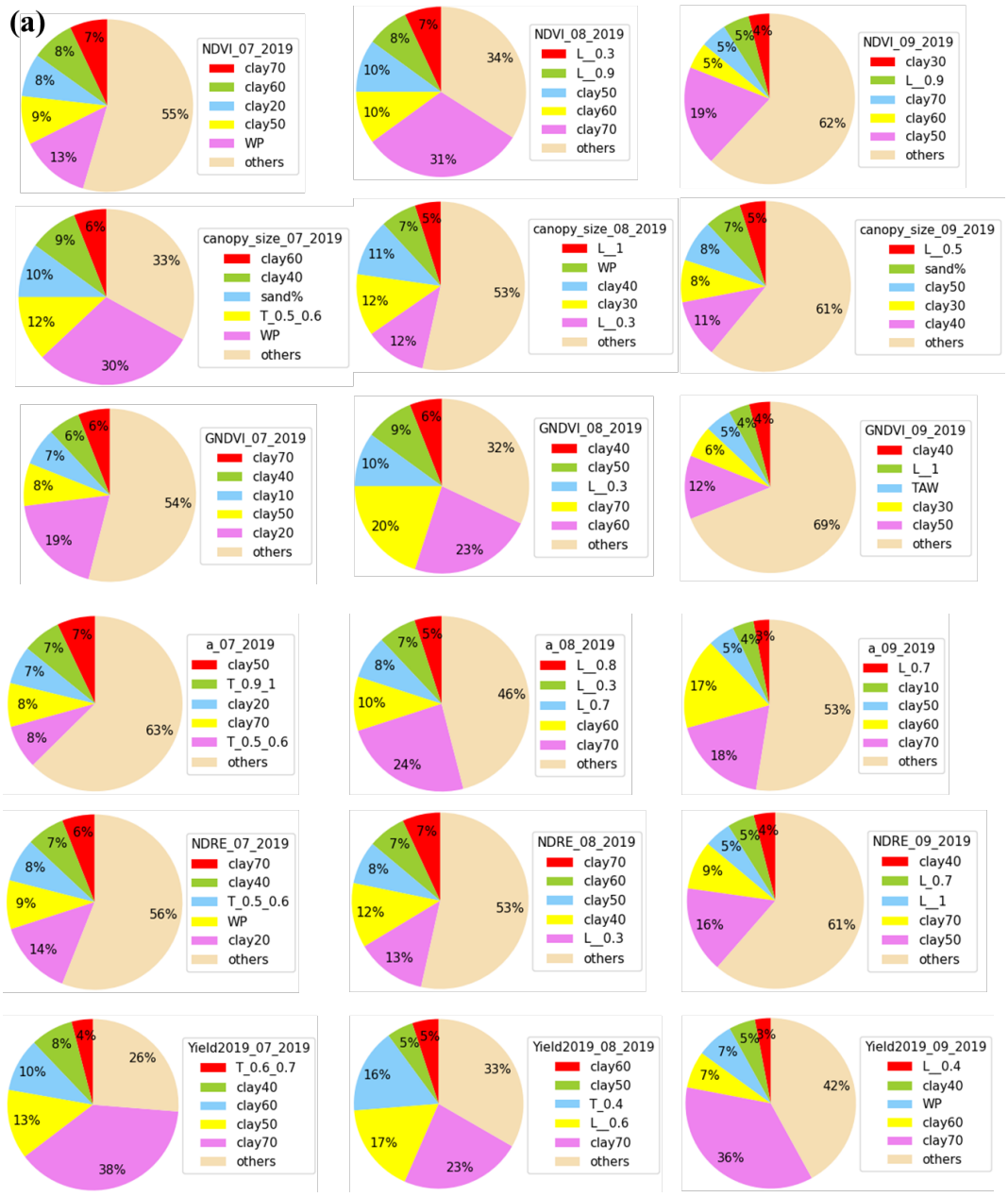
(a)
NDVI_07_2019
clay70 7%
clay60 8%
clay20 8%
clay50 9%
WP 13%
others 55%
NDVI_08_2019
L__0.3 7%
L__0.9 8%
clay50 10%
clay60 10%
clay70 31%
others 34%
NDVI_09_2019
clay30 4%
L__0.9 5%
clay70 5%
clay60 5%
clay50 19%
others 62%
canopy_size_07_2019
clay60 6%
clay40 9%
sand% 10%
T_0.5_0.6 12%
WP 30%
others 33%
canopy_size_08_2019
L__1 7%
WP 5%
clay40 11%
clay30 12%
L__0.3 12%
others 53%
canopy_size_09_2019
L__0.5 7%
sand% 5%
clay50 8%
clay30 8%
clay40 11%
others 61%
GNDVI_07_2019
clay70 6%
clay40 6%
clay10 7%
clay50 8%
clay20 19%
others 54%
GNDVI_08_2019
clay40 6%
clay50 9%
L__0.3 10%
clay70 20%
clay60 23%
others 32%
GNDVI_09_2019
clay40 4%
L__1 4%
TAW 5%
clay30 6%
clay50 12%
others 69%
a_07_2019
clay50 7%
T_0.9_1 7%
clay20 7%
clay70 8%
T_0.5_0.6 8%
others 63%
a_08_2019
L__0.8 7%
L__0.3 5%
L_0.7 8%
clay60 10%
clay70 24%
others 46%
a_09_2019
L_0.7 5%
clay10 4%
clay50 3%
clay60 17%
clay70 18%
others 53%
NDRE_07_2019
clay70 6%
clay40 7%
T_0.5_0.6 8%
WP 9%
clay20 14%
others 56%
NDRE_08_2019
clay70 7%
clay60 7%
clay50 8%
clay40 12%
L__0.3 13%
others 53%
NDRE_09_2019
clay40 4%
L_0.7 5%
L__1 5%
clay70 9%
clay50 16%
others 61%
Yield2019_07_2019
T_0.6_0.7 4%
clay40 8%
clay60 10%
clay50 13%
clay70 38%
others 26%
Yield2019_08_2019
clay60 5%
clay50 5%
T_0.4 16%
L__0.6 17%
clay70 23%
others 33%
Yield2019_09_2019
L__0.4 3%
clay40 5%
WP 7%
clay60 7%
clay70 36%
others 42%

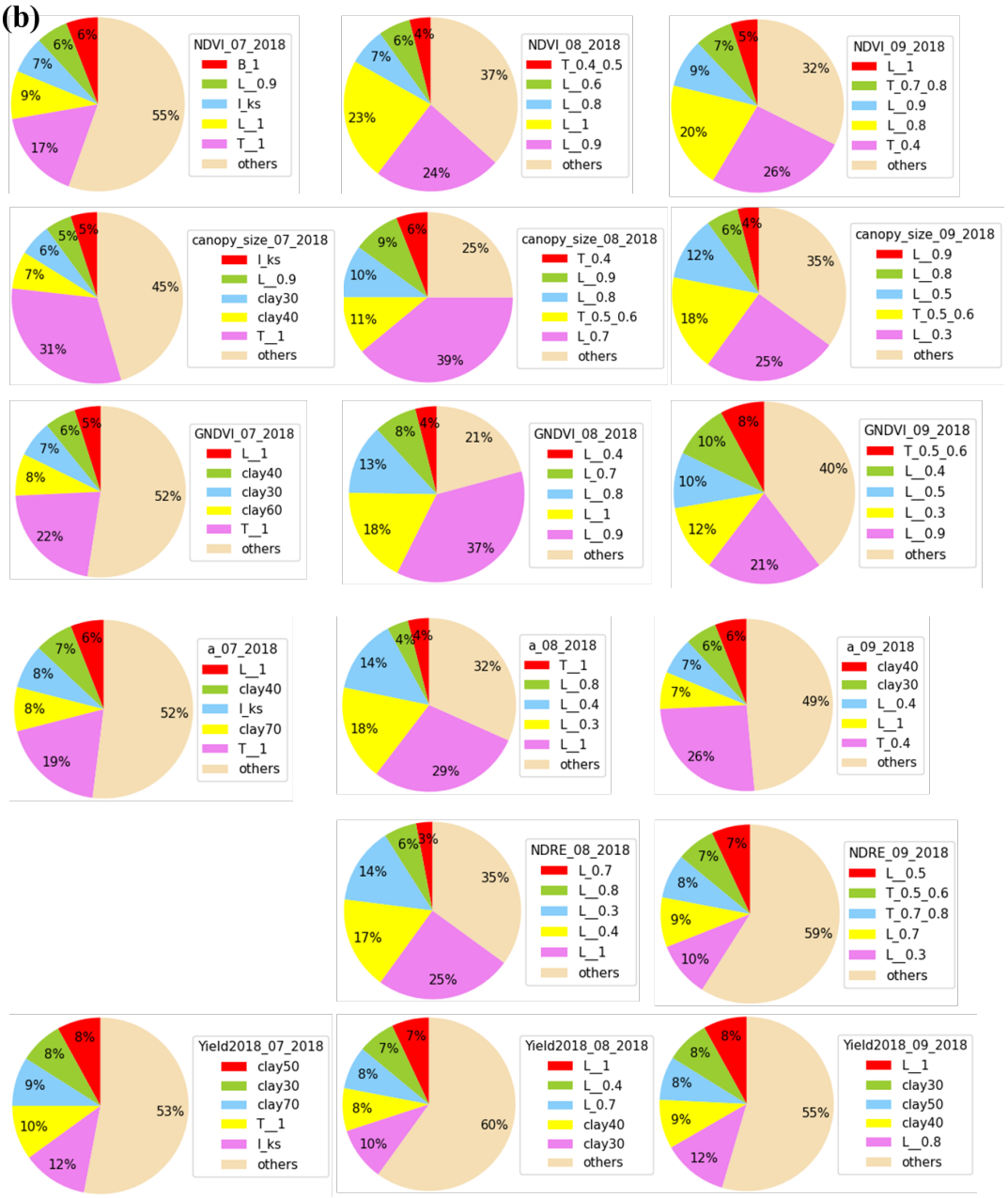

Figure 5.23: Feature contribution (%) of the five highest and remainder (as 'others') soil features and K_s features for each image feature and yield in (a) 2019 and (b) 2018. XNiteCanonElph130 camera did not have a red-edge spectral band and *NDRE* was not available in July 2018

In addition, Figure 5.23b shows the feature contribution (%) of soil and K_s features for the prediction of each image feature and yield in 2018. It can be seen from the figure that the feature contribution of the overall soil features was less than 20% in the prediction of all the image features in Aug. and September. On the other hand, the K_s features had higher feature contribution values to the image feature prediction, especially L_1 and L_0.9 whose contribution values were 25%-55% on the prediction of NDVI, GNDVI, a* and NDRE. The different patterns showing in 2018 and 2019 might be due to more irrigation applied in 2018 and crops being less affected by the soil water capacity. The feature contribution value of soil feature on yield estimation in 2018 decreased to 18%-25%, which was 15%-44% lower than that in 2019. In summary, K_s is a good feature to explore crop growth variation with fields having irrigation applied.

5.7 Conclusion

This study investigated the impact of soil texture, moisture and weather conditions on cotton growth variation that was quantified by crop growth image features from UAV-based multispectral images collected in 2018 and 2019. Soil features such as clay content, field capacity, wilting point and water holding capacity were calculated and calibrated based on soil EC_a data. The water stress coefficient K_s was calculated using weather, irrigation and soil data. Pearson correlation, ANOVA and XGBoost models were developed to explore the relationship of soil features and K_s features with crop growth. Results showed that difference in NDVI were found in both 2018 and 2019 under varying EC_a-based soil texture. Soil features and K_s features did not fit the crop growth variation well in the early growth stages when crops do not require a large amount of water and soil water storage is sufficient. Soil features and K_s features had a higher correlation with image

features in middle growth stages. Soil features had a stronger correlation with crop development when crops suffered from water stress. Clay content in shallow layers affected crop development in early growth stages while clay content in the deeper layers affected the middle growth stages. The K_s features were important indicators of crop growth variation if irrigations were applied. The results showed that investigating the soil and weather data corresponding with UAV image data is feasible to exam the effects of soil and weather on crop growth variation.

5.8 Literature cited

Addy, J.W., Ellis, R.H., Macdonald, A.J., Semenov, M.A., Mead, A., 2020. Investigating the effects of inter-annual weather variation (1968–2016) on the functional response of cereal grain yield to applied nitrogen, using data from the Rothamsted Long-Term Experiments. Agricultural and Forest Meteorology 284, 107898.

Alexandratos, N., Bruinsma, J., 2012. World agriculture towards 2030/2050: the 2012 revision.

Allen, R., Pereira, L., Raes, D., Smith, M., 1998. Crop evapotranspiration-Guidelines for computing crop water requirements-FAO Irrigation and drainage paper 56. Fao, Rome 300, D05109.

ArcGIS Pro 2.7, 2020. How kriging works.

ASCE-EWRI, 2005. The ASCE standardized reference evapotranspiration equation. ASCE Reston, Va.

Baluja, J., Diago, M.P., Balda, P., Zorer, R., Meggio, F., Morales, F., Tardaguila, J., 2012. Assessment of vineyard water status variability by thermal and

multispectral imagery using an unmanned aerial vehicle (UAV). Irrigation Science 30, 511-522.

Barnhart, I., Rosso, L.M., Secchi, M., Ciampitti, I., 2019. Evaluating sorghum senescence patterns using small unmanned aerial vehicles and multispectral iImaging. Kansas Field Research 2019, 166.

Basso, B., Antle, J., 2020. Digital agriculture to design sustainable agricultural systems. Nature Sustainability 3, 254-256.

Battisti, R., Bender, F.D., Sentelhas, P.C., 2018. Assessment of different gridded weather data for soybean yield simulations in Brazil. Theoretical and Applied Climatology.

Bell, J.M., Schwartz, R., McInnes, K.J., Howell, T., Morgan, C.L., 2018. Deficit irrigation effects on yield and yield components of grain sorghum. Agricultural Water Management 203, 289-296.

Bendig, J., Yu, K., Aasen, H., Bolten, A., Bennertz, S., Broscheit, J., Gnyp, M.L., Bareth, G., 2015. Combining UAV-based plant height from crop surface models, visible, and near infrared vegetation indices for biomass monitoring in barley. International Journal of Applied Earth Observation and Geoinformation 39, 79-87.

Beres, B.L., Hatfield, J.L., Kirkegaard, J.A., Eigenbrode, S.D., Pan, W.L., Lollato, R.P., Hunt, J.R., Strydhorst, S., Porker, K., Lyon, D., Ransom, J., Wiersma, J., 2020. Toward a Better Understanding of Genotype × Environment × Management Interactions—A Global Wheat Initiative Agronomic Research Strategy. Frontiers in Plant Science 11.

Bittelli, M., 2011. Measuring soil water content: A review. HortTechnology 21, 293-300.

Chen, T., Guestrin, C., 2016. Xgboost: A scalable tree boosting system, Proceedings of the 22nd acm sigkdd international conference on knowledge discovery and data mining, pp. 785-794.

Cobb, J.N., DeClerck, G., Greenberg, A., Clark, R., McCouch, S., 2013. Next-generation phenotyping: requirements and strategies for enhancing our understanding of genotype–phenotype relationships and its relevance to crop improvement. Theoretical and Applied Genetics 126, 867-887.

Cuong, T.X., Ullah, H., Datta, A., Hanh, T.C., 2017. Effects of silicon-based fertilizer on growth, yield and nutrient uptake of rice in tropical zone of Vietnam. Rice Science 24, 283-290.

Dalezios, N., Domenikiotis, C., Loukas, A., Tzortzios, S., Kalaitzidis, C., 2001. Cotton yield estimation based on NOAA/AVHRR produced NDVI. Physics and Chemistry of the Earth, Part B: Hydrology, Oceans and Atmosphere 26, 247-251.

Datta, S., Taghvaeian, S., Stivers, J., 2017. Understanding soil water content and thresholds for irrigation management.

Dukowitz, Z., 2017. What is an orthomosaic map? How these maps are helping catch bad guys, grow grops, and geep people safe.

Easton, Z.M., Bock, E., 2016. Soil and soil water relationships. Virginia Cooperative Extension.

Feng, A., Zhang, M., Sudduth, K.A., Vories, E.D., Zhou, J., 2019. Cotton yield estimation from UAV-based plant height. Transactions of the ASABE 62, 393-404.

Feng, A., Zhou, J., Vories, E., Sudduth, K.A., 2020a. Evaluation of cotton emergence using UAV-based narrow-band spectral imagery with customized image alignment and stitching algorithms. Remote Sensing 12, 1764.

Feng, A., Zhou, J., Vories, E.D., Sudduth, K.A., Zhang, M., 2020b. Yield estimation in cotton using UAV-based multi-sensor imagery. Biosystems Engineering 193, 101-114.

Forcella, F., Arnold, R.L.B., Sanchez, R., Ghersa, C.M., 2000. Modeling seedling emergence. Field Crops Research 67, 123-139.

Friedman, J., Hastie, T., Tibshirani, R., 2001. The elements of statistical learning. Springer series in statistics, New York, NY, USA.

Friedman, J.M., Hunt, E.R., Mutters, R.G., 2016. Assessment of leaf color chart observations for estimating maize chlorophyll content by analysis of digital photographs. Agronomy Journal 108, 822-829.

Gago, J., Fernie, A.R., Nikoloski, Z., Tohge, T., Martorell, S., Escalona, J.M., Ribas-Carbó, M., Flexas, J., Medrano, H., 2017. Integrative field scale phenotyping for investigating metabolic components of water stress within a vineyard. Plant Methods 13, 90.

Hansen, P., Schjoerring, J., 2003. Reflectance measurement of canopy biomass and nitrogen status in wheat crops using normalized difference vegetation indices and partial least squares regression. Remote Sensing of Environment 86, 542-553.

Hatfield, J.L., Walthall, C.L., 2015. Meeting Global Food Needs: Realizing the Potential via Genetics × Environment × Management Interactions. Agronomy Journal 107.

Hayes, T., Usami, S., Jacobucci, R., McArdle, J.J., 2015. Using Classification and Regression Trees (CART) and random forests to analyze attrition: Results from two simulations. Psychology and Aging 30, 911.

Hickey, L.T., A, N.H., Robinson, H., Jackson, S.A., Leal-Bertioli, S.C.M., Tester, M., Gao, C., Godwin, I.D., Hayes, B.J., Wulff, B.B.H., 2019. Breeding crops to feed 10 billion. Nat Biotechnol 37, 744-754.

Hoffmann, H., Jensen, R., Thomsen, A., Nieto, H., Rasmussen, J., Friborg, T., 2016a. Crop water stress maps for an entire growing season from visible and thermal UAV imagery. Biogeosciences 13, 6545.

Hoffmann, H., Nieto, H., Jensen, R., Guzinski, R., Zarco-Tejada, P., Friborg, T., 2016b. Estimating evaporation with thermal UAV data and two-source energy balance models. Hydrology and Earth System Sciences 20, 697-713.

Hong, M., Zeng, W., Ma, T., Lei, G., Zha, Y., Fang, Y., Wu, J., Huang, J., 2017. Determination of growth stage-specific crop coefficients (Kc) of sunflowers (Helianthus annuus L.) under salt stress. Water 9, 215.

Hunt, E.R., Doraiswamy, P.C., McMurtrey, J.E., Daughtry, C.S.T., Perry, E.M., Akhmedov, B., 2013. A visible band index for remote sensing leaf chlorophyll content at the canopy scale. International Journal of Applied Earth Observation and Geoinformation 21, 103-112.

Hunt, E.R., Hively, W.D., McCarty, G.W., Daughtry, C.S.T., Forrestal, P.J., Kratochvil, R.J., Carr, J.L., Allen, N.F., Fox-Rabinovitz, J.R., Miller, C.D., 2011. NIR-green-blue high-resolution digital images for assessment of winter cover crop biomass. GIScience & Remote Sensing 48, 86-98.

Ihuoma, S.O., Madramootoo, C.A., 2019. Crop reflectance indices for mapping water stress in greenhouse grown bell pepper. Agricultural Water Management 219, 49-58.

James, I., Waine, T., Bradley, R., Taylor, J., Godwin, R., 2003. Determination of soil type boundaries using electromagnetic induction scanning techniques. Biosystems Engineering 86, 421-430.

Jiang, P., Thelen, K., 2004. Effect of soil and topographic properties on crop yield in a north-central corn–soybean cropping system. Agronomy Journal 96, 252-258.

Kitchen, N., Drummond, S., Lund, E., Sudduth, K., Buchleiter, G., 2003. Soil electrical conductivity and topography related to yield for three contrasting soil–crop systems. Agronomy Journal 95, 483-495.

Kitchen, N., Sudduth, K., Myers, D., Drummond, S., Hong, S., 2005. Delineating productivity zones on claypan soil fields using apparent soil electrical conductivity. Computers and Electronics in Agriculture 46, 285-308.

Ko, J., Piccinni, G., Marek, T., Howell, T., 2009. Determination of growth-stage-specific crop coefficients (Kc) of cotton and wheat. Agricultural Water Management 96, 1691-1697.

Koganti, T., Moral, F., Rebollo, F., Huang, J., Triantafilis, J., 2017. Mapping cation exchange capacity using a Veris-3100 instrument and invVERIS modelling software. Science of The Total Environment 599, 2156-2165.

Křížová, K., Kroulík, M., Haberle, J., Lukáš, J., Kumhálová, J., 2018. Assessment of soil electrical conductivity using remotely sensed thermal data. Agronomy Research.

Lee, C., 2017. Feature importance measures for tree models.

Liu, S., Baret, F., Allard, D., Jin, X., Andrieu, B., Burger, P., Hemmerlé, M., Comar, A., 2017. A method to estimate plant density and plant spacing heterogeneity: application to wheat crops. Plant methods 13, 38.

Ludovisi, R., Tauro, F., Salvati, R., Khoury, S., Mugnozza Scarascia, G., Harfouche, A., 2017. UAV-Based Thermal Imaging for High-Throughput Field Phenotyping of Black Poplar Response to Drought. Frontiers in Plant Science 8, 1681.

Maimaitijiang, M., Sagan, V., Sidike, P., Maimaitiyiming, M., Hartling, S., Peterson, K.T., Maw, M.J., Shakoor, N., Mockler, T., Fritschi, F.B., 2019. Vegetation index weighted canopy volume model (CVMVI) for soybean biomass estimation from unmanned aerial system-based RGB imagery. ISPRS Journal of Photogrammetry and Remote Sensing 151, 27-41.

McKinney, W., 2010. Data structures for statistical computing in python, Proceedings of the 9th Python in Science Conference. Austin, TX, pp. 51-56.

Meron, M., Tsipris, J., Orlov, V., Alchanatis, V., Cohen, Y., 2010. Crop water stress mapping for site-specific irrigation by thermal imagery and artificial reference surfaces. Precision agriculture 11, 148-162.

Moges, S., Raun, W., Mullen, R., Freeman, K., Johnson, G., Solie, J., 2005. Evaluation of green, red, and near infrared bands for predicting winter wheat biomass, nitrogen uptake, and final grain yield. Journal of Plant Nutrition 27, 1431-1441.

Oliphant, T.E., 2006. A guide to NumPy. Trelgol Publishing USA.

Oliver, M.A., Webster, R., 1990. Kriging: a method of interpolation for geographical information systems. International Journal of Geographical Information System 4, 313-332.

Onder, S., Caliskan, M.E., Onder, D., Caliskan, S., 2005. Different irrigation methods and water stress effects on potato yield and yield components. Agricultural water management 73, 73-86.

Oosterhuis, D.M., 1990. Growth and development of a cotton plant. Nitrogen Nutrition of Cotton: Practical Issues, 1-24.

Ray, D.K., Mueller, N.D., West, P.C., Foley, J.A., 2013. Yield Trends Are Insufficient to Double Global Crop Production by 2050. PLOS ONE 8, e66428.

Ren, J., Chen, Z., Zhou, Q., Tang, H., 2008. Regional yield estimation for winter wheat with MODIS-NDVI data in Shandong, China. International Journal of Applied Earth Observation and Geoinformation 10, 403-413.

Reyes, J.F., Correa, C., Zúñiga, J., 2017. Reliability of different color spaces to estimate nitrogen SPAD values in maize. Computers and Electronics in Agriculture 143, 14-22.

Rischbeck, P., Elsayed, S., Mistele, B., Barmeier, G., Heil, K., Schmidhalter, U., 2016. Data fusion of spectral, thermal and canopy height parameters for improved yield prediction of drought stressed spring barley. European Journal of Agronomy 78, 44-59.

Ritchie, G.L., Bednarz, C.W., Jost, P.H., Brown, S.M., 2007. Cotton growth and development. Cooperative Extension Service and the University of Georgia College of Agricultural and Environmental Sciences, Athens, GA, USA.

Romero, M., Luo, Y., Su, B., Fuentes, S., 2018. Vineyard water status estimation using multispectral imagery from an UAV platform and machine learning algorithms

for irrigation scheduling management. Computers and Electronics in Agriculture 147, 109-117.

Russell, K., 2017. Genotype× Environment× Management: Implications for selection to heat stress tolerance and nitrogen use efficiency in Soft Red Winter Wheat.

Santesteban, L., Di Gennaro, S., Herrero-Langreo, A., Miranda, C., Royo, J., Matese, A., 2017. High-resolution UAV-based thermal imaging to estimate the instantaneous and seasonal variability of plant water status within a vineyard. Agricultural Water Management 183, 49-59.

Savva, A.P., Frenken, K., 2002. Crop water requirements and irrigation scheduling. FAO Sub-Regional Office for East and Southern Africa Harare.

Saxton, K., Rawls, W., 2006. Soil water characteristic estimates by texture and organic matter for hydrologic solutions. Soil Science Society of America Journal 70, 1569-1578.

Saxton, K., RRawls, W., Romberger, J., Papendick, R., 1986. Estimating generalized soil-water characteristics from texture 1. Soil Science Society of America Journal 50, 1031-1036.

Scherer, T.F., Franzen, D., Cihacek, L., 2017. Soil, water and plant characteristics important to irrigation. North Dakota State University, Fargo, North Dakota.

Schut, A.G., Traore, P.C.S., Blaes, X., Rolf, A., 2018. Assessing yield and fertilizer response in heterogeneous smallholder fields with UAVs and satellites. Field Crops Research 221, 98-107.

Schwarz, M.W., Cowan, W.B., Beatty, J.C., 1987. An experimental comparison of RGB, YIQ, LAB, HSV, and opponent color models. ACM Transactions on Graphics (TOG) 6, 123-158.

Snyder, R., Eching, S., 2002. Penman-Monteith daily (24-hour) reference evapotranspiration equations for estimating ETo, ETr and HS ETo with daily data. Regents of the University of California.

Steduto, P., Hsiao, T.C., Fereres, E., Raes, D., 2012. Crop yield response to water. FAO Rome.

Stępień, M., Samborski, S., Gozdowski, D., Dobers, E.S., Chormański, J., Szatyłowicz, J., 2015. Assessment of soil texture class on agricultural fields using ECa, Amber NDVI, and topographic properties. Journal of Plant Nutrition and Soil Science 178, 523-536.

Sudduth, K.A., Kitchen, N., Bollero, G., Bullock, D., Wiebold, W., 2003. Comparison of electromagnetic induction and direct sensing of soil electrical conductivity. Agronomy Journal 95, 472-482.

Sudduth, K.A., Kitchen, N., Drummond, S., 2017. Inversion of soil electrical conductivity data to estimate layered soil properties. Advances in Animal Biosciences 8, 433-438.

Sudduth, K.A., Kitchen, N.R., Wiebold, W., Batchelor, W., Bollero, G., Bullock, D., Clay, D., Palm, H., Pierce, F., Schuler, R., 2005. Relating apparent electrical conductivity to soil properties across the north-central USA. Computers and Electronics in Agriculture 46, 263-283.

Sui, R., Vories, E., 2020. Comparison of sensor-based and weather-based irrigation scheduling. Applied Engineering in Agriculture, 0.

Thompson, C.N., Guo, W., Sharma, B., Ritchie, G.L., 2019. Using normalized difference red edge index to assess maturity in cotton. Crop Science 59, 2167-2177.

Tremblay, N., Bouroubi, Y.M., Bélec, C., Mullen, R.W., Kitchen, N.R., Thomason, W.E., Ebelhar, S., Mengel, D.B., Raun, W.R., Francis, D.D., 2012. Corn response to nitrogen is influenced by soil texture and weather. Agronomy Journal 104, 1658-1671.

Turner, D., Lucieer, A., Malenovský, Z., King, D.H., Robinson, S.A., 2014. Spatial co-registration of ultra-high resolution visible, multispectral and thermal images acquired with a micro-UAV over Antarctic moss beds. Remote Sensing 6, 4003-4024.

United Nations, U.N., 2019. World population prospects 2019: highlights. Department of Economic and Social Affairs, Population Division.

Van Bussel, L.G., Ewert, F., Zhao, G., Hoffmann, H., Enders, A., Wallach, D., Asseng, S., Baigorria, G.A., Basso, B., Biernath, C., 2016. Spatial sampling of weather data for regional crop yield simulations. Agricultural and Forest Meteorology 220, 101-115.

Virtanen, P., Gommers, R., Oliphant, T.E., Haberland, M., Reddy, T., Cournapeau, D., Burovski, E., Peterson, P., Weckesser, W., Bright, J., 2020. SciPy 1.0: fundamental algorithms for scientific computing in Python. Nature Methods 17, 261-272.

Vories, E., O'Shaughnessy, S., Sudduth, K.A., Evett, S., Andrade, M., Drummond, S., 2020. Comparison of precision and conventional irrigation management of cotton and impact of soil texture. Precision Agriculture, 1-18.

Vos, C., Don, A., Prietz, R., Heidkamp, A., Freibauer, A., 2016. Field-based soil-texture estimates could replace laboratory analysis. Geoderma 267, 215-219.

Walter, A., Finger, R., Huber, R., Buchmann, N., 2017. Opinion: Smart farming is key to developing sustainable agriculture. Proceedings of the National Academy of Sciences 114, 6148-6150.

Walter, I.A., Allen, R.G., Elliott, R., Jensen, M., Itenfisu, D., Mecham, B., Howell, T., Snyder, R., Brown, P., Echings, S., 2000. ASCE's standardized reference evapotranspiration equation, Watershed management and operations management 2000, pp. 1-11.

Walton, J.T., Nowak, D.J., Greenfield, E.J., 2008. Assessing urban forest canopy cover using airborne or satellite imagery. Arboriculture & Urban Forestry 38, 334-340.

Xin, Y., Tao, F., 2019. Optimizing genotype-environment-management interactions to enhance productivity and eco-efficiency for wheat-maize rotation in the North China Plain. Science of the Total Environment 654, 480-492.

Xue, J., Su, B., 2017. Significant remote sensing vegetation indices: A review of developments and applications. Journal of sensors 2017.

Zhang, L., Zhang, H., Niu, Y., Han, W., 2019. Mapping maize water stress based on UAV multispectral remote sensing. Remote Sensing 11, 605.

Chapter 6. CROP YIELD ESTIMATION BASED ON SOIL, WEATHER AND UAV IMAGES

6.1 Abstract

Crop yield prediction is important for farmers to conduct proper field management and marketing decisions. However current prediction models are usually built on single types of data, e.g. imagery data, soil or weather data, which may not reflect the holistic effect of environment and management on crop development. The goal of this study was to quantify cotton yield variance due to soil texture and weather conditions using the multiple-year unmanned aerial vehicle (UAV) imagery data and deep learning techniques. Eleven soil features were extracted using the collected apparent soil electrical conductivity (EC_a) to describe soil variation over the field. A soil convolutional neural network (CNN) was developed to process the soil features. In addition, six weather parameters were also processed by a weather CNN. A gated recurrent unit (GRU) network was used to quantify cotton yield variation due to soil and weather features by integrating UAV-based image features (e.g., NDVI) variance in different months. Results show that each one of the three years' cotton yield could be predicted using the model trained with data of the other two years with prediction errors of MAE = 247 (8.9%) to 384 kg ha^{-1} (13.7%), which showed that quantified yield variance based on soil texture, weather conditions and UAV imagery for a future year was feasible.

Keyword: Yield prediction, soil CNN, weather CNN, multispectral imagery, gated recurrent unit network

6.2 Introduction

Soil and weather conditions are important factors to quantify crop development and yield. Soil texture, defined as different percentages of sand, clay and silt content in a soil group, affects the water holding capacity and had effects on crop development and yield (Scherer et al., 2017; Tremblay et al., 2012). Forcella et al. (2000) reported that soil texture and soil water content affected seedling emergence date and emergence rate. Soil texture and soil water content also had effects on root development (Oosterhuis, 1990). Many studies found out that soil texture had relationships with the yield of cotton (Vories et al., 2020), corn (Kitchen et al., 2003; Kitchen et al., 2005) and soybean (Jiang and Thelen, 2004; Kitchen et al., 2005). Weather conditions of temperature, precipitation and solar radiation had been shown to be important effects for yield variability of maize and winter wheat between years (Ceglar et al., 2016). Addy et al. (2020) showed that the functional response of crop yield to nitrogen application rate varied under different weather conditions between years.

However, the combined effects of soil and weather on crops are complicated. Crops showed different levels of weather sensitivity in different regions (Mathieu and Aires, 2018) and different growth stages (Addy et al., 2020; Ceglar et al., 2016). Crop development and yield also showed different dependence on soil under different years' weather conditions (Feng et al., 2021). Studies have developed many crop models from regional to global to quantify crop development and yield based on weather and soil (Van Bussel et al., 2016). The development of those models required more than 10 years of data and generally needed a recalibration when used in other regions (Ceglar et al., 2016). Khaki et al. (2020) and

Khaki and Wang (2019) developed yield prediction models based on weather and soil that can work for different USA states but needed data from 35 years and 9 years, respectively.

Remote sensing technology has been used in recent years to monitor crops to quantify crop development and yield. For example, satellites images were used for yield prediction (Schut et al., 2018; You et al., 2017) , evaluating metal-induced stress on crops development (Liu et al., 2018), and quantifying chlorophyll concentration in vegetation (Singhal et al., 2018). Site-specific monitoring instead of the region and state-level monitoring is more meaningful for farmers, and unmanned aerial vehicle (UAV)-based images were used to evaluate field-scale crop emergence (Chen et al., 2018; Feng et al., 2020a), crop water stress (Bian et al., 2019), crop growth status (Du and Noguchi, 2017) and yield (Feng et al., 2019; Feng et al., 2020b). Many studies that worked with UAV images to quantify crop growth and yield focused on images (including training and testing sets) collected within one year (Maimaitijiang et al., 2020; Yang et al., 2019; Zhang et al., 2020). Models built using one year's data were difficult to apply in a future year to guide field management. Evaluation of yield in a future year before harvest is meaningful for farmers, which required models that have good predictions performance in an additional year that included data not used in the model training procedure. There were studies working on this (Chu and Yu, 2020; Khaki and Wang, 2019; Khaki et al., 2020; Schwalbert et al., 2020) but none of them works with UAV images.

Combining soil texture, weather conditions and UAV images together would be promising to quantify crop growth and yield in a future year. This study aimed to establish a method for yield estimation based on soil texture, weather conditions and UAV imagery collected in three different years where soil texture did not change much (2017-2019). The

specific objectives were: 1) developing data fusion methods for spatiotemporal soil data, weather data and UAV image data; 2) developing a deep learning model to predict yield for different years.

6.3 UAV image processing

Images collected in all three years were processed using Agisoft PhotoScan Pro (Version 1.2.2, Agisoft, Russia) to generate orthomosaic images. The GPS locations of the GRPs were used for the GPS calibration of the orthomosaic images. Each cotton row was identified from the orthomosaic images using the method developed in a previous study (Feng et al., 2019). NDVI was calculated in the orthomosaic images and soil background was removed based on a threshold of NDVI < 0.5. There were 152 (or 148 in 2018) cotton rows and the field was about 320 m in the south-north direction, therefore 152 (or 148) × 315 rectangles with ~1.0 m^2 each were segmented (the north and south edges of the field were removed to avoid edge effects) and the mean NDVI in each rectangle were extracted as image data points following by the procedure written in Feng et al. (2021). Then, the data points were downsampled to 38 (or 37) × 63 data points by averaging the NDVI in a sample area of 4 m (match the four-row harvested yield data) × 5 m (got the integer from 315/5 instead of non-integer from 315/4). The GPS of the center of each sample area was extracted from the geo-referenced orthomosaic images. To register the data collected in different years, data points of soil EC_a and yield and were firstly interpolated with Kriging, and then the 4 m × 5 m sample areas were cropped from the Kriging maps of yield and soil EC_a to align with those NDVI areas in different years.

6.4 Soil and weather features processing

Sand content percentage (sand%) and clay content percentage (clay%) in the average 34 cm and clay content percentage in seven different depths from 10 cm to 70 cm (defined as clay10 - clay70) were calibrated based on EC_a and the soil sample lab analysis following the data processing procedure described in Chapter 4. Field capacity (*FC*), wilting point (*WP*) and total available water (*TAW*) were calculated based on the sand% and clay% (Saxton and Rawls, 2006; Saxton et al., 1986). Those soil features could be used directly as inputs in machine learning models for crop development and yield estimation as described in Chapter 4. However, Khaki et al. (2020) and Chapter 4 pointed out that there were dependencies (relationships) of the soil features measured at different depths. For example, the clay10 – clay70 features showed high Pearson correlation coefficients between their neighborhood layers (as described in Chapter 4). A soil convolutional neural network (S_CNN) was developed to capture the dependencies of soil data measured at different depths using two convolution layers (Figure 5.1). The convolutional neural networks are able to scan the clay content in every two-neighbor layer to extract the spatial features. The first convolution layer consisted of four kernels (Khaki et al., 2020) to extract information in each two neighborhood depth layers. Each kernel (marks as color dot in Figure 5.1) was designed as $\sum_{i=1}^{n} \boldsymbol{w_i} \times \boldsymbol{x_i}$ where x_i were the inputs of clay1 - clay7 and the w_i were the weights. Different kernels with different w_i defined different relationships or data transforms between the neighborhood depth layers. The numbers of kernels were designed based on the numbers of soil features and the amount of soil data points. If the number of kernels is too small, it would not have enough fitting ability to extract the information between the soil features; however, if the number of kernels is too large, it may

cause over-fitting problems. In this paper, there were seven input features (clay10 - clay70) and the number of kernels in the first layer of the S_CNN were four, which was about the half of the number of input features. Followed was an average pooling layer that conducted an average process on the outputs of the first convolution layer. The second convolution layer conducted similar process as the first convolution layer but with eight kernels, which was the twice of the first convolution layer, followed by an average pooling layer to generate features with 1 × 8 dimensions. The S_CNN extracted the most significant and independent parameters from the seven soil features (clay10 - clay70) that included the clay content in different depth layers as well as their relationship between layers. In addition, four soil features of sand% (clay% were removed since linear calibration were used based on the same EC_a data with the sand%), FC, WP and TAW were transformed using a fully connected layer to reduce collinearity since high Pearson correlation coefficients were found between these four soil features (Chapter 4). The fully connected layer conducted another mathematical operation of $\sum_{i=1}^{n} \boldsymbol{w_i} \times \boldsymbol{x_i}$ where xi were inputs of *FC*, *WP*, *TAW* and sand%.

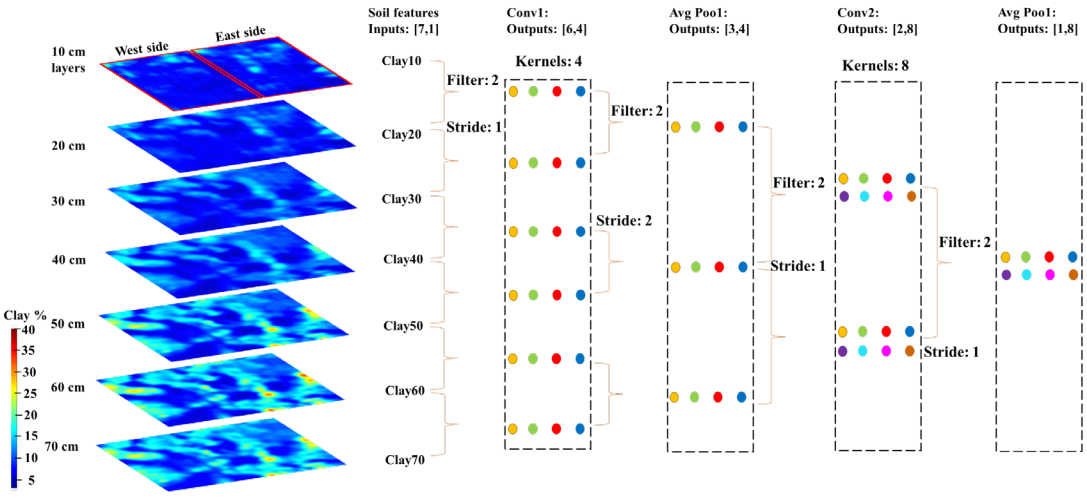

Figure 6.1: S_CNN. Soil clay content percentage from different depth were processed using a network with two convolution layers. Each color dot was a mathematical operation result of $\sum_{i=1}^{2} \boldsymbol{w_i} \times \boldsymbol{x_i}$ where xi were the clay content percentage of each layer and the w_i were the weights obtained by training from the data set provided.

Weekly weather data was used in this study instead of daily weather (large amount of data and was shown not necessary in (Khaki and Wang, 2019) and (Khaki et al., 2020)) data and monthly weather data (less amount of data and may not enough to reflect the weather effects on crop development), which included accumulative input water (precipitation and irrigation), maximum and minimum air temperature, total solar radiation, vapor pressure and evapotranspiration of reference crop (Allen et al., 1998) from May 1 to Oct. 29 in each year of 2017 to 2019. In the experimental area, cotton is preferred to plant in late May or early June, and they develop in the months of Jul., Aug. and Sep., and harvest in Oct (Goodell et al., 2015). UAV images were collected in Jul., Aug. and Sep. to monitor cotton development. Weather data were divided into four periods to match with the imagery data periods, i.e., the first 13 weeks after planting (May 1 to Jul. 30, Period 1) to match with the UAV image collected in Jul., week 14 to week 18 (Jul. 31 to Sep. 3, Period 2) to match with the UAV image collected in Aug., week 19-week 22 (Sep. 4 to Oct. 1, Period 3) to match with the UAV image collected in Sep. and week 23 to week 26 (Oct. 2 to Oct. 29, Period 4) to represent the period that between the last image collection and harvest.

Weather data have temporal dependencies. For example, some weather prediction models such as the Markov chain (Khiatani and Ghose, 2017) assumed that temperature would reduce and vapor pressure would increase dependently if rain, and if last week was

in high temperature, this week may have a low possibility of low temperature. A weather convolutional neural network (W_CNN) was designed to extract the relationships among the six weekly weather parameters and the temporal relationships (dependencies) of the weekly weather parameters in the sequential weeks. Two convolution layers were designed with four filters in each layer (color boxes in Figure 5.2). Similar to the S_CNN, a moving window scans every three weekly weather from the first week to the 26th week after planting using kernels that provided various relationships (non-linear fit) between weekly weather parameters. The output features from the W_CNN were 1×12 matrixes with fused information of both relationship information between six weather parameters and sequential weeks.

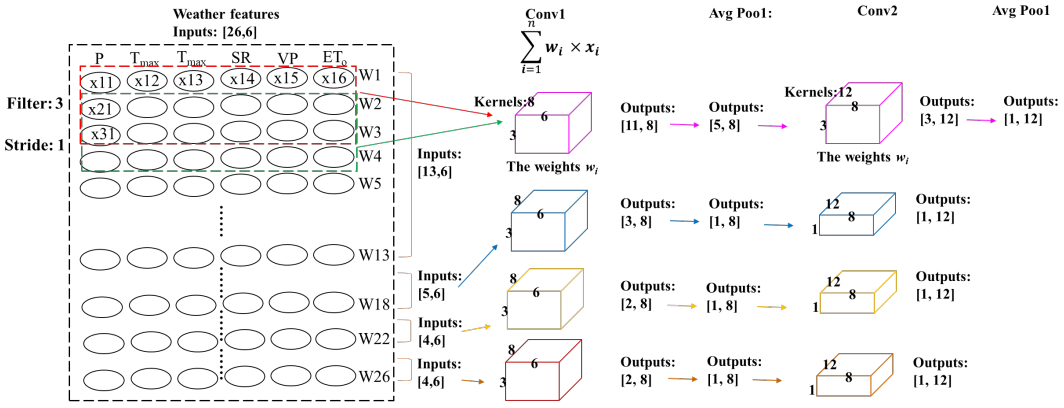

Figure 6.2: The illustration of the developed W_CNN. Weekly weather data from May 1 to Oct. 29 were used. The first 13 weeks related to date from May 1 to Jul. 30, week14-week18 related to date from Jul. 31 to Sep. 3, week19-week22 related to date from Sep. 4 to Oct. 1 and week 23 to week 26 related to date from Oct. 2 to Oct. 29. The meanings of the abbreviations of the weather features are: P- total precipitation (irrigation data was included), T_{max}- max air temperature, T_{min}- min air temperature, SR- total solar radiation,

VP- vapor pressure, and ET_o- evapotranspiration for reference crop. W1-W26 mean week1-week26 after planting.

6.5 Yield estimation model

A recurrent neural network (RNN) is a type of neural networks that are designed to process a sequence of variables (e.g., a temporal sequence) by modelling the relationship between the current state of a variable and the previous states (recurrent) in the sequence. It has been used to handle sequential data such as weather data and time series image data (Lipton et al., 2015). Improved RNN models, such as Long Short-Term Memory networks (LSTMs) or Gated Recurrent Units (GRU), enable training on long sequences, overcoming problems like vanishing gradients (Lee et al., 2020). Chung et al. (2014) showed that the GRU and LSTM almost had similar performance on serval sequence prediction tasks, however, GRU has fewer model parameters and easier to optimize.

In this study, a GRU-based RNN (Chung et al., 2014) was used to quantify cotton yield based on soil, weather condition and imagery data. The GRU continuously accepts inputs from a sequence and outputs the information that describes the data transform (or the weighted combination results) of the previous inputs and the current inputs. To easily understand the loop operation in the GUR, the GRU was drawn with the unfolded way (Chen et al., 2019) in this paper, as shown in Figure 5.3a. The GRU includes a reset gate (Eq. 5.1) and an update gate (Eq. 5.2) to control how much information through the sequence needed to be forgotten and memorized. Then a candidate hidden layer $\tilde{h}_t$ was calculated based on the r_t, x_t and h_{t-1} to carry the information remained after the process of the reset gate (Eq. 5.3). If the reset gate r_t were close to 0, all the information h_{t-1} from

the previous sequence would not carry and passed (or memorized) to the later process of the sequence. The final hidden output calculates the ratio (the updated gate z_t) of previous inputs information h_{t-1} updated to information after the reset process $\tilde{h}_t$ to calculate the information that should be passed to the later process of the sequence (Eq. 5.4). If z_t were close to 1, only the information from previous layers h_{t-1} and none of the current input x_t would be used as the input to the later process of the sequence.

$$r_t = \sigma(W_r x_t + U_r h_{t-1}) \tag{5.1}$$

$$z_t = \sigma(W_z x_t + U_z h_{t-1}) \tag{5.2}$$

$$\tilde{h}_t = tanh(W x_t + r_t * U h_{t-1}) \tag{5.3}$$

$$h_t = (1 - z_t) * \tilde{h}_t + z_t * h_{t-1} \tag{5.4}$$

where, r_t, z_t and $\tilde{h}_t$ are the reset gate, update gate and candidate hidden layer; h_t is the hidden layer with the information passed to the next layer; x_t is the current input of a sequence for the GRU and h_{t-1} is the information from the last layer; W_r, W_z, W, U_r, U_z and U are parameters to be trained from the training data set; and σ is the sigmoid function and * is the Hadamard product.

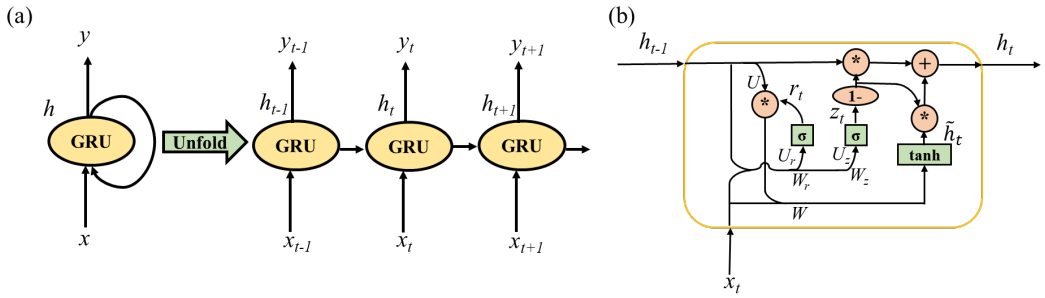

Figure 6.3: The explanation of GRU. (a) GRU continuously accepts inputs from a sequence. To easily understand the loop operation in the GUR, the GRU was drawn with

the unfolded way in this paper. The ‘t’ represented each time step. (b) The architecture of GRU related to Eq. 5.1-5.44.

The architecture of the GRU-based RNN is shown in Figure 5. 4 that included four layers, i.e., S_CNN, W_CNN, GRU layers for NDVI prediction (‘GRU’ in Figure 5. 4) and the fully connected layers for yield prediction (‘FCL2’ in Figure 5. 4). The input parameters of the GRU network included the 11 soil features processed by the S_CNN and weather data from May 1 to Jul. 30 processed by the W_CNN. The initially hidden input vector (‘Init’ in Figure 5. 4) of the GRU was set as zeros and the corresponding output was assumed to be the NDVI in July (the GRU output of its first loop). The hidden outputs of the July GRU would be passed to the next loop of the GRU unit (i.e. the Aug. GRU). The processed weather data from Jul. 31 to Sep. 3 would be passed to the Aug. GRU and its output was assumed to be the NDVI in Aug. The NDVI in Jul. would be used to replace the ‘Init’ to input to the Aug. GRU. Similar procedures were conducted to the GRU of Sep. and yield. The GRU unit was a loop processing unit that continued to accept the three-month weather data and the previous month’s NDVI images. The GRU can predict the NDVI distribution of the current month based on the current month’s weather and the previous month’s NDVI.

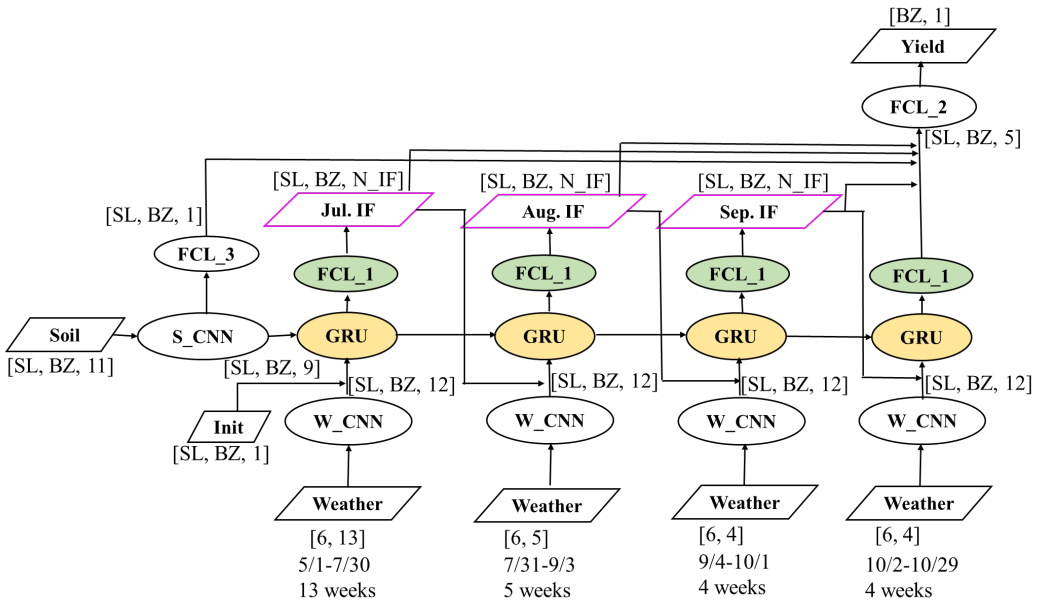

Figure 6.4: The architecture of the GRU network. SL means sequence length, which was set as 1 in this study. BZ is the batch size for the training procedure. FCL means fully connected layer, which conducted another mathematical operation of $\sum_{i=1}^{n} \boldsymbol{w_i} \times \boldsymbol{x_i}$. The yellow GRU was the same loop processing unit in the network and has the same parameters, as well as all the green FCL_1 unit.

Although the GRU has the memory of short-term information and can pass the condensed information to the next timestamp, there is still information loss and not all information that is able to be used after the previous process of the GRU. Therefore, the processed soil features that were important to the yield prediction were directly connected to the fully connected yield prediction layer ('FCL_2' in Figure 5. 4) to avoid information loss through the whole GRU process. These processed soil features would combine with the final output of the GRU and the NDVI in Jul., Aug. and Sep. together to have the final yield prediction after the FCL_2 layer. The NDVI values from images and yield were used as the true labels to train the overall network and the loss function was defined in Eq. 5.5:

$$L = |\hat{y} - y| + \left|\widehat{N_J} - N_J\right| + \left|\widehat{N_A} - N_A\right| + \left|\widehat{N_S} - N_S\right| \quad (5.5)$$

where, L is the loss, $\hat{y}$ is the predicted yield (normalized values), y is the true yield (normalized values), $\widehat{N_J}$, $\widehat{N_A}$ and $\widehat{N_S}$ are the predicted NDVI of the Jul., Aug. and Sep. respectively, and N_J, N_A and N_S are the true NDVI of the Jul., Aug. and Sep.

However, the selected deep learning network is a long training network and some information cannot be passed to the subsequent layers, which makes it hard to train using the overall ground true corresponded with the global loss function. Therefore, a Teacher Forcing (TF) technology (Williams and Zipser, 1989) was conducted to improve the parameter optimizing, which used the NDVI of Jul., Aug. and Sep. from the imagery data to train the individual month's GRU. To avoid yield overfitting of the image NDVI, the TF conducts with a given possibility (for example, 0.5-0.9; TF=1 means true NDVI will always be used, while TF=0 means the predicted NDVI will always be used) in the training procedure, which means the model had the possibility to learn yield variability from the soil, weather and the predicted NDVI (instead of relying the most on the collected image data and ignoring the soil and weather features). Image NDVI (not predicted NDVI) would always be used in the testing procedure.

The best hyperparameters of the learning rate, training batch size, momentum of the stochastic gradient descent (SGD) optimizer and the TF possibility were obtained by the Bayesian optimization procedure with an open-source constrained global optimization tool (Nogueira, 2014). All input data of the model were normalized using Eq. 5.6 before they were used in the model.

$$N_x = \frac{x-m}{std} \quad (5.6)$$

where N_x is the normalized value, m and std are the mean and standard deviation of the training set, and x is the original data.

There are five important components in the GRU-based RNN network, including the direct connection between processed soil and the yield fully connected layer (FCL_2 in Figure 5. 4), S_CNN, W_CNN, GRU and NDVI images. To test the importance of each component on the GRU-based RNN, different models without (WO_) one of each component were tested, as shown in Table 5.1. Firstly, the components of NDVI would be removed from the original model from the test procedure and then from the training procedure by setting the TF to 0 (WO_TF_Test and WO_TF_Train in Table 5.1). S_CNN would be removed and used a fully connected layer instead to process the raw soil features (WO_S_CNN in Table 5.1). W_CNN would be removed and used the average weekly weather as the inputs instead (WO_W_CNN in Table 5.1). The direct connection between soil and the FCL_2 would be removed in WO_S2Y in Table 5.1. All the data used in the original GRU-based RNN network would be used in the above five models. However, when GRU units were removed, an ensemble module XGBoost (Chen and Guestrin, 2016) was used to replace the GRU for yield prediction and due to the requirement of fix dimension for the inputs of XGBoost, only August NDVI, soil and weather would be used in the WO _GRU as there were some missing image data in July and September in 2017 and 2019. WO_GRU_NDVI would remove the GRU and NDVI in the original model, while WO_GRU_NDVI_W would only predict the yield by soil data and the XGBoost.

Table 6.1: Yield prediction models with the removal of the five important components

Models	Description

WO_TF_Test	Set teacher forcing as 0 in the test procedure, which meant that the true NDVI would not be used as the input of the GRU. The overall model relied on soil, weather and the predicted NDVI. This aimed to test the importance of the UAV NDVI images for yield prediction.
WO_TF_Train	Set teacher forcing as 0 in both train and test procedure. There was only yield data and no image data to guide the model to optimize the GRU parameters in the training procedure. This aimed to test the importance of the UAV NDVI images in the training procedure for the parameter optimization guide.
WO_S_CNN	Remove the S_CNN and use a fully connected layer instead. This aimed to test the importance of the S_CNN.
WO_W_CNN	Remove the W_CNN and instead use the mean weather parameters as the input. This aimed to test the importance of the W_CNN.
WO_S2Y	Remove the connection between the processed soil features and the FC_2 layer. This aimed to test if soil information would be lost through the whole GRU procedure.
WO _GRU	Use an XGBoost model instead of a GRU model and the inputs of soil features, mean weather parameters and NDVI images for yield prediction. This aimed to test the importance of the GRU unit. Only soil, weather and August NDVI would be used.
WO_GRU_NDVI	Use an XGBoost model and the inputs of soil features and mean weather parameters for yield prediction. This aimed to test the importance of the UAV NDVI images.
WO_GRU_NDVI_W	Use an XGBoost model and only soil features for yield prediction. This aimed to test the importance of the UAV NDVI images and the weather data.

6.6 Yield prediction accuracy

6.6.1 Correlation between yield with soil features and image features

Pearson correlation coefficients (*r*) between yield with soil features are shown in Table 5.2. As can be seen in Table 5.2, the correlation between yield and soil features in each year was about 0.5-0.7, except for the topsoil clay10 and clay20 that had a lower correlation. Cotton yields in all three years had a higher correlation with clay content in the depth between 40 – 70 cm, i.e., clay40 – lay70 than those in shallower layers, which may be due to the less water content in the shallow soil and higher water-use effeteness of deeper roots (Djaman and Irmak, 2012). The *r* in clay40 -clay70 with yield is very close to each other as the *r* between clay40 – clay 70 were over 0.92 (Chapter 5.6.2). Table 5.2 also

shows that the soil features derived from soil texture, including sand% in the top 0-34 cm, WP, FC and TAW were about 0.5 and did not show strong correlations with yield.

Table 6.2: Pearson correlation coefficients (*r*) between yield and soil features.

Yield	sand%	clay10	clay20	clay30	clay40	clay50	clay60	clay70	WP	FC	TAW
2017E§	-0.45	0.2	0.37	0.5	0.52	0.51	0.51	0.51	0.49	0.49	0.48
2018W	-0.51	0.27	0.46	0.56	0.58	0.58	0.57	0.58	0.57	0.55	0.52
2019E	-0.55	0.23	0.46	0.64	0.67	0.69	0.69	0.69	0.58	0.57	0.55
2019W	-0.5	0.19	0.42	0.58	0.61	0.63	0.63	0.64	0.59	0.55	0.53

§: 'W' represents the west side of the field, while 'E' represents the east side of the field.

Soil features did not explain all the variability of the yield in the three years in this study. As shown in Figure 5.5, histograms of the cotton yield of the same fields, whose soil texture had not had substantial changes in the three years, showed different distribution in 2017-2019. In addition, Figure 5.6 shows the fitness of the cotton yield in each same position at different years, i.e., data points in 2017E vs. 2019E, and 2018W vs. 2019W, as well as the average yield in different sand% groups of these three years. The variance of cotton yield was MAE = 627 kg ha^{-1} (equivalent 27.0% to the Yield2017E) between the year 2017 and 2019 in the east field, and MAE = 662 kg ha^{-1} (equivalent 20.0% to the Yield2018W) between the year 2018 and 2019 in the west field. Yield variation between years in the same positions (assumed same soil texture) may be due to the different weather conditions and field management (irrigation in this case).

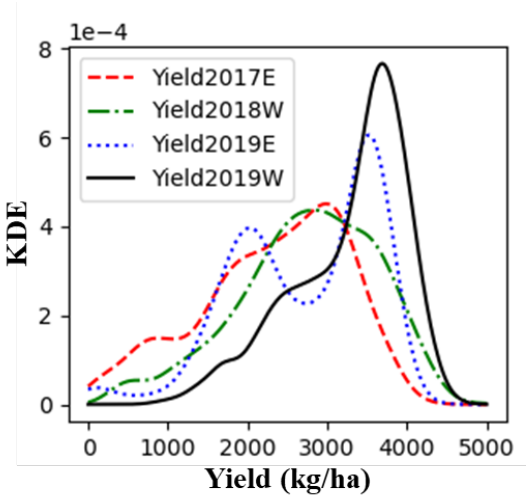

Figure 6.5: Yield data distributions in 2017E, 2018W, 2019E and 2019W. KDE: kernel density estimation.

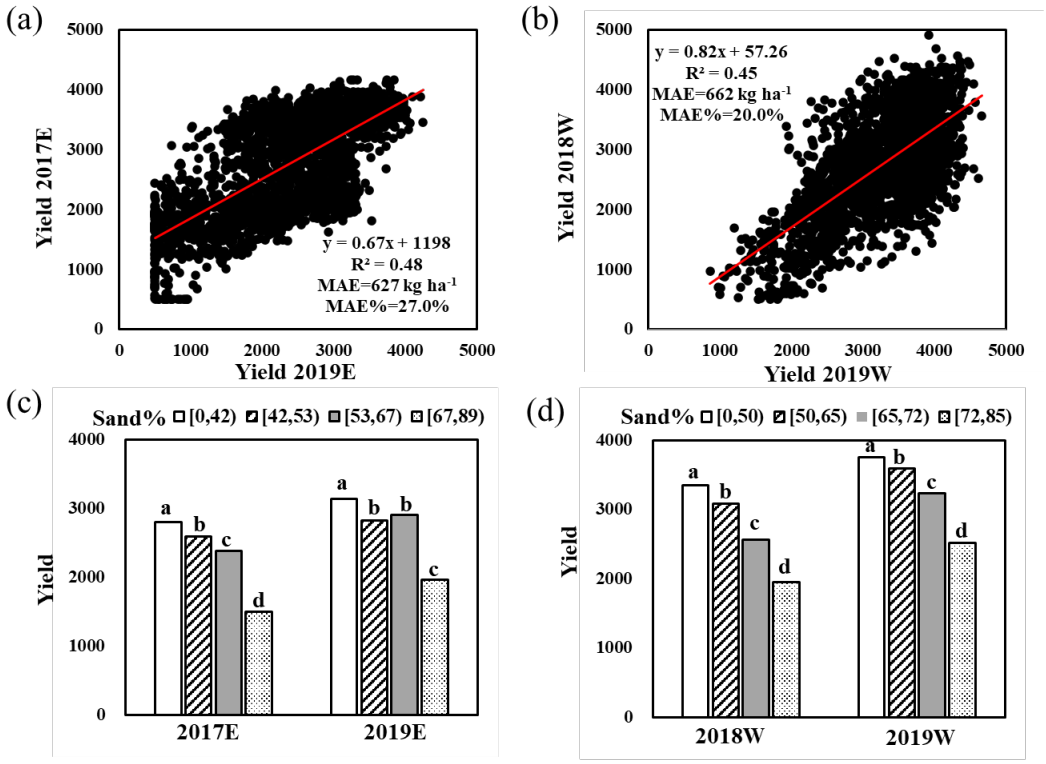

Figure 6.6: Yield comparison of different years in the same positions as well as the average yield in different sand% groups of these three years. (a) Comparing the yield in 2017 and 2019 in the east side of the field; (b) comparing the yield in 2018 and 2019 in

the west side of the field; (c) yield difference between 2017E and 2019E in different sand% groups; (d) yield difference between 2018W and 2019W in different sand% groups. Different lower-case letters indicate a significant difference at the 5% level of Tukey's Honest significant difference test with 'a' the largest mean yield and 'd' the smallest mean yield.

NDVI in August of 2017E and 2019E was highly correlated to yield, as shown in Table 5.3. The correlation between NDVI and yield in Aug. and July of the 2018W were close (i.e., 0.65 and 0.69). Figure 5.7 shows the relationships between NDVI and yield in different years in the east side of the field, where the soil texture was considered the same within two years. The relationship between NDVI and yield was quadratic in 2019 but a linear relationship in 2017. If predicting the yield in 2019 only based on image NDVI collected in 2019 and the linear function fitted using NDVI and yield data collected in 2017, R^2=0.31 was obtained. The NDVI collected in 2019 may face the saturation problem though the 16-bit multispectral camera was used. Even though there was no difference in quadratic and linear relationships, coefficients of the formula may still be different in a different year. The NDVI had a high correlation with yield in 2017 and 2019, but predicting yield in different years only based on a model build with the previous year's image NDVI and yield may not be accurate.

Table 6.3: Pearson correlation coefficients (*r*) between yield and image NDVI respectively

Yield	Jul. NDVI	Aug. NDVI	Sep. NDVI
2017E	--	0.81	--
2018W	0.69	0.65	0.12
2019E	0.6	0.9	0.79

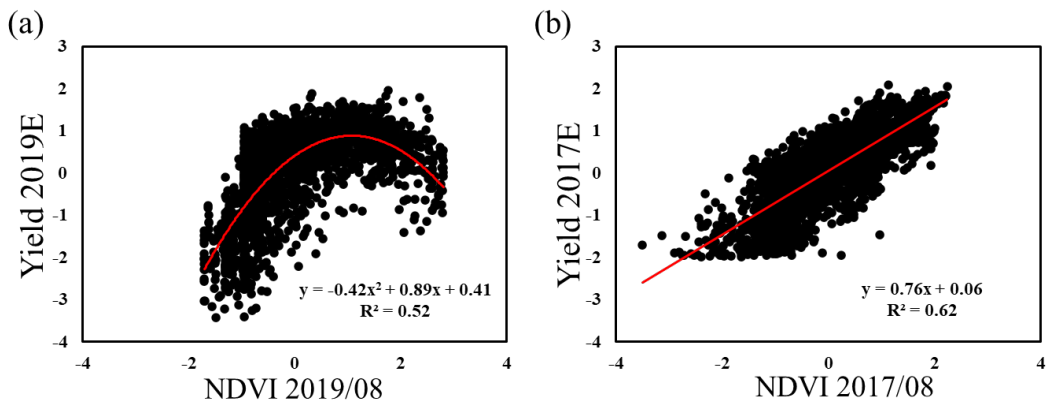

Figure 6.7: Relationships between NDVI and yield in different years: (a) quadratic relationship between NDVI collected in Aug. 2019 and yield in 2019; (b) relationship between NDVI collected in Aug. 2017 with yield was more likely be a linear relationship. To avoid the effects of different multispectral sensors, all the NDVI and yield were normalized as (x-mean)/std.

In summary, the low correlation between soil features with yield (Table 5.3 and Figure 5.6) and the unstable relationship between NDVI and yield in different yield (Figure 5.7) show that combining soil, weather and NDVI together for yield prediction in a different year is necessary.

6.6.2 Yield prediction based on soil, weather and UAV images

Four tests were conducted with each selected one of the years' data as the testing set and the others as the training set to evaluate the performance of the proposed model structure for yield prediction in an additional year. Soil features, weather conditions and image data of the training set were used as the inputs and the true yield data of the training set were used as the targets to train the GRU-based RNN network. After model training, soil features, weather conditions and image data of the testing set were used as the inputs for the trained model to predict the yield of the testing year and compared with the true

yield in the testing set. There were 38*63= 2394 data points per year. If used two years of data for training, there would be 2394*2=4788, and the other year for testing is 2394. We had 4788+2934=7722 in total for each one test in Figure 5.8. In Figure 5.8a, the model was trained using the soil, weather and NDVI images in Jul. Aug. and Sep. of 2018W and 2019E, and predicted the yield of 2017E with the inputs of soil, weather and the NDVI in Jul. 2017. Figure 5.8b shows the yield prediction result of 2018W with the predictors of soil, weather and NDVI of 2018W and the model trained with soil, weather and NDVI of 2019E and 2017E. MAE=345 kg ha^{-1} (12.3%) and R^2=0.72 for 2017E as well as MAE=384 kg ha^{-1} (13.7%) and R^2=0.67 of 2018W were obtained. Figure 5.8c shows the result of 2019E with the predictors of soil, weather and NDVI of 2019E based on the model that trained with soil, weather and NDVI of 2018W and 2017E, while Figure 5.8d shows the yield prediction result of 2019W with the predictors of soil and weather of 2019W but not have NDVI images available in 2019W based on the GRU network trained using the soil, weather and NDVI of 2018W and 2017E. MAE=247 kg ha^{-1} (8.9%) and R^2= for 2019E as well as MAE=355 kg ha^{-1} (10.8%) and R^2=0.60 of 2019W were obtained. Those MAE were lower than the MAE shown in Figure 5.6 (only relied on soil) and R^2 were higher than that in Figure 5.7 (only relied on image NDVI), which indicate that combining soil, weather and image NDVI as the predictors could potentially predict yield using model that training with previous years' soil, weather and NDVI.

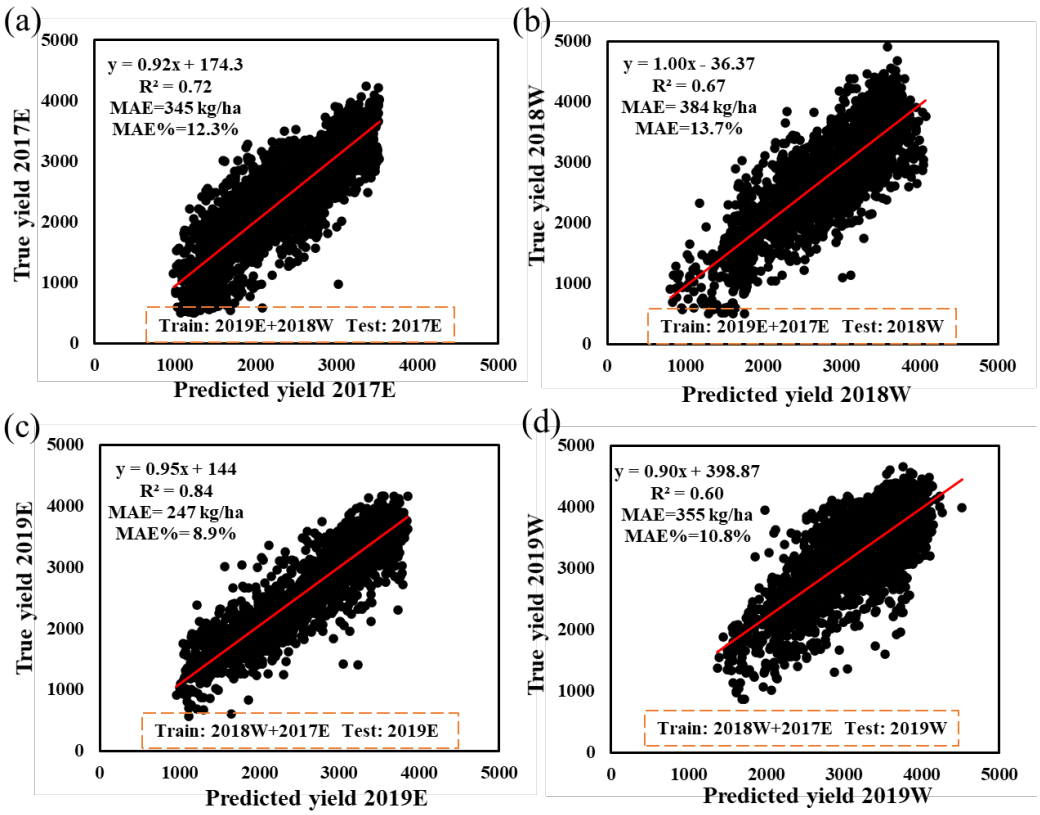

Figure 6.8: Yield prediction results. (a) The data set of 2019E and 2018W were used for training to predict the yield in 2017E; (b) The data set of 2019E, 2019W and 2017E were used for training to predict the yield in 2018W; (c) The data set of 2019W, 2018W and 2017E were used for training to predict the yield in 2019E; (d) The data set of 2019E, 2018W and 2017E were used for training to predict the yield in 2019W. Note, no image NDVI was available in 2019W and the result in (d) is equal to the result of WO_TF_test.

The prediction results in Figure 5.8 that obtained from the proposed model can be used as a reference to compare with the models that excluded each of the components of S_CNN, W_CNN, a direct connection between soil and FCL_2 layer, GRU unit and image NDVI (set by changing the TF) (Table 5.1), as shown in Figure 5.9. Overall, models removing those components had higher MAE and lower R^2 compared with the original model. It is worth noting that the removal of W_CNN obtained the worst performance

(about 150-250 kg ha^{-1} MAE increased compared to the original model) in all the years' yield prediction. There was about 150-220 kg ha^{-1} MAE increased of the WO_TF_Test and WO_TF_Train models compared to the original model, which indicated that NDVI played an important role in the yield prediction. The models without S_CNN had about 20-120 kg ha^{-1} MAE increased. The models without connection between the soil features and the FCL_2 layer showed 20-130 kg ha^{-1} MAE increased, indicating that there was some soil information loss through the GRU loop process. There was about 100 kg ha^{-1} MAE increased for the models without GRU units. Removing the NDVI from those XGBoost models showed more performance drop, as well as the weather data. This indicates that NDVI and weather data were important even using a non-time series model.

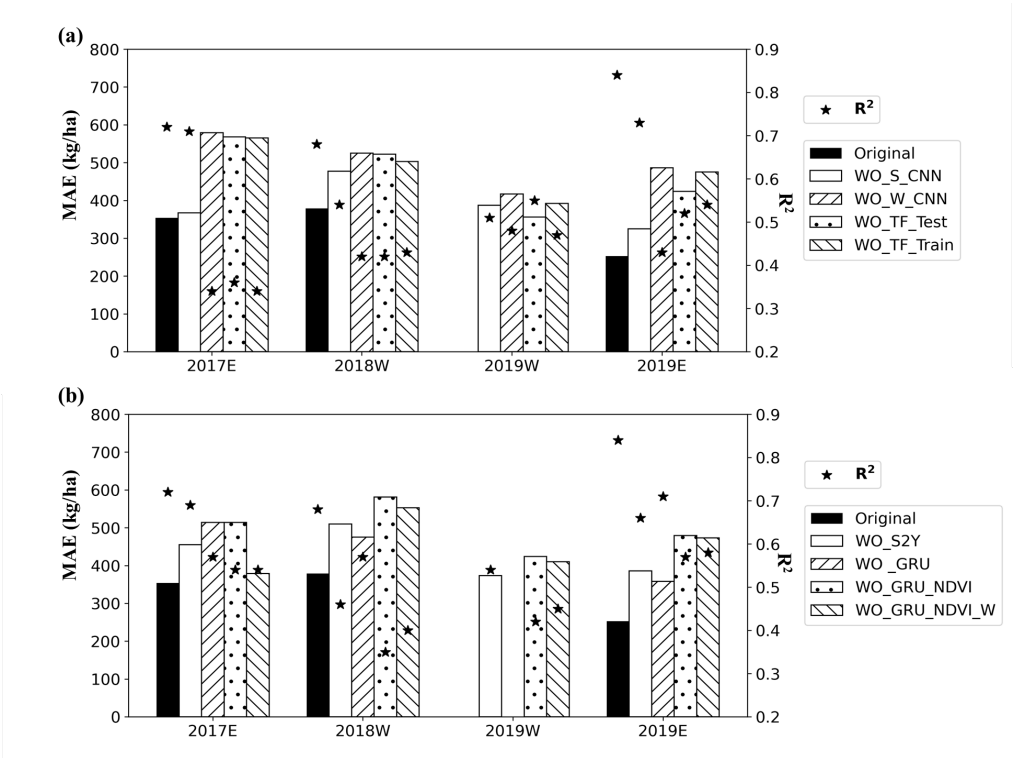

Figure 6.9: Yield prediction performance of models that excluded each of the components of S_CNN, W_CNN, GRU unit, image NDVI and TF described in Table 7. (a) The MAE and R2 of WO_S_CNN, WO_W_CNN, WO_TF_Test and WO_TF_Train; (b)

MAE and R2 of WO_S2Y, WO _GRU, WO_GRU_NDVI and WO_GRU_NDVI_W. Note, no image NDVI was available in 2019W.

Since there were 7 clay input features in the S_CNN, the yield prediction performance of kernel numbers of 2, 4, 8 in the first layer and of 2, 4, 8, 16 in the second layer were compared, as well as the kernel numbers of 4, 8, 16 in the first layer and of 8, 12, 16 in the second layer of the W_CNN. The numbers of kernels changes did not affect the yield prediction performance in 2017E and 2019E too much (about 20-50 kg ha^{-1} MAE increased and 0.01-0.03 R^2 dropped). This may due to the NDVI in 2017E and 2019E had a high correlation with yield and the yield prediction can get information from the NDVI. There were about 30-80 kg ha^{-1} MAE increased and 0.12-0.2 R^2 dropped for the 2018W when kernel numbers changed, which was the one that had the largest effects. There was about 20-60 kg ha^{-1} MAE increased and 0.1 R^2 dropped for the 2019W.

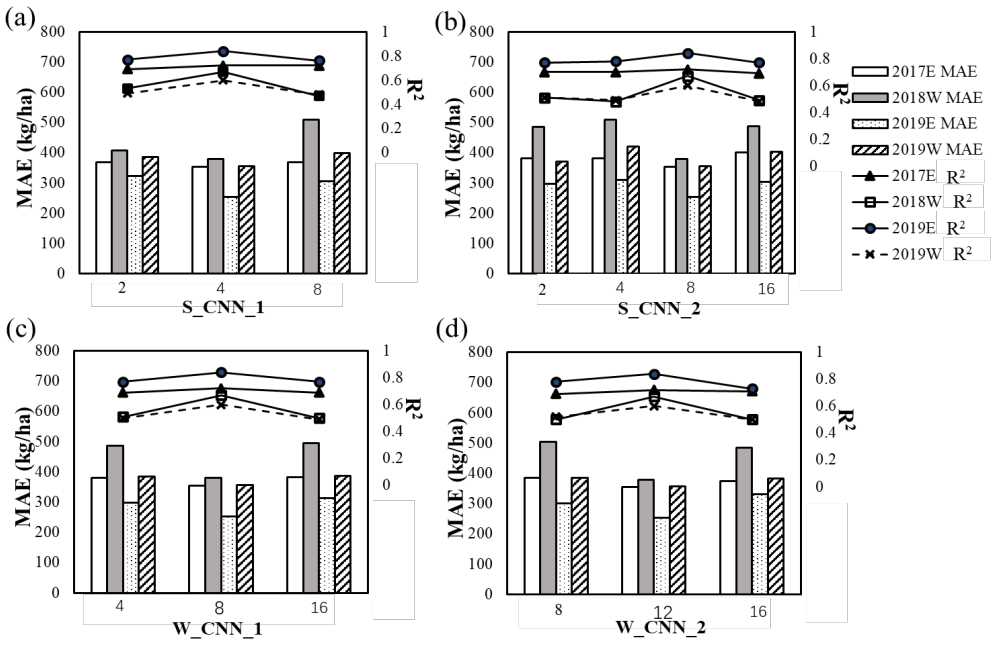

Figure 6.10: Yield prediction performance of models with different kernel numbers in S_CNN and W_CNN.

6.6.3 The crop growth and yield maps

The monthly NDVI can be used to trace the crop development through the growing season. Figure 5.11 shows the NDVI and yield maps of the east field in 2017 and 2019. Only NDVI in Aug. of 2017 was available, and only 2/3 field's NDVI in Sep. 2019 was available due to a camera problem. The predicted NDVI from the GRU network in Jul. and Sep in 2017 and the other 1/3 field's in Sep. 2019 were used as the alternative in Figure 5.11. Tough the soil texture was considered the same between these two years, crop yield distribution shows a difference in some regions. The black circles in the yield maps mark the regions that having more yield in 2019, while the pink circles mark the regions that having more yield in 2017. The predicted yield of 2017E and 2019E captured most of the true yield variance, as well as those yield difference between these two years. Irrigation was applied in late July and in Aug. 2017 in the pink circle region, while there was no irrigation in 2019. NDVI in the pink circle region in July of 2019 was high. The amount of rainfall was small from the middle of July to the late of Aug. in 2019, and the temperature in 2019 in these days was higher than that in 2017 (Figure 2.3). The soil in this pink circle region had about 40%-50% sand content. Those may be the reasons that NDVI were drop in the pink circle region in Aug. and Sep. in 2019. However, the rainfall amount in June and early July in 2019 were higher than that in 2017, and this may be the reason for the high clay content region (the black circles) having a higher yield than that in 2017.

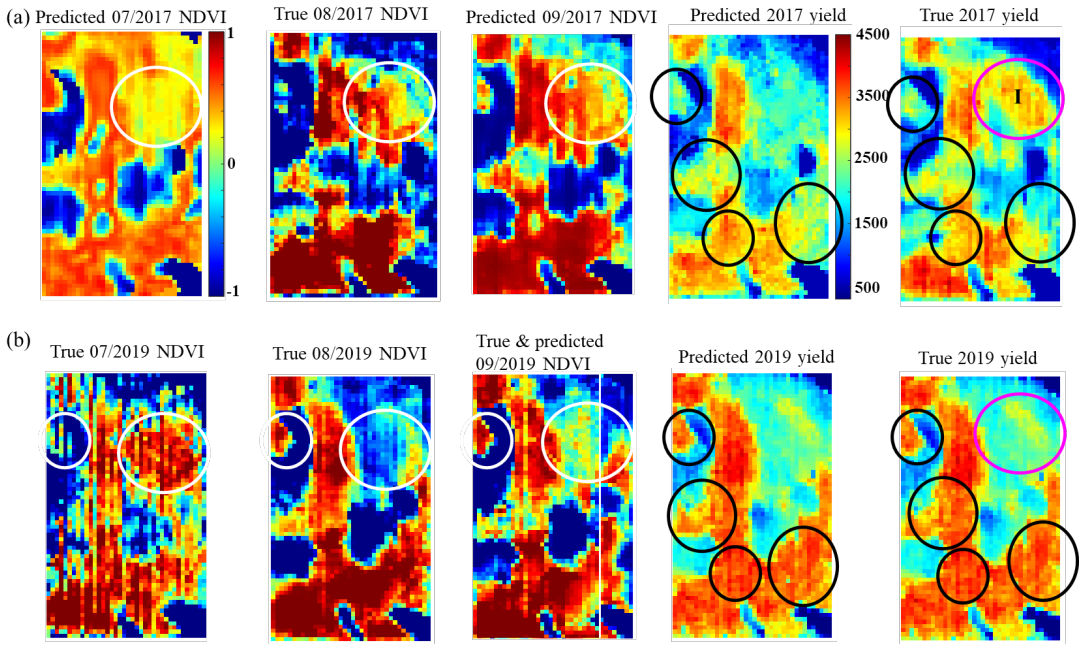

Figure 6.11: The NDVI and yield of (a) 2017E and (b) 2019E. The multispectral camera in Sep. 2019 had some problems and the data of the right side of the field were lost (the NDVI in the right of the white line was the predicted NDVI from the GRU network). The black circles make the regions that had more yield in 2019 while the pink circles mark the regions that had more yield in 2017. The white circles mark the regions of how NDVI changed from July to Sep. of the yield difference regions between 2017 and 2019. All the NDVI were normalized and the absolute values did not have physical meanings. The legend of NDVI was the same in all the NDVI maps. The legend of yield was the same in all the yield maps. I: irrigation applied

The rainfall amount before the middle of Aug. was low in 2018, and this may be the reason that most of the region in 2018 having a lower yield than the same position in 2019, especially in the black circle regions in the yield maps that having 55%-75% sand content. For the year that had higher rainfall amount (i.e., 2019 compared with 2018 and 2017), yield distribution patterns were more similar with the soil texture pattern and the

correlation between yield and soil features were higher (Yield2019E and Yield2019W had the highest Pearson correlation with clay30- clay70, FC, WP and TAW in Table 5.2). There was no NDVI available in 2019W, the predicted NDVI were showing in Figure 5.12, which provided an alternative way to observe the crop growth changes during the season.

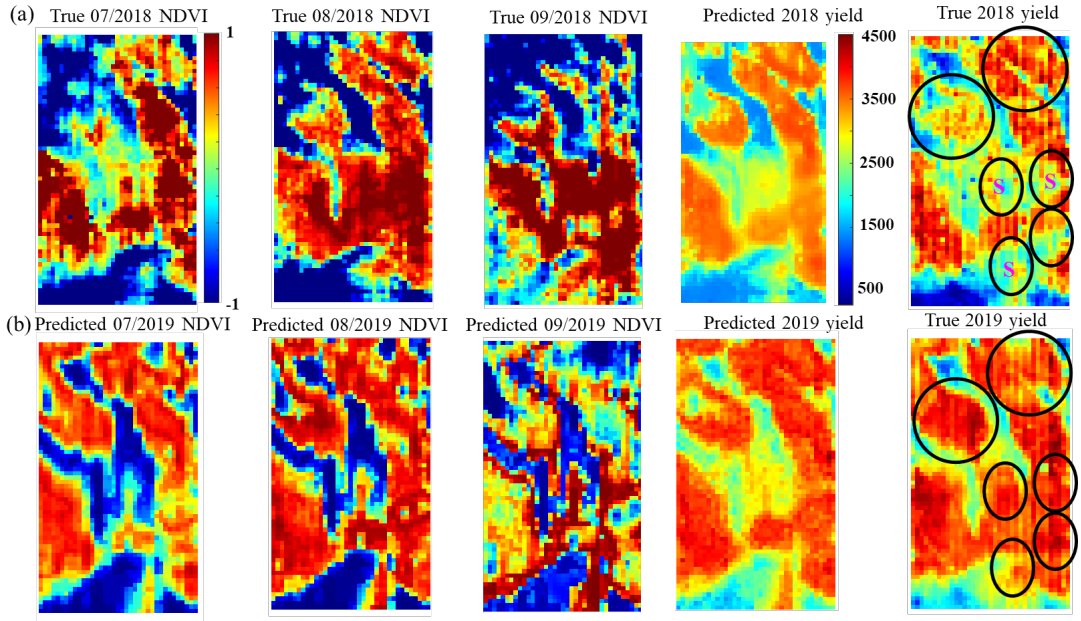

Figure 6.12: The NDVI and yield of (a)2018W and (b) 2019W. The black circles make the regions that having more yield in 2019 than in 2018. All the NDVI were normalized and the absolute values did not have physical meanings. The legend of NDVI was the same in all the NDVI maps. The legend of yield was the same in all the yield maps. S: regions with 55%-75% sand content.

6.7 Conclusion

This paper quantified yield variation based on soil texture, weather conditions and UAV imagery collected in three different years of 2017-2019. Eleven soil features (sand content percentage, wilting point, field capacity, total available water, and clay content percentage in 7 different depth layers) and six weekly weather data (total precipitation,

max air temperature, min air temperature, total solar radiation, vapor pressure and evapotranspiration for reference crop) were processed in an S_CNN and a W_CNN. A GRU-based RNN network was trained using the processed soil features and weather features, as well as the UAV image NDVI and yield as ground true labels. Then the trained models were used for yield prediction in an additional year. MAE = 247 (8.9%) to 384 kg ha^{-1} (13.7%) were obtained for yield prediction of 2017-2019. The S_CNN, W_CNN, direct connection between soil with the final yield prediction layer, UAV-based NDVI, weather data and the GRU unit were showed important for the high accuracy yield prediction. Results showed that quantified yield variation based on soil texture, weather conditions and UAV imagery for a future year was feasible.

6.8 Future work

For the crop growth quantification study in Chapter 5.6.5, we tried to answer if the weather data more important to the crop growth or the soil data more important in the year 2018 and 2019 respectively. In this Chapter of the yield prediction study, I haven't figure out this question of how a specific input feature (soil or weather features) affected the final yield variation. One reason is that deep learning models though have high prediction ability but usually work like a 'black box' and have low explanation ability. For my current prediction model, I haven't found out a better way to explain how the input features affect the final yield prediction. Another reason is that I had a limited data set. I only had three years of data from 2017-2019. The current model had the function for crop growth prediction monthly. But the growth prediction currently did not have high accuracy. Even though we collected image data in the middle of each month, the crop growth stage at the same time of different yield was different due to the weather variation. I did not have higher

temporal resolution image data now. I may need more data especially more high temporal image data to track the crop growth to answer this question. Also, collecting the image data before or after irrigation is a good way to understand the soil and water effects on crop development.

In this Chapter, previous years' data were used for model training. When predicted a future year, all the data for the future year such as soil, weather and image data were used. The cut-off date of the image data was the date we collected images. The cut-off date of the weather data was the end of October. It may be better to use part of the weather data such as weather data up to August or September rather than using all the weather data in the whole growth season since farmers would like to know the yield earlier than waiting for the whole growth season at the harvest time. There are publications (Khaki and Wang, 2019; Khaki et al., 2020) that working for a future yield prediction, and they added the weather prediction function in their models. Future weather prediction or other methods are needed if not the whole growth season weather data are included in the yield prediction model.

I mixed the west field east field and different years in the four tests because of the limited amount of the data set. For example, in the west field, I only had two years' data, 2018 and 2019, and therefore I cannot have more than one year's data for training as I need an additional year's data for testing. The same situation happened to the east field, I only had two years' data 2017 and 2019. If more data will be collected in the future, separating the field for different years' tests (such as using the left half of the west field data of 2018-2019 for training and using the right half of the west field data of 2020 for testing) is a good way to try.

Weekly weather data was used instead of daily weather (large amount of data and was shown not necessary in (Khaki and Wang, 2019) and (Khaki et al., 2020)) data and monthly weather data (less amount of data and may not enough to reflect the weather effects on crop development). However, a test to tell is which is the best to use (daily weather data or weekly weather data or monthly weather data) for yield prediction is worth conducting.

I tried to use the cotton boll as one of the image data for yield prediction before. But at that time, the UAV flew too high, and the cotton bolls cannot be seen clearly. Another difficulty for using the cotton bolls is that the image collected before harvest is hard to stitch together due to no plant leaves and fewer image features for stitching. the growing degree days (GDD) as one of the weather data is worth trying in the yield prediction model.

6.9 Literature cited

Addy, J.W., Ellis, R.H., Macdonald, A.J., Semenov, M.A., Mead, A., 2020. Investigating the effects of inter-annual weather variation (1968–2016) on the functional response of cereal grain yield to applied nitrogen, using data from the Rothamsted Long-Term Experiments. Agricultural and Forest Meteorology 284, 107898.

Allen, R., Pereira, L., Raes, D., Smith, M., 1998. Crop evapotranspiration-Guidelines for computing crop water requirements-FAO Irrigation and drainage paper 56. Fao, Rome 300, D05109.

Bian, J., Zhang, Z., Chen, J., Chen, H., Cui, C., Li, X., Chen, S., Fu, Q., 2019. Simplified Evaluation of Cotton Water Stress Using High Resolution Unmanned Aerial Vehicle Thermal Imagery. Remote Sensing 11, 267.

Ceglar, A., Toreti, A., Lecerf, R., Van der Velde, M., Dentener, F., 2016. Impact of meteorological drivers on regional inter-annual crop yield variability in France. Agricultural and forest meteorology 216, 58-67.

Chen, J., Jing, H., Chang, Y., Liu, Q., 2019. Gated recurrent unit based recurrent neural network for remaining useful life prediction of nonlinear deterioration process. Reliability Engineering & System Safety 185, 372-382.

Chen, R., Chu, T., Landivar, J.A., Yang, C., Maeda, M.M., 2018. Monitoring cotton (Gossypium hirsutum L.) germination using ultrahigh-resolution UAS images. Precision Agriculture 19, 161-177.

Chen, T., Guestrin, C., 2016. Xgboost: A scalable tree boosting system, Proceedings of the 22nd acm sigkdd international conference on knowledge discovery and data mining, pp. 785-794.

Chu, Z., Yu, J., 2020. An end-to-end model for rice yield prediction using deep learning fusion. Computers and Electronics in Agriculture 174, 105471.

Chung, J., Gulcehre, C., Cho, K., Bengio, Y., 2014. Empirical evaluation of gated recurrent neural networks on sequence modeling. arXiv preprint arXiv:1412.3555.

Djaman, K., Irmak, S., 2012. Soil water extraction patterns and crop, irrigation, and evapotranspiration water use efficiency of maize under full and limited irrigation and rainfed settings. Transactions of the ASABE 55, 1223-1238.

Du, M., Noguchi, N., 2017. Monitoring of wheat growth status and mapping of wheat yield's within-field spatial variations using color images acquired from UAV-camera system. Remote Sensing 9, 289.

Feng, A., Zhang, M., Sudduth, K.A., Vories, E.D., Zhou, J., 2019. Cotton yield estimation from UAV-based plant height. Transactions of the ASABE 62, 393-404.

Feng, A., Zhou, J., Vories, E., Sudduth, K.A., 2020a. Evaluation of cotton emergence using UAV-based narrow-band spectral imagery with customized image alignment and stitching algorithms. Remote Sensing 12, 1764.

Feng, A., Zhou, J., Vories, E.D., Sudduth, K.A., Zhang, M., 2020b. Yield estimation in cotton using UAV-based multi-sensor imagery. Biosystems Engineering 193, 101-114.

Forcella, F., Arnold, R.L.B., Sanchez, R., Ghersa, C.M., 2000. Modeling seedling emergence. Field Crops Research 67, 123-139.

Goodell, P.B., Davis, R.M., Godfrey, L.D., Hutmacher, R.B., Roberts, P.A., Wright, S.D., M, B.V., Haviland, D.R., Munier, D.J., Natwick, E.T., 2015. UC IPM pest management guidelines cotton, Oakland, CA.

Jiang, P., Thelen, K., 2004. Effect of soil and topographic properties on crop yield in a north-central corn–soybean cropping system. Agronomy Journal 96, 252-258.

Khaki, S., Wang, L., 2019. Crop Yield Prediction Using Deep Neural Networks. Frontiers in Plant Science 10.

Khaki, S., Wang, L., Archontoulis, S.V., 2020. A cnn-rnn framework for crop yield prediction. Frontiers in Plant Science 10, 1750.

Khiatani, D., Ghose, U., 2017. Weather forecasting using hidden Markov model, 2017 International Conference on Computing and Communication Technologies for Smart Nation (IC3TSN). IEEE, pp. 220-225.

Kitchen, N., Drummond, S., Lund, E., Sudduth, K., Buchleiter, G., 2003. Soil electrical conductivity and topography related to yield for three contrasting soil–crop systems. Agronomy Journal 95, 483-495.

Kitchen, N., Sudduth, K., Myers, D., Drummond, S., Hong, S., 2005. Delineating productivity zones on claypan soil fields using apparent soil electrical conductivity. Computers and Electronics in Agriculture 46, 285-308.

Lee, S.H., Goëau, H., Bonnet, P., Joly, A., 2020. Attention-Based Recurrent Neural Network for Plant Disease Classification. Frontiers in Plant Science 11.

Lipton, Z.C., Berkowitz, J., Elkan, C., 2015. A critical review of recurrent neural networks for sequence learning. arXiv preprint arXiv:1506.00019.

Liu, M., Wang, T., Skidmore, A.K., Liu, X., 2018. Heavy metal-induced stress in rice crops detected using multi-temporal Sentinel-2 satellite images. Science of the total environment 637, 18-29.

Maimaitijiang, M., Sagan, V., Sidike, P., Hartling, S., Esposito, F., Fritschi, F.B., 2020. Soybean yield prediction from UAV using multimodal data fusion and deep learning. Remote Sensing of Environment 237, 111599.

Mathieu, J.A., Aires, F., 2018. Assessment of the agro-climatic indices to improve crop yield forecasting. Agricultural And Forest Meteorology 253, 15-30.

Nogueira, F., 2014. Bayesian Optimization: Open source constrained global optimization tool for Python.

Oosterhuis, D.M., 1990. Growth and development of a cotton plant. Nitrogen Nutrition of Cotton: Practical Issues, 1-24.

Saxton, K., Rawls, W., 2006. Soil water characteristic estimates by texture and organic matter for hydrologic solutions. Soil Science Society of America Journal 70, 1569-1578.

Saxton, K., RRawls, W., Romberger, J., Papendick, R., 1986. Estimating generalized soil-water characteristics from texture 1. Soil Science Society of America Journal 50, 1031-1036.

Scherer, T.F., Franzen, D., Cihacek, L., 2017. Soil, water and plant characteristics important to irrigation. North Dakota State University, Fargo, North Dakota.

Schut, A.G., Traore, P.C.S., Blaes, X., Rolf, A., 2018. Assessing yield and fertilizer response in heterogeneous smallholder fields with UAVs and satellites. Field Crops Research 221, 98-107.

Schwalbert, R.A., Amado, T., Corassa, G., Pott, L.P., Prasad, P.V., Ciampitti, I.A., 2020. Satellite-based soybean yield forecast: Integrating machine learning and weather data for improving crop yield prediction in southern Brazil. Agricultural and Forest Meteorology 284, 107886.

Singhal, G., Bansod, B., Mathew, L., Taneja, S., 2018. A Preparatory Comparison of Landsat and Sentinel Satellite Data for Estimation of Chlorophyll Concentration in Vegetation, 2018 2nd International Conference on Micro-Electronics and Telecommunication Engineering (ICMETE). IEEE, pp. 230-233.

Tremblay, N., Bouroubi, Y.M., Bélec, C., Mullen, R.W., Kitchen, N.R., Thomason, W.E., Ebelhar, S., Mengel, D.B., Raun, W.R., Francis, D.D., 2012. Corn response to nitrogen is influenced by soil texture and weather. Agronomy Journal 104, 1658-1671.

Van Bussel, L.G., Ewert, F., Zhao, G., Hoffmann, H., Enders, A., Wallach, D., Asseng, S., Baigorria, G.A., Basso, B., Biernath, C., 2016. Spatial sampling of weather data for regional crop yield simulations. Agricultural and Forest Meteorology 220, 101-115.

Vories, E., O'Shaughnessy, S., Sudduth, K.A., Evett, S., Andrade, M., Drummond, S., 2020. Comparison of precision and conventional irrigation management of cotton and impact of soil texture. Precision Agriculture, 1-18.

Williams, R.J., Zipser, D., 1989. A learning algorithm for continually running fully recurrent neural networks. Neural computation 1, 270-280.

Yang, Q., Shi, L., Han, J., Zha, Y., Zhu, P., 2019. Deep convolutional neural networks for rice grain yield estimation at the ripening stage using UAV-based remotely sensed images. Field Crops Research 235, 142-153.

You, J., Li, X., Low, M., Lobell, D., Ermon, S., 2017. Deep Gaussian Process for Crop Yield Prediction Based on Remote Sensing Data, AAAI, pp. 4559-4566.

Zhang, M., Zhou, J., Sudduth, K.A., Kitchen, N.R., 2020. Estimation of maize yield and effects of variable-rate nitrogen application using UAV-based RGB imagery. Biosystems Engineering 189, 24-35.

Chapter 7. CONCLUSIONS AND FUTURE STUDY

7.1 Conclusions

This study tried to use emerging sensing technologies, such as soil EC sensors, and UAV imaging sensors as well as data from the weather station to understand the environmental effects on crop emergence, crop development and yield. This study specifically focused on methods to characterize crop development and yield using UAV-based remote sensing and deep learning technologies. This study also developed methods for the fusion of different spatiotemporal resolution soil, weather and images data so that those data can be used to quantification of soil and weather effects on crop development and yield. Specifically, this study developed the above characterize methods and the fusion methods that can be used in crop emergence, crop development and yield accordingly. The whole study showed that the developed technologies and methods are feasible for crop emergence evaluation, crop development monitoring and yield prediction.

First of all, this study developed methods and a framework for timely crop emergence mapping. High accuracy of crop emergence stand count and canopy size estimation was obtained in near real-time. With the improved crop row alignment algorithm, the mapping GPS accuracy was improved and provided the feasibility of exploring the relationship between emergence, subsequent growth and environment using UAV image data. Although there are only one-year data collected due to weather and equipment issues for the other year (the year 2018 and 2020), field elevation, $EC_{a\text{-}sh}$, $EC_{a\text{-}dp}$ and soil clay content in the shallow depth (i.e. clay10-clay30) still showed important effects on the crop stand count and seedling canopy size.

Secondly, crop development variation and water stress level can be quantified by the UAV multispectral images and thermal images. Under different years (i.e. 2018 and 2019) weather conditions and field management (i.e. irrigation management), crop vegetation indices increased and decreased differently in regions with different soil texture. The study showed that soil had more influence on crop development in the year that when water inputs were not enough and crop were under water stress. High sand content regions affected the crop development due to water stress, but the high sand content regions would not affect the crop development too much if irrigation were applied. If irrigation was applied and water inputs were enough, the effects of soil on crop decreased.

In the end, this study showed that the cotton yield could be estimated accurately and mapped based on the integration of soil, weather and UAV image data. Integration of soil, weather and images data is a promising way to understand the soil and weather effects on crop development and yield. With the methods and models developed in this study, predicting yield accurately in a future year before harvest based on the model training on previous years' soil, weather and UAV image data is feasible, which is meaningful for farmers to prepare harvest and make marketing decisions.

7.2 Future study

The methods and models developed in this study are promising for understanding soil and weather effects on crop emergence, crop development and yield. However, a larger amount of data may be required to give more convincing conclusions of the environmental effects on the crop. Currently, the temporal resolution for image data (once per month) and the spatial resolution for ground data (like soil moisture data) in this study was still not high. Future works may focus on higher temporal resolution image data (twice or three

times a week) to check more temporal details of the crop development and higher spatial resolution ground data (like soil moisture data) to understand more spatial distribution of the environmental characteristics of the field. Especially in the yield estimation study as described in Chapter 6, predicting the crop growth as well as yield together may also be meaningful for researchers and farmers. For the current model, the prediction of crop growth is still with low accuracy, and it requires more data support for future study.

More accurate prediction models are needed to have higher accuracy for yield estimation results and mapping. New models with machine learning and deep learning technologies are waiting to be explored. Especially, accurate models with higher explainable ability are needed to explain the relationships between crop, soil and weather as most of the machine learning and deep learning models are with low explanation ability currently. Explainable ability is important in agriculture science for understanding the environmental effects on the crop.

VITA

Aijing Feng was born in Yangjiang city of Guangdong Province, China. She received her bachelor's degree in software engineering from South China Agricultural University in 2014, and master's degree in computer application technology from South China Agricultural University in 2017. She started her Ph.D. studies in the Department of Biomedical, Biological & Chemical Engineering at University of Missouri-Columbia in the fall of 2017.

She is interested in developing and applying computer vision, machine learning, data mining techniques to address precision agriculture problems. Her research focuses on remote sensing, computer vision and machine learning. Specifically, her primary research is to use UAV-based imaging and machine learning methods in a cotton research field to automatically mapping cotton emergence, crop development variation under different soil texture and weather condition, as well as yield prediction.